ADHESION SELECTIVITY VIA COMPLEMENTARITY

A Dissertation

Presented to the Faculty of the Graduate School

of Cornell University

in Partial Fulfillment of the Requirements for the Degree of

Doctor of Philosophy

by

Congrui Jin

January 2013

ADHESION SELECTIVITY VIA COMPLEMENTARITY

Congrui Jin, Ph.D.

Cornell University 2013

Selective adhesion between surfaces is a highly desirable property for many practical applications. The ability to control adhesion selectivity by design of near-surface architecture irrespective of surface chemistry is broadly appealing. The first chapter shows that highly selective interfacial properties can be achieved between surfaces patterned with complementary micro-channel structures: strongly enhanced work of adhesion between two matched patterns and highly attenuated adhesion between most others. Relative misalignment is accommodated by screw dislocations that run in a direction orthogonal to the channels. Dislocation energy governs the width of dislocation core; misorientation controls dislocation distribution through the Moire pattern of pillar/channel combinations on the two sides of the interface. This versatile system could be a useful experimental tool in assisting research on geometry-controlled adhesion, while providing a test-bed for stability theories of interacting dislocations and crack fronts. The second chapter studies the adhesion selectivity by electrostatic complementarity. We consider the interaction between two flat surfaces separated by water in the presence of ions, each with simple striped pattern of alternating positive and negative surface charges, and each with zero net charge. We show that such surfaces have highly selective adhesion depending on the matching between the two charge patterns. Because a number of problems related to micro-structured surfaces require analysis of their contact mechanics and extraction of material properties of indentation ex-

periments, the third chapter provides a complete numerical simulation package that allows for general analysis of the contact problems involving complex geometry. To solve the system of a large number of highly nonlinear equations, a virtual state relaxation method has been used by interposing a virtual dash-pot in the mechanical system. This method plots only the stable equilibriums for each displacement, and therefore the load-displacement curves are discontinuous at unstable jumps. It essentially generates the force-displacement curves that can be observed in real-world experiments.

BIOGRAPHICAL SKETCH

Congrui Jin received her M.S. degree in Department of Mechanical Engineering from University of Alberta, Edmonton, Canada in 2009 and Ph.D. degree in Field of Theoretical and Applied Mechanics in Sibley School of Mechanical and Aerospace Engineering from Cornell University, New York, USA in 2012. She was the recipient of Cornell Fellowship for the 2009-2010 academic year. She then became a postdoctoral associate in the Materials Science and Technology Division at Oak Ridge National Laboratory, Tennessee, USA. Her research interests include continuum mechanics, contact mechanics, biophysics and material simulation.

ACKNOWLEDGEMENTS

I wish to express my most sincere gratitude and appreciation to my advisor, Prof. Chung-Yuen Hui, who has given me an abundance of intellectual freedom, patience, support, and understanding throughout the development of the project. It is Prof. Hui who had guided me into the exciting field of mechanics, and introduced me to a splendor of fascinating topics. I believe what I have learnt from him will have a direct impact on my future professional career.

I would like to thank Profs. Anand Jagota, Stuart Phoenix and Timothy Healey for their encouragement and suggestions during the last three years.

This dissertation is a collection of the journal papers that I had published during my Ph.D. at Cornell University. Trying to satisfy the high standards of the referees for these journals encouraged me to develop much clearer explanations for many mechanics topics. I would like to thank these referees who do their work in anonymity.

TABLE OF CONTENTS

LIST OF TABLES

LIST OF FIGURES

CHAPTER 1

STRUCTURE AND ENERGETICS OF DISLOCATIONS AT MICRO-STRUCTURED COMPLEMENTARY INTERFACE GOVERN ADHESION

1.1 Introduction

Adhesion selectivity* via complementarity involves endowing surfaces with specific properties, such as textures, so that interaction between all except matching pairs is strongly attenuated. Complementarity was interpreted in a geometric sense by ancient Chinese who first drew the Tai Chi symbol, which describes the interconnection and interdependence of two complementary opposites within a united system, i.e., "yin" and "yang". Various types of complementarity have been widely observed in nature, e.g., shape, charge, magnetic, and hydrogen-bonding [1–12]. The recent study by Singh et al. [13] provides a comprehensive list of references, both theoretical and experimental.

Although the physical principles of complementarity in nature are quite well understood, the deliberate control of adhesion selectivity of material surfaces by complementarity has not been studied much as yet [14]. The possibility of adhesion selectivity between two flat surfaces with striped patterns of alternating positive and negative surface charges separated by an electrolyte has been analyzed by Bai et al. [15] and Jin et al. [16]. As for structural and shape complementarity, Vajpayee et al. [17] showed that highly selective adhesion can be achieved between complementary elastic surfaces patterned with ripples. Their

[0]*The final version of this paper has been submitted as: Congrui Jin, Anand Jagota and Chung-Yuen Hui 2012 Structure and energetics of dislocations at a micro-structured complementary interface govern adhesion. Advanced Functional Material.

results demonstrated that it is relatively simple to destroy adhesion between non-complementary surfaces. For example, rippled surfaces with different amplitudes or wavelengths do not adhere to each other. The basic question in achieving selective adhesion is whether and how the inevitably present small mismatches, either in the dimensions of the pattern or in alignment of the two sides of the interface, will be accommodated over length scales much larger than that of the repeating pattern. Singh et al. [13] investigated the adhesion enhancement between complementary surfaces with micro-channel structures in a rectangular-toothed pattern, and observed an interesting phenomenon: the appearance of defects in the form of visible striations. Their results suggested that these defects accommodate relative misorientation and also strongly influence the resulting properties.

In the present study, we examine the observed defect structures in details. In particular, we establish their geometrical features to relate the local/global changes in the distribution and orientation of defect structures to the influencing factors, such as misorientation and pillar/channel's geometrical parameters. We ask the questions: How do defect structures affect the interfacial adhesion? What is the enhancement due to complementarity and how is it attenuated by the defects? What is the nature of interfacial crack growth? How does the crack interact with the microstructures and with defects? To answer these questions quantitatively, we have carried out a series of well-controlled adhesion tests on complementary surfaces while progressively increasing the misalignment angle, which was found to be the key factor controlling the adhesion strength. It is hoped that such an approach will contribute to a better understanding of the effect of directional patterned heterogeneities on interfacial fracture energy between complementary surfaces, with potential implications for their use as

adhesives, binders, coatings and sealants.

1.2 Experimental Methods

1.2.1 Sample Fabrication

To fabricate samples with micro-channel structures in a rectangular-toothed pattern on the surface, i.e., parallel channels with a rectangular cross-section, we began by molding an elastomer, poly-(dimethylsiloxane) (PDMS), into etched silicon masters with parallel micro-channels on the surface patterned by photolithography, as shown in Fig. 1a. The channel width of the original masters, w, was fixed at 10 μm, the minimum center-to-center spacing or smallest period, c, was varied from 20 to 125 μm, and channel depth, d, was varied from 10 to 20 m. This study is mainly focused on the case $d = 10\,\mu$m. Liquid PDMS precursor (silicone elastomer base) was mixed with curing agent (Sylgard 184 Silicone Elastomer kit, Dow Corning) in weight ratio of $10 : 1$. The liquid silicone mixture was then degassed under vacuum for 40 minutes before applying to the master and was cured at a temperature of 80 ^{o}C for 120 minutes.

The cured PDMS layer, as shown in Fig. 1b, was then peeled off the silicon master. A typical piece of sample is 610 μm thick, 30 mm long and 10 mm wide. This first set of PDMS sample is called the pillar side. The pillar side was coated by a monolayer of n-Hexadecyltrichlorosilane (C16H33Cl3Si). A sample with a complementary surface profile, called the channel side, was obtained by a second molding and curing of PDMS on first set of the samples (i.e. the pillar side), as shown in Fig. 1c, which also shows the optical micrographs of a pair of

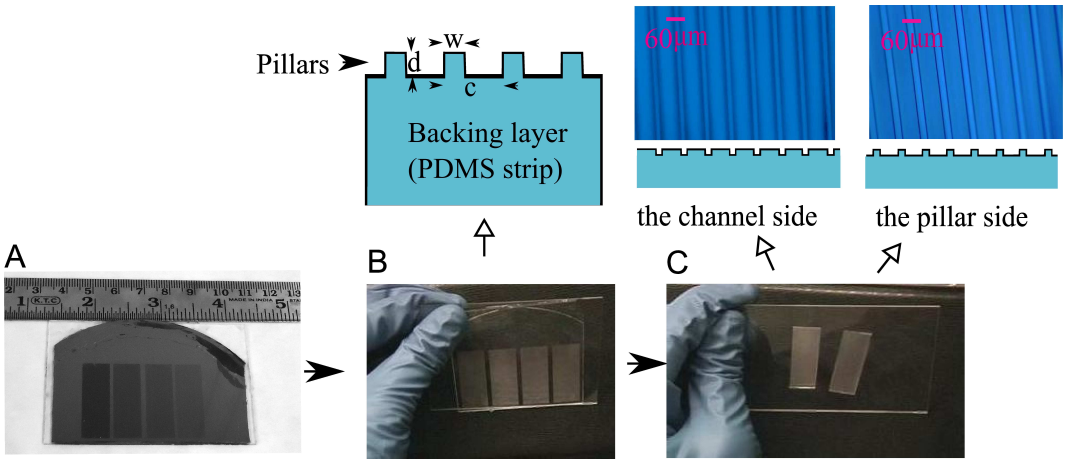

Figure 1.1: Illustration of sample fabrication. A typical piece of sample is 610 μm thick, 30 mm long and 10 mm wide. (a) The etched silicon masters with parallel micro-channels on the surface patterned by photolithography. This silicon master contains four patterned areas. (b) The cured PDMS layer was peeled off from the silicon master. This set of samples is called the pillar side. (c) The channel side was obtained by a second molding and curing of PDMS on the first set of the samples. This figure also shows the optical micrographs of a pair of complementary surfaces.

complementary surfaces.

1.2.2 Adhesion Testing

The PDMS strips with the internal rectangular-channel interface were peeled manually, hence creating two strips each with structured patterns on their surface. The rotational misalignment angle θ, as defined in Fig. 2a, is the key factor controlling the positioning accuracy and adhesion strength of the two complementary surfaces. We measured the adhesion of the complementary surfaces for different values of misalignment angle in the following manner, as shown in Fig. 2b.

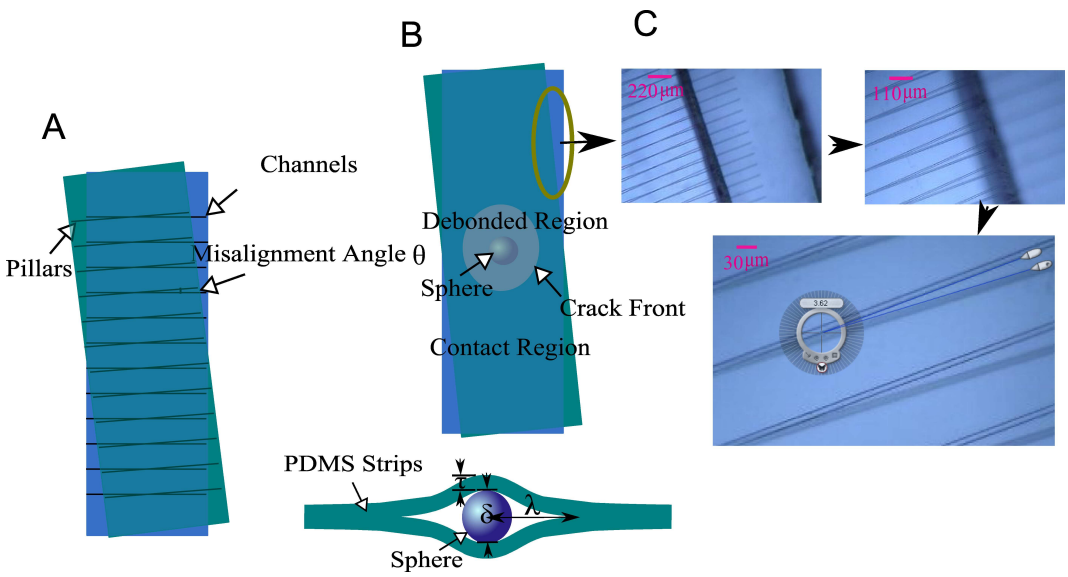

Figure 1.2: (a) The rotational misalignment angle θ is the key factor in determining the positioning accuracy of the two complementary surfaces, and hence their adhesion strength. The interchannel spacing has been exaggerated in the diagram for visual clarity. (b) Top view and cross-section schematic (not drawn to scale) of adhesion test by inserting a small glass sphere at the interface. (c) Precise measurement of misalignment angle by analyzing the optical micrographs taken at the edges of the decohered PDMS strips. The value of misalignment angle was determined by making ten repeated measurements using the Screen Protractor (commercial software developed by Iconico, Inc.) with resolution 0.01^o. The sample shown above has the same channel depth and width $d = w = 10\,\mu$m, and $c = 110\,\mu$m. Ten repeated measurements of the misalignment angle θ had a mean of 3.69^o and a standard deviation of 0.52^o in this case.

A small glass sphere of known diameter, δ, typically either 0.3 or 0.4 mm, is placed at the micro-channel/pillar interface of two samples. We then press the two sheets against each other sufficiently, attempting to force pillars on one sheet to find and insert into the channels of the other. To simplify the analysis, both ends of the resulting sandwich structure are fixed on glass slides so that the expected debonding zone is freestanding, thereby ensuring that the two sheets are deflected equally in opposite directions, as shown in Fig. 2b.

Immediately upon release of the pressing force, a crack propagates away from the sphere, since the sphere applies an opening displacement approximately equal to its diameter, and as a result, a debonded region forms between the two PDMS strips. Eventually the crack arrests at an equilibrium length, which results from a balance between energy release rate supplied by the debonded portion of the PDMS strip and the energy required to increase the crack area by a unit amount. The crack propagation was recorded by a Panasonic PV-GS400 3CCD Camcorder during the tests. Each video was stored together with a time stamp which allows each frame to be associated with a specific time. Using the dimensions of a folding ruler in the video images as spatial calibration, direct dimensional measurements could be made.

Because the pillar structures have dimensions of order 10 μm, and the misalignment angles in the experiments are usually very small, adequate care must be taken to accurately measure the misalignment angle. In the experiments, directly after the properties (defined in the next section) of a pair of misaligned complementary surfaces had been measured, a thin wire was carefully inserted between the surfaces without changing the relative position between the two sheets, making the two PDMS strips decohere laterally from the corners. By analyzing the optical micrographs taken at the edges of the decohered strips, the misalignment angle was determined by making ten repeated measurements using the Screen Protractor as shown in Fig. 2c.

1.3 Results and Discussion

1.3.1 Dislocation Structures

For any pair of complementary surfaces, when we try to insert pillars into their complementary channels, even with great care taken to align the two PDMS strips, we invariably observe defects in the form of visible striations tens to hundreds of microns in width where pillar/channel combinations are not fully inserted. The striations are visible because of light scattering from interfacial regions in partial contact. Away from the striation are featureless regions where the pillars are perfectly inserted into the channels, as shown in Fig. 3. For additional examples, see Fig. A1 in Appendix A. In the visible striations, pillars are first partially debonded from their corresponding channels, and then extracted from their channels and shifted over by one period in the core region, and then partially inserted into a neighboring channel. The striations can thus be viewed as "screw dislocations" that carry a Burgers vector with magnitude of interchannel spacing c. (The dislocation is a pure screw dislocation only when the dislocation region is perpendicular to the orientation of the pillar/channel combination; otherwise, it is a mixture of screw and edge dislocations.) The dislocation region where the pillars are completely pulled out and sheared sideways by a distance of c is clearly dilated. Fig. 3 also shows that these dislocation regions become wider as the inter-channel spacing, c, increases, and as a result, some intricate dislocation patterns, such as closed loops, as shown Fig. A2, are only observed in the samples with small interchannel spacings ($c < 60\ \mu$m) because of the limited sample size (30 mm $\times$ 10 mm).

Some of the salient properties of dislocation structures will be explored in

next section: the local geometric properties, such as the widths of the dislocation region and the core region (i.e. a and b, respectively, as defined in Fig. 3), and the dilation of the core region; and a series of general properties, such as the distance between dislocation regions, the orientation of the dislocation regions (i.e., the acute angle α between the tangent vector to the curve of the dislocation region and the orientation of the pillar/channel combination, as defined in Fig. 3), and the area fraction of the featureless region.

1.3.2 Rotational Misalignment

Rotational misalignment is one of the principal reasons that the dislocation defects occur. The rotational misalignment angle between the two PDMS strips is defined in Fig. 2. The adhesion reduction due to a small angular misalignment is surprisingly large. Here we define θ_m as the maximum angle allowed between two PDMS strips when featureless regions (where the pillars are fully inserted into the channels) can still be observed, and thus when $\theta > \theta_m$ there exists no (or negligible) adhesion between the two sheets. We found that $\theta < 10^o$ for all the samples tested, and θ_m decreases with increasing interchannel spacing c, as shown in Fig. 4.

- Case 1: Nearly perfect alignment when $\theta < 2^o$

When we insert pillars into their complementary channels with care taken to align the two PDMS strips, we still observe dislocation regions in all the samples. When θ is very small, only a few dislocation regions are found. Since they show no regular pattern, no generalizations can be made about the possible causes for the defect. It could be a mixture of local mismatch, relative

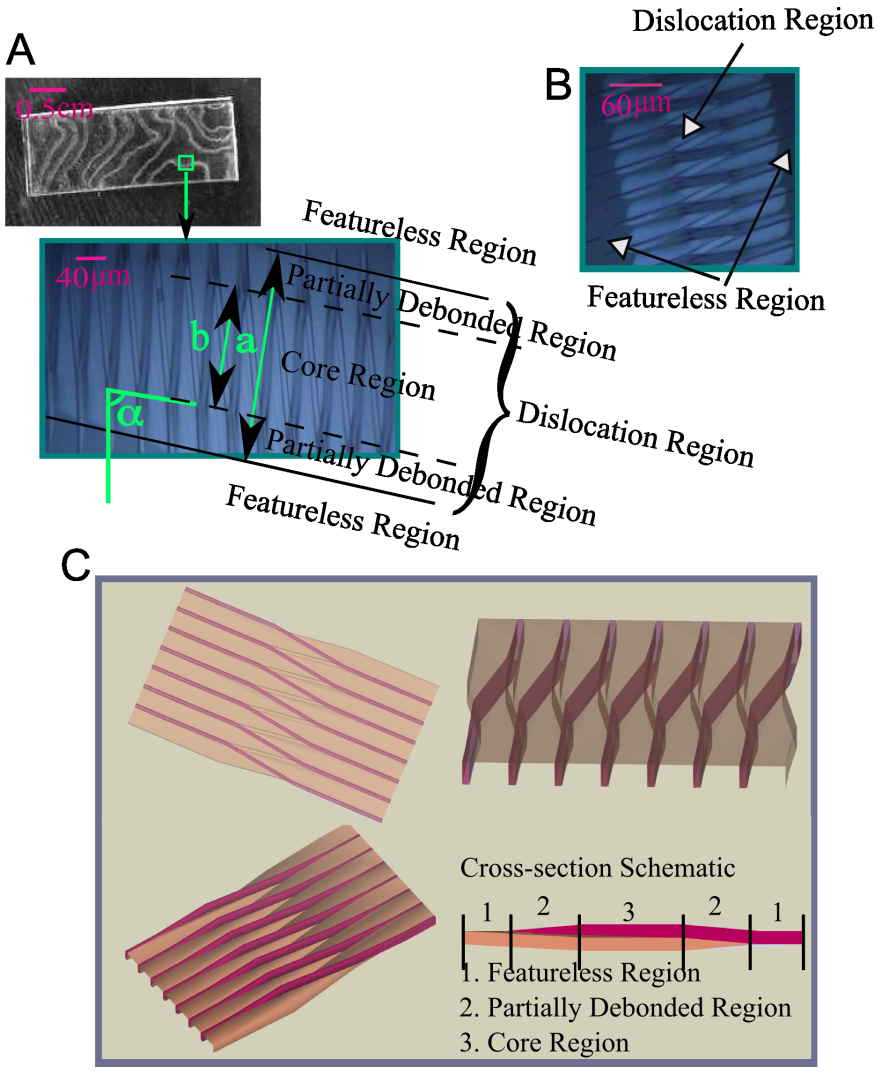

Figure 1.3: (a) and (b): Photograph and optical micrographs of dislocation regions in complementary surfaces. The samples have the same channel depth and width, $d = w = 10\,\mu$m, and a misalignment angle $\theta < 2^o$. The interchannel spacing c: (a): 40 μm (b): 30 μm. Clear, featureless regions are those where pillars have been inserted fully into channels. The striations are dislocation regions where pillars fail to fully insert into channels. The orientation of the dislocation regions is described by the acute angle α. (c): Schematic illustration of dislocation structures. A series of views from different angles show that the dislocation region where the pillars are completely pulled out and sheared sideways by a distance of c is clearly dilated.

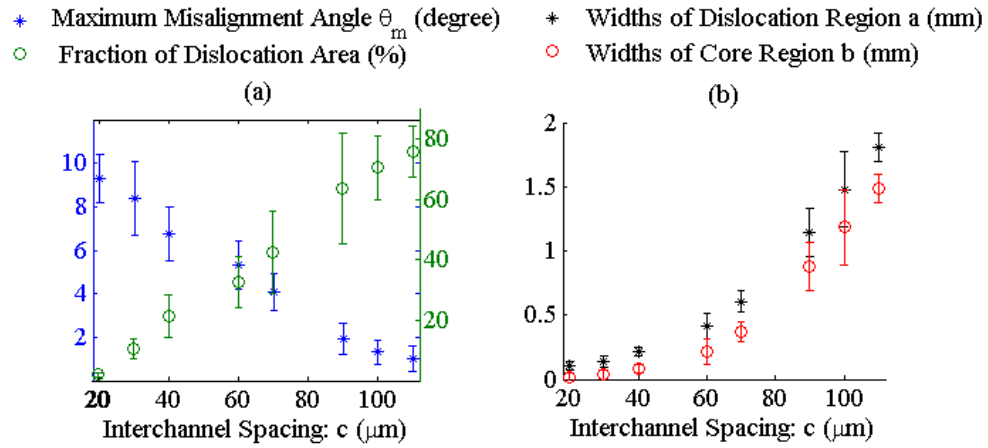

Figure 1.4: (a) Maximum misalignment angle θ_m and the fraction of dislocation area in one sample as a function of interchannel spacing c when $\theta < 2^o$, taking the average of a number of measurements. (b) Widths of the dislocation region a and core region b as a function of interchannel spacing c when $\theta < 2^o$. Error bars represent standard deviation. All the samples have the same channel depth and width, $d = w = 10\,\mu$m.

shear, misorientation, non-uniformity in pressing force and/or material properties, wherein there is no single dominant factor. Nonetheless, some general trends have been observed. The width of the dislocation region a, the width of the core region b, and the fraction of dislocation area in one sample, as a function of interchannel spacing c (when $\theta < 2^o$), are presented in Fig. 4. It shows that the fraction area covered by defects in one sample is approximately proportional to the interchannel spacing, consistent with the previous study reported by Singh et al. [13]. It also shows that the widths of the dislocation region and the core region both increase with increasing interchannel spacing.

The surface profile of the resulting sandwich structure, measured using an interferometric optical profilometer (ZeGage. Zemetrics, Inc), confirmed the dilation of the core regions. A typical surface morphology is shown in Fig. A3.

The region on the surface right above a dislocation region at the interface is usually 0.4 μm to 0.8 μm higher than that above a featureless region. As discussed later, the local geometric properties of the dislocation region, such as the widths of the dislocation region and the core region, i.e., the results presented in Fig. 4b, and the dilation of the core region, i.e., the results presented in Fig. A3, do not depend on the misalignment angle. On the other hand, the fraction area covered by defects, i.e., the results presented in Fig. 4a, will change as the misalignment angle is increased.

- Case 2: Moderate misalignment when $2^o < \theta < \theta_m$

As we gradually increase the misalignment angle to about 2.5^o, the rotational misorientation plays a dominant role in the formation of dislocation structures, and as a result, the initially almost random distribution of dislocation regions resolves into a periodic pattern, which is the most striking and reproducible observation of the experiments, as shown in Fig. 5. The dislocation regions are fairly uniformly distributed over the entire interface, including the edges and corners, as shown in Fig. A4. The experimental values for angle α, the acute angle between dislocation region and the pillar/channel combination, as defined in Fig. 3, usually fall within the range of $80^o < \alpha < 90^o$, i.e., in most cases, the dislocation regions are perpendicular (or nearly so) to the orientation of the pillar/channel combination. The experimental results also show that the local geometric properties of the dislocation region, such as the widths of the dislocation region and the core region, and the dilation of the core region, depend only on the characteristic lengths of the rectangular-toothed channel pattern, i.e., the values of w, d and c, and not on the misalignment angle, which means that the angular misalignment affects only the dislocation density, not its internal struc-

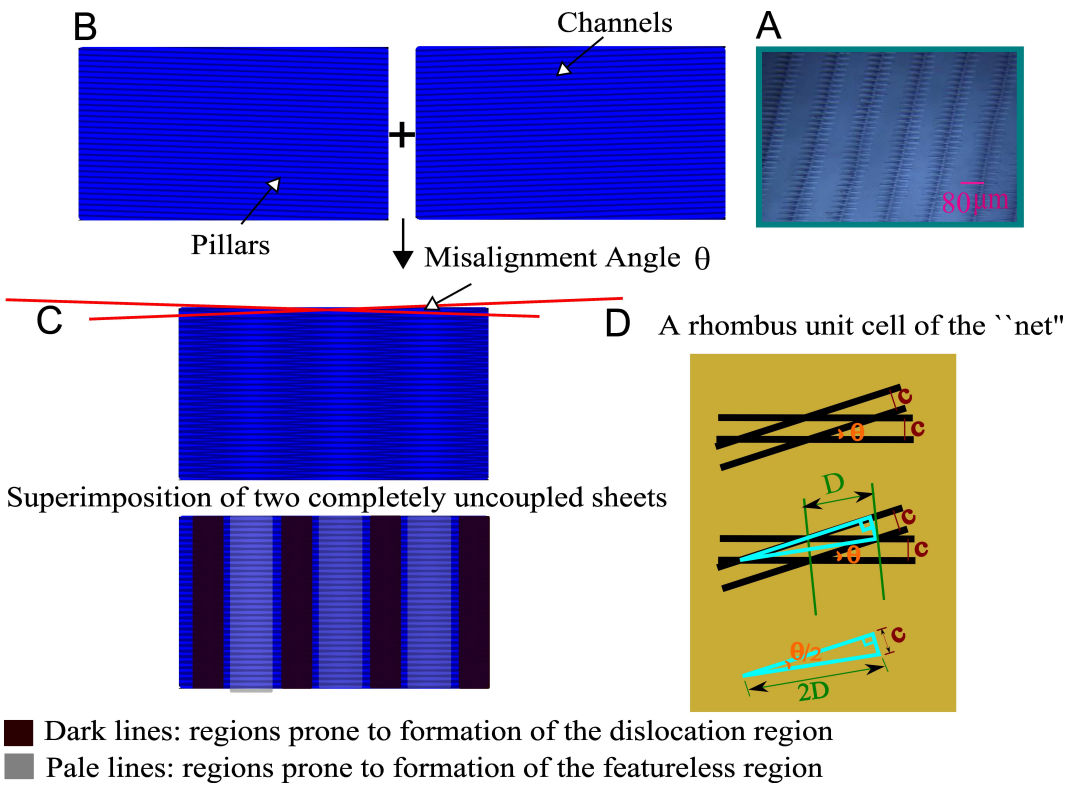

Figure 1.5: (a): Optical micrograph of the periodic pattern of dislocation regions in misaligned complementary surfaces. The sample has the same channel depth and width, $d = w = 10\ \mu$m, and the interchannel spacing $c = 30\ \mu$m. The misalignment angle $\theta = 3.59^o$. (b)-(d): Schematic diagrams illustrating the formation of the observed periodic dislocation pattern in two rotationally misoriented complementary surfaces. A Moire pattern is created by superimposing two sets of parallel and equidistant lines, one set rotated by a small angle ($\theta = 3.59^o$ in this case) with respect to the other.

ture.

In some cases, spatial variation in dislocation density caused by non-uniformity in rotation, pressing force, material properties, and/or in-plane stretch, is observed, but the overall trend is clear and consistent that when the value of misalignment angle is increased, the density of the dislocation regions increases, and hence the area of the featureless region between the lines de-

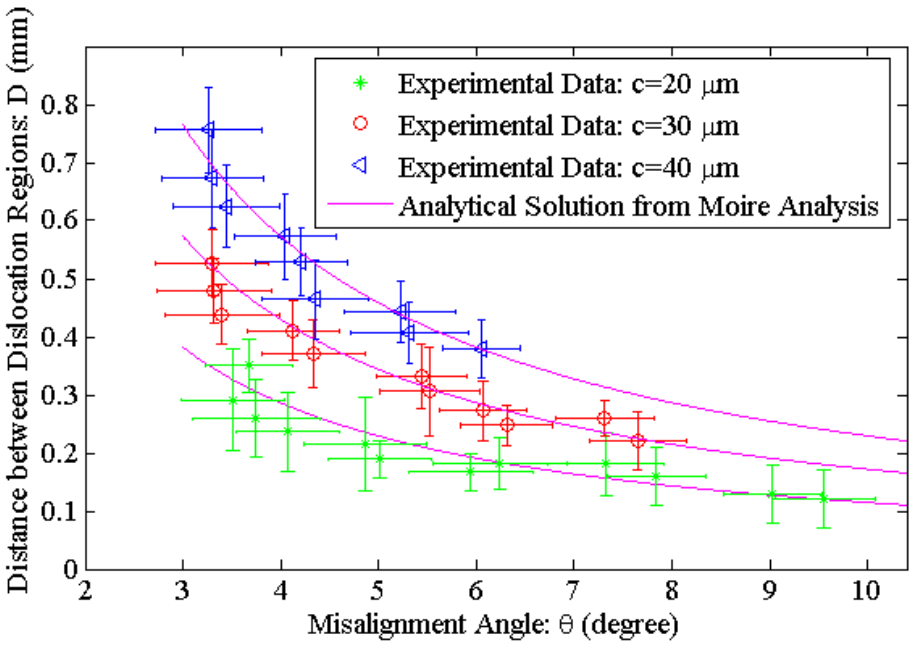

Figure 1.6: Distance between dislocation regions D, i.e. the pattern period, as a function of the misalignment angle θ, taking the average of a number of measurements. Error bars represent standard deviation. All the samples have the same channel depth and width, $d = w = 10$ μm, and the interchannel spacing c is varied from 20 m to 40 μm. Some data were obtained from experiments performed on smaller samples (such as 8 mm $\times$ 10 mm in size) to reduce the effects of non-uniformity in rotation, pressing force, material properties, and/or in-plane stretch.

creases. This trend is quantified in Fig. 6, which plots the distance between dislocation regions, D, i.e. the pattern period, as a function of the misalignment angle θ.

Surprising as it may seem, however, the observed periodic dislocation pattern is actually a direct consequence of the superimposition of two moderately misoriented complementary surfaces with periodic rectangular-toothed channels on the interface. The theoretical mechanism is explicated by Fig. 5, a schematic representation (drawn to scale) illustrating the formation of periodic dislocation pattern for two rotationally misoriented samples with $d = w = 10$

μm, $c = 30$ μm, and $\theta = 3.59^o$ (i.e. the example shown in Fig. 5a). Fig. 5 plots two identical sets of parallel and equidistant lines as a two dimensional simplification of a pair of complementary surfaces, one representing the channel side and the other representing the pillar side. When these two are superimposed with a small angular misorientation, a Moire pattern [18–20] is then shown in Fig. 5c. "Moire" is the French word for "watered" and is familiar to most people in the term "moire silk" or perhaps through familiarity with the more common moire-look vinyl window shades. As seen from a far distance, the Moire pattern gives pale and dark periodic lines, where the pale lines correspond to the lines passing through the intersections of the two sets of lines. We can imagine that when the two samples are pressed against each other, the pale lines wherein pillars and channels are in close proximity to each other are prone to formation of the featureless regions, whereas the dark lines are prone to formation of the dislocation region. A rhombus unit cell of the "net" is shown in Fig. 5d, in which the misalignment angle is exaggerated for ease of illustration. Since the spacing between two pale lines is D, the longer diagonal of the rhombus is $2D$, which is the hypotenuse of the cyan right triangle. We thus obtain the following equation:

$$2D = c/\sin(\theta/2) \tag{1.1}$$

The relationship based on Eqn. (1) is plotted in Fig. 6, which shows that the analytical result from Moire analysis matches closely with the experimental data for all the three types of samples. This also demonstrates that local/global misalignment angle can be estimated through examination of the local/global Moire pattern.

- Case 3: Severe misalignment when $\theta > \theta_m$

Under severe misalignment condition $\theta > \theta_m$, there exists no (or negligible) adhesion between the two sheets. The dislocation regions are so close-packed that no featureless region exists in between, and hence it is observed that the entire sample scatters light. When θ is slightly larger than θ_m, however, the featureless region can be observed at first, but the defect structure is not stable, and as a result, the featureless regions in between start to shrink upon release of the pressing force, and gradually become spotty before they disappear altogether. Simultaneously, the core region starts to relax, i.e. the width of the core region starts to increase, which ultimately leads to a complete detachment of the two sheets. Images from a video in Fig. A5 represent details of two typical sequences leading to the detachment of two PDMS strips.

1.3.3 Crack Propagation and Adhesion Strength between Complementary Surfaces

When the pressing force is released, the driving energy release rate due to the inserted sphere exceeds the ability of the interface to arrest it, and the crack begins to propagate, forming a debonded region, as shown in Fig. 2. We also carried out control experiments on nominally flat samples of the same thickness, because the solution for a flat interface is known and consequently provides a baseline to compare against. Since the two complementary strips are opened up by a displacement equal to the diameter of the sphere, δ, whose ratio to the thickness of the strip, τ, is always about 0.6 or less, the opening strips can be modeled as a linearly elastic plate with Youngs modulus E and Poisson's ratio ν. For flat samples, the equilibrium shapes of the debonded region are always

circular, and the relationship between the applied energy release rate, G, and the radius of the debonded region, λ, can be expressed as [21,22]:

$$G\lambda^4 = \frac{E\tau^3}{6(1-\nu^2)\delta^2} \tag{1.2}$$

For structured samples, we waited for two hours for the crack to achieve its equilibrium position; for flat samples, a much longer time (up to four hours) was needed. It is interesting to note that some samples appear to exhibit an equilibrium crack length after a relatively short time, although at much longer times, the crack length continues to increase.

Fig. 7 shows photograph and microscopic images of the region near an advancing crack front. It can be seen that the crack propagation on structured interfaces behaves quite differently from flat interfaces. For structured interfaces, there are two distinct fronts, one where the pillars have partially debonded from their complementary channels, and a second one behind which the pillars are fully extracted from their channels, consistent with observations from the previous study [13]. For structured samples, the shape of the debonded region is always close to circular, but never perfectly so, with or without the influence of dislocations, so we refer to its mean radius as crack length, still denoted by λ, so that $\pi\lambda^2$ is equal to area of the debonded region. The deviation from circularity, typically in the range of $3\% - 15\%$, varies from sample to sample, and is not reproducible, even on the same sample.

- Case 1: Nearly perfect alignment when $\theta < 2^o$

The shape variability is mainly attributed to the stepwise nature of the crack propagation. The growth of the partially-debonded crack front is not continuous; rather, it is observed to proceed by the formation of new microcracks ahead

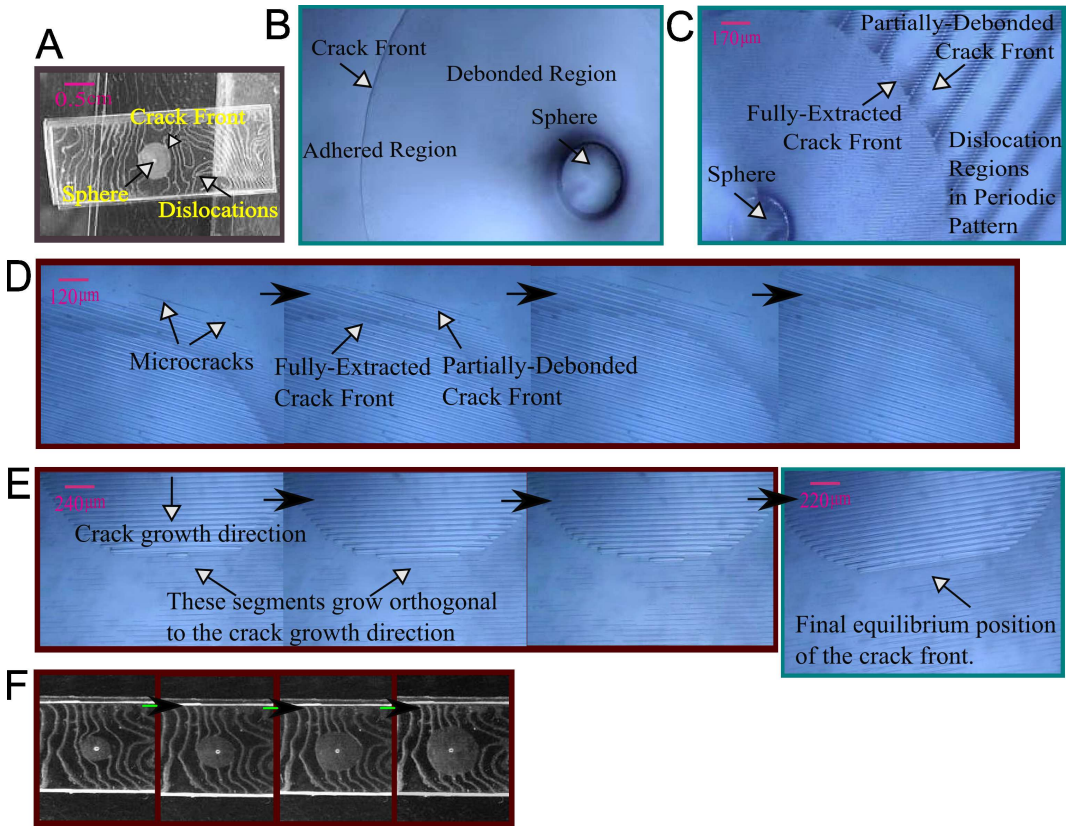

Figure 1.7: (a) Photograph of a structured sample showing that the crack propagates away from the sphere and a debonded region forms. Also visible are a series of dislocations. (b) Optical micrographs of the region behind and ahead of the crack front at the interface between two flat surfaces. (c) A structured sample showing a crack advancing through a well-adhered region of the interface. As the misalignment angle increases, the random distribution of dislocation regions resolves into a periodic pattern. (d) and (e) Images from a video representing details of typical sequences of the moving crack front, where nucleation, growth and coalescence of microcracks take place. (d) These images are taken at time intervals of 12 seconds, while the first frame was acquired 20 seconds after release of the pressing force. (e) These images are taken at time intervals of 8 seconds. Crack growth halted at a final crack length in the last frame. (f) The influence of pre-existing dislocations on the shape of the debonded region can be substantial. The last frame shows the final equilibrium shape of the debonded region. All the samples shown above have $d = w = 10\ \mu$m. The interchannel spacing: $c = 20\ \mu$m in (a), (c), (d), $c = 30\ \mu$m in (f), and $c = 40\ \mu$m in (e). The misalignment angle: $\theta < 2^o$ in (a), (d), (e) and (f), and $\theta = 4.65^o$ in (c).

of the moving partially-debonded crack front, which is followed by microcrack coalescence (by extending existing microcracks and connecting them into the main crack) and further microcrack formation along the growth direction of the main crack. These microcracks are always initiated at the tip of the teeth in the rectangular-toothed channel pattern and then extend along the parallel channels, as shown in Figs. 7d and 7e. Presumably, local stress concentrations determine which tooth segments crack first. This irregular staircase pattern of crack growth is also evident with the fully-extracted crack front, which immediately follows the partially-debonded front. This discontinuous nature of the interfacial crack growth process is not surprising. The crack front is trapped as it tries to kink in a direction that is perpendicular to its original path. It is well known that the energy release rate, G, at the tip of a kinked crack can be significantly less than its value prior to kinking. For example, the energy release rate at the tip of kinked crack, where the kink angle is 90^o from the initial crack plane, is only 25% of the energy release rate that would exist if the crack had advanced straight ahead [13, 23]. Therefore, even in dislocation-free zones, the directionally patterned heterogeneous interface does not simply unzip in a continuous manner.

In most cases, multiple dislocation regions that are simultaneously formed upon release of the pressing force reside within the expected debonding region. Experimental results show that these dislocations can be a source of strong local perturbations along the crack path. The direct interaction of a propagating crack with stationary or quasistationary dislocations can generate substantial crack front deflections, and as a result, the shape of the debonded region is strongly influenced by the distribution and orientation of the pre-existing dislocations, as shown in Fig. 7f and Fig. A6.

We measured the equilibrium crack length, λ, and then converted it into effective interfacial adhesion energy, W, using Eqn. (2). Fig. 8 plots the effective interfacial adhesion energy normalized by its value for a flat control. For each set of samples, we made 10 repeated tests. The first striking observation is that one can achieve a significant enhancement of adhesion, up to a factor of 30, over the flat control. Second, it is noticeable that, due to the influence of randomly distributed dislocations, despite the general trend that the equilibrium crack length increases with increasing interchannel spacing, the values of equilibrium crack length can differ significantly from sample to sample, and is not reproducible, even on the same sample. In a previous work [13], we have analyzed that adhesion enhancement is mainly attributed to two mechanisms: crack trapping and frictional pull-out.

To understand the influence of dislocations on crack propagation, two typical crack-dislocation interaction sequences are illustrated in Fig. 9 and Fig. A7. These images are taken at time intervals of 60 seconds, and the final equilibrium state of the crack front is shown on the right. It can be seen that the distance between the crack front and the dislocation continued to decrease until they coalesced. In the end, the crack did not cross the dislocation region, but rather travelled mainly along the orientation of the dislocation region. Note that such a behavior is already seen in Fig. A5, showing that the core region does not relax, i.e., the width of the core region does not increase, until the last step of detachment process, i.e., after the disappearance of the featureless region on both sides of the dislocation region. Such crack-dislocation interactions imply that the presence of dislocations alters the stress field near the crack front, and deflects the crack path from the preferred growth direction straight ahead.

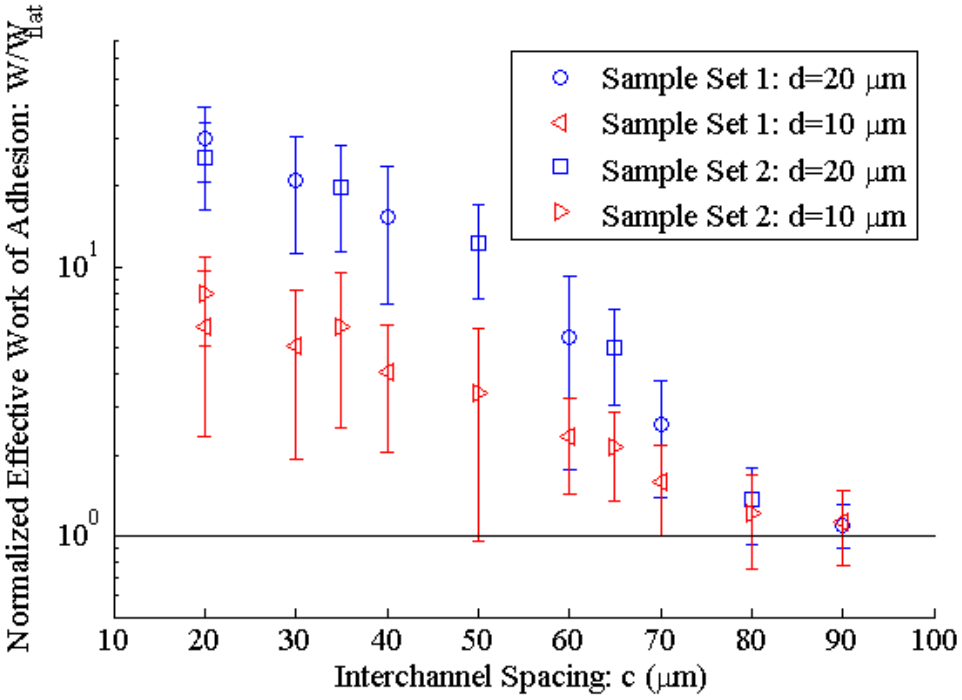

Figure 1.8: Normalized effective work of adhesion for different values of interchannel spacing, and two different channel depths (d = 10 μm and 20 μm). Error bars represent standard deviation. is represented by a horizontal line. The interchannel spacing c is varied from 20 μm, 30 μm, 40 μm, 60 μm, 70 μm to 90 μm in Sample Set 1; and from 20 μm, 35 μm, 50 μm, 65 μm to 80 μm in Sample Set 2. All the samples shown above have w = 10 μm and $\theta < 2^o$.

- Case 2: Moderate misalignment when $2^o < \theta < \theta_m$

As we gradually increase the misalignment angle, the random distribution of dislocation regions resolves into a periodic pattern, as shown in Fig. 7c. As we analyzed previously, increasing the misalignment angle increases the dislocation density, which results in a lower adhesion strength, as shown in Fig. 10, implying that the presence of the dislocation regions, while accommodating rotational mismatch between two complementary surfaces, is detrimental to adhesion.

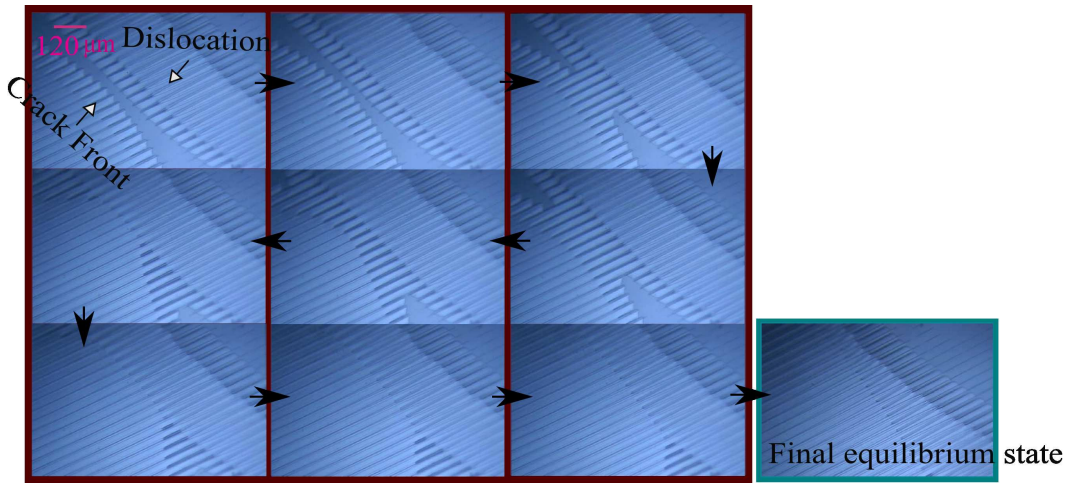

Figure 1.9: Images from a video representing a typical crack-dislocation interaction sequence. The sample has $d = w = 10$ μm, $c = 40$ μm, and $\theta < 2^o$. The featureless region between the dislocation and the crack front is where the pillars are fully inserted into the channels.

1.3.4 Relationship between Local Geometric Properties of Dislocation Structure and Interfacial Adhesion Strength

In the previous two sections, we discussed the local geometric features of the dislocation structure, e.g. the results shown in Fig. 4b, and interfacial adhesion strength between complementary surfaces, e.g. the results shown in Fig. 8, respectively, and in this section, we will examine whether there is actually a relationship between the two. To explain quantitatively the dependence of the local geometric features of dislocation structure on adhesion strength, we need to understand that, because of the disruption of the perfect periodicity around a screw dislocation, there is a strain energy per unit length, E_s, in a region bounded by cylinders of radii $b/2$ and R_o ($R_o > b/2$), as shown in Figs. 11a and 11b, which depends quadratically on the magnitude of the Burgers vector

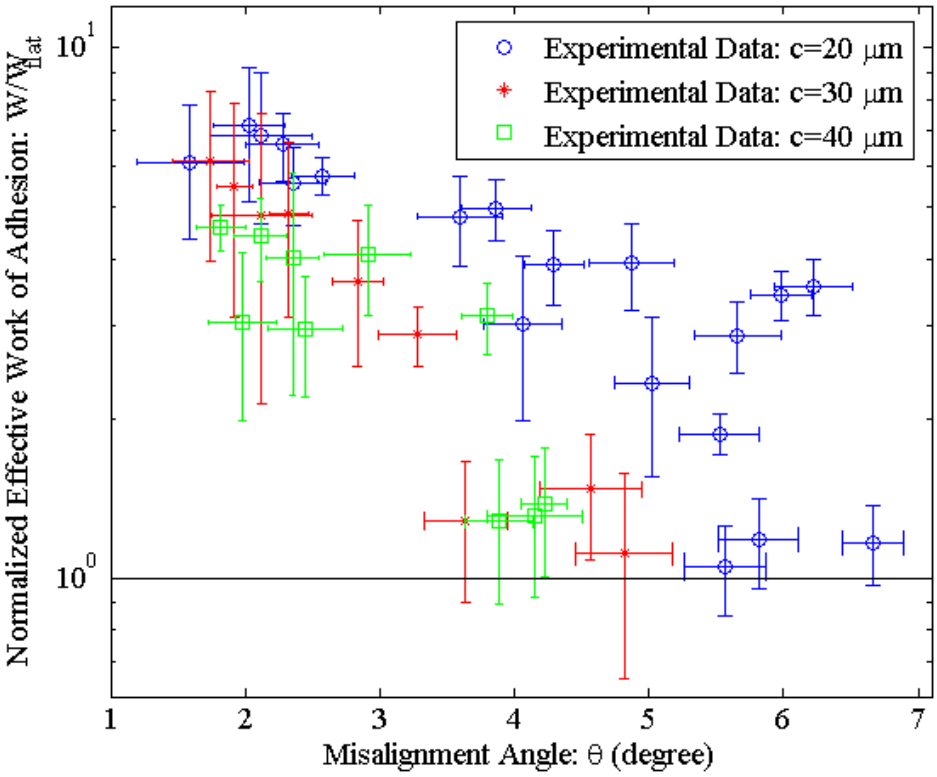

Figure 1.10: Normalized effective work of adhesion for different values of misalignment angle. Error bars represent standard deviation. $W/W_{flat} = 1$ is represented by a horizontal line. All the samples have the same channel depth and width, $d = w = 10\ \mu$m, and the interchannel spacing c is varied from 20 μm to 40 μm.

c [13,24]:

$$E_s = \frac{\mu c^2}{4\pi} \log \frac{2R_o}{b} \tag{1.3}$$

where μ is the shear modulus of PDMS. Eqn. (3) diverges as $b \to 0$, indicating failure of the continuum description near the core. As c increases, eventually its associated strain energy will exceed the adhesion energy of the interface and the interfacial failure (unstable dislocation structure) will occur. An energy release rate balance between work of separating the interface, $E_\gamma = (2R_o - b)W$, where W is effective work of adhesion between complementary surfaces, and the strain

energy from Eqn. (3) (both per unit length) results in a relationship between b and W as follows:

$$dE/db = 0 \quad \rightarrow \quad dE_\gamma/db = dE_s/db \tag{1.4}$$

$$\rightarrow \quad b = \frac{\mu c^2}{4\pi W} \tag{1.5}$$

Using a typical value for shear modulus of PDMS, $\mu = 1.00$ MPa [25], allows for an evaluation of Eqn. (5). Substituting the experimentally measured values of effective work of adhesion, i.e. the results presented in Fig. 8, into Eqn. (5) gives higher values of the widths of the dislocation region than the experimental data, as shown in Fig. 11c. This is because during the adhesion tests, all the elastic energy associated with these dislocations is released to assist crack growth. Thus the experimentally measured work of adhesion, which already includes a negative contribution from the defect structures, has a smaller value than that experienced by the growing dislocation core. A lower bound estimate of the dislocation core width can be obtained by substituting a single value, the experimentally measured value of W for the case $c = 20$ μm, into Eqn. (5). By using a single value, we are neglecting the decrease in W with increasing c; W is overestimated and b is consequently underestimated by Eqn. (5). These two bounds bracket the experimental measurements quite well, establishing the conclusion that the size of the dislocation core is determined by balance of dislocation energy and interfacial adhesion. In particular, note in Eqn. (5) the quadratic dependence on Burgers vector, c.

Some less easily quantifiable sources of energy, such as the strain energy stored in the dislocation core, have been neglected in our calculation. If we consider a spread-out dislocation core instead of the ideal line dislocation, the divergence in Eqn. (3) can be removed [26,27]. A more complete analysis given

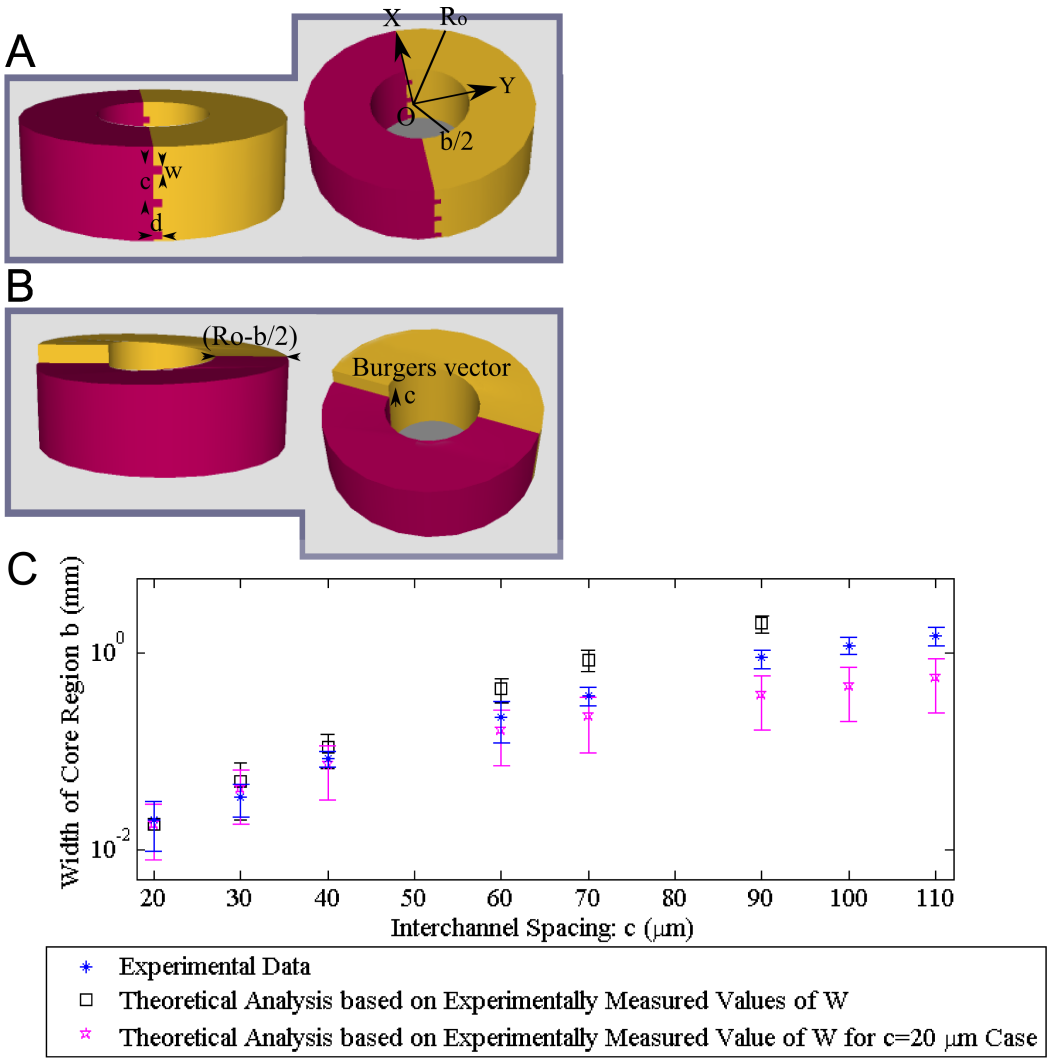

Figure 1.11: (a) A pair of complementary surfaces in perfect alignment. Since the backing layers are very thick in comparison with the value of interchannel spacing c, they can be modeled as infinite elastic blocks. (b) A defect structure viewed as a screw dislocation that carries a Burgers vector with magnitude of interchannel spacing c. (c) The $b - c$ relationship based on Eqn. (5) is compared against experimental data presented in Fig. 4b.

in Appendix A shows that Eqn. (5) remains correct even if we account for the elastic energy of the core. The energy release rate due to dilation of the core region is also addressed in Appendix A.

1.4 Summary of Results

Following experimental indications that rotational misalignment angle is a key factor controlling dislocation pattern and adhesion strength between two micro-structured complementary surfaces, we have carried out a series of well-controlled adhesion tests on complementary surfaces while progressively increasing the misalignment angle.

It has been found that as the misalignment angle increases, the initially almost random distribution of dislocation regions resolves into a periodic pattern, i.e., the dislocation regions are fairly uniformly distributed over the entire interface, including the edges and corners, and as a result local/global misalignment angles can be estimated through examination of the local/global Moire patterns. On the other hand, the local geometric properties of dislocation region, such as the widths of the dislocation region and the core region, and the dilation of the core region, depend only on the characteristic lengths of the rectangular-toothed channel pattern, not on the misalignment angle, which means that the angular misalignment affects only the dislocation distribution, not the internal structure.

Experimental results show that direct interaction of a propagating crack with stationary or quasistationary dislocations can generate substantial crack front deflections, and as a result, the shape of the debonded region is strongly influenced by the distribution and orientation of the pre-existing dislocations. Adhesion between complementary interfaces, as measured by energy release rate required to propagate an interfacial crack, can be enhanced by up to 30 times compared to a flat control depending on the misalignment angle. The relationship between the local geometric features of the dislocation structure and inter-

facial adhesion strength between complementary surfaces can be obtained from an energy release rate balance analysis. We have only studied complementary surfaces in this work. Previous work has shown that, with a few exceptions, adhesion between non-complementary surfaces is very low [13].

It is interesting to note the difference in role played by dislocations in our structures compared to those in metals. In the latter case, dislocations are generated and move under applied stress, causing plastic deformation and associated dissipation. Here, on the other hand, dislocations are immobile. The elastic energy they store is available to propagate the interfacial crack separating adhering surfaces. Therefore, although they accommodate misorientation, dislocations degrade the adhesive strength of the interface. The dislocation patterning process is interesting both as a tool for fundamental and technological studies of defect structures and for its potential in applications in material science.

CHAPTER 2

ADHESION SELECTIVITY BY ELECTROSTATIC COMPLEMENTARITY: TWO DIMENSIONAL ANALYSIS

2.1 Introduction

Adhesion selectivity[*] via complementarity involves matching of pairs of surfaces endowed with certain properties allowing many interaction modes to occur so that any competitive combination other than the resulting aggregate is rejected. Nature presents various types of complementarities, e.g. shape, charge, magnetic, and hydrogen-bonding, all of which are important features for recognition [1–10]. For example, for protein-protein recognition, the topology of the two surfaces and the nature of interacting atom groups are essential [29]. Although the physical principles of complementarities in nature are quite well understood, the deliberate control of adhesion selectivity of material surfaces by complementarity has not been much studied because of the complexity of the systems involved. In Part I of this article, the possibility of adhesion selectivity between two flat surfaces with striped patterns of alternating positive and negative surface charges separated by an electrolyte was analyzed using a one dimensional model. It was shown that strong adhesion can be achieved by exact complementarity between two such pattern-charged surfaces. It was also shown that deformability of the materials strongly alters adhesion selectivity. Specifically, by allowing the surfaces to deform, many more compositions are found to have good adhesion.

[0*]The final version of this paper has been published as: Congrui Jin, Ying Bai, Anand Jagota and Chung-Yuen Hui 2011 Adhesion selectivity by electrostatic complementarity. II. Two-dimensional analysis. Journal of Applied Physics 110 054903

The charged system being studied is shown schematically in Fig. 1. In Part I of this work, it was assumed that the electrostatic interaction between the two charged strips is zero if they are not directly facing each other. In addition, their interaction per unit area is quantified by the solution of two infinite flat surfaces with fixed and uniform surface charge densities. For example, the electrostatic field at any point within Strip A, as shown in Fig. 1, is given by the interaction between Strip A and Strip B, ignoring the interaction with all the neighbors of Strip A on the same plate as well as all the neighbors of Strip B in the other plate.

By a priori making the approximation in Part I that a model based on one-dimensional electrostatic interactions is adequate, we were unable to specify if and under what conditions of geometrical and materials parameters the approximation is valid. For example, the 1D solution neglects to satisfy electrochemical equilibrium in the plane of the surfaces and the consequences of this approximation on the accuracy of the 1D model are not clear. The objective of the theoretical work presented in this article is to examine the predictions of the one dimensional model presented by Part I and to understand the validity of its application in experiments with different choices of material and geometrical parameters, such as dielectric constants, stripe dimensions and separation between the surfaces. The strength of our analysis relies on the comprehensive two dimensional analysis of different factors contributing to the interaction force and energy between two pattern-charged surfaces.

Our 2D solution for the electrostatic fields between charged surfaces is also applicable to other problems of physical and practical interest. For example, there are several known techniques for separation of charged and uncharged dielectric particles that rely on flow near spatially varying fixed surface charges

[30,31]. The specific solution we obtain for the electrostatic fields between surfaces with periodic distributions of charge would allow analysis and design of processes for the separation of charged and uncharged particles. For example, if one had a dispersion of charged bacterial particles and uncharged viral particles in water, the charged particles would be attracted electrophoretically to the surface while uncharged dielectric particles (with dielectric constant typically much smaller than that of the aqueous medium) would be repelled towards the center of the gap between two surfaces [32].

This paper is organized as follows: first, after setting up the problem and clarifying our notation, an exact and general analytical expression for the electric potential between two periodically charged plates immersed in an electrolyte solution is derived in two dimensional configuration; second, this expression is used to derive in a consistent manner expressions for the interaction force and energy; finally, numerical results are presented and compared with the analysis in Part I to examine the applicability and effectiveness of the one-dimensional formulation. The difference between the one-dimensional and two-dimensional models is investigated in detail.

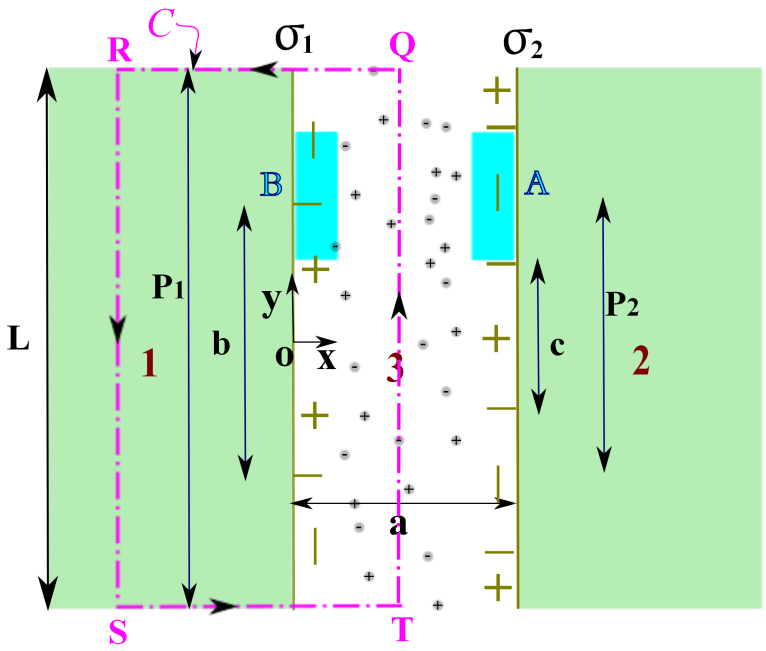

Figure 2.1: Schematic diagram of two charged plates placed parallel at a distance of a. Two infinitely long surfaces with striped patterns of alternating positive and negative charges. ($NP_1 = MP_2$. In this figure, $N = 1$ and $M = 2$.) The surface comprises repeats of a periodic unit cell with length $L = NP_1 = MP_2$.

2.2 Problem Formulation

2.2.1 Equations Governing Electrostatic Interaction between Two Charged Plates

The geometry is shown in Fig. 1: two flat, parallel, charged plates, infinitely long in the y-direction and the out-of-plane direction, have fixed surface charge densities, σ_1 and σ_2, that are periodic functions of y. The spacing between the two plates is denoted by a. The electrolyte inside the gap is denoted as Medium 3. The dielectric constants of the two plates, i.e. Medium 1 and Medium 2, are denoted by ϵ_1 and ϵ_2, which are typically small compared to that of the electrolyte, i.e. ϵ_3. Throughout this paper, subscript i is used to designate physical quantities that belong to Medium i (i = 1, 2 or 3).

As in Part I, we computed the electrostatic fields in Medium 3 using the Debye-Huckel (DH) theory [33]. Note that in Medium 1 and Medium 2 where the charge density is zero, the distribution of potential ϕ is governed by Laplace equation. The governing equations are:

$$\nabla^2\phi_1 = 0, \quad x < 0 \tag{2.1}$$

$$\nabla^2\phi_3 = \frac{\phi_3}{l_D^2}, \quad 0 < x < a \tag{2.2}$$

$$\nabla^2\phi_2 = 0, \quad x > a \tag{2.3}$$

where l_D is the Debye screening length [16].

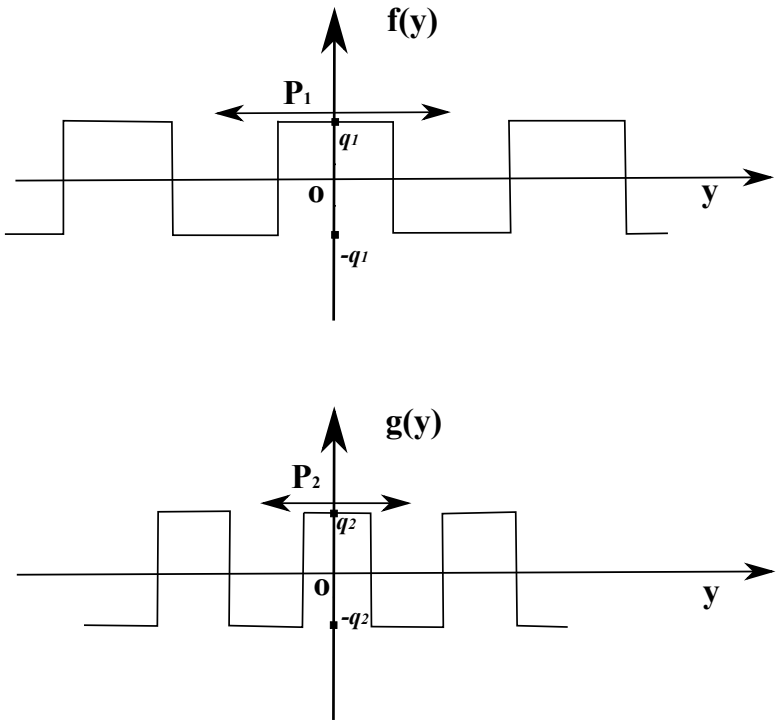

Figure 2.2: Patterns of charge densities on two charged plates.

On the interfaces $x = 0$ and $x = a$, there are fixed surface charges:

$$\sigma_1(x = 0) = f(y) \tag{2.4}$$

$$\sigma_2(x = a) = g(y) \tag{2.5}$$

Continuity of electric potentials and displacements normal to the interfaces lead to the following boundary conditions

$$\phi_1(x = 0) = \phi_3(x = 0) \qquad \phi_3(x = a) = \phi_2(x = a) \tag{2.6}$$

$$(\epsilon_1\phi_{1,x} - \epsilon_3\phi_{3,x})|_{x=0} = \sigma_1 \qquad (\epsilon_3\phi_{3,x} - \epsilon_2\phi_{2,x})|_{x=a} = \sigma_2 \tag{2.7}$$

Without loss in generality, we assume that the charge density on the plate at $x = 0$ is an even function of y, with period $P_1 = 2c$. For the time being, we assume that the two charge distributions are perfectly aligned (see Fig. 1),

so that the charge density on the plate at $x = a$ is of the same form but with different period, $P_2 = 2b$, and amplitude.

Periodicity allows the charge densities to be represented as the Fourier series with coefficients A_n and B_n respectively.

$$f(x) = \Sigma_{n=0}^{\infty} A_n \cos(2n\pi y/P_1) \tag{2.8}$$

$$g(y) = \Sigma_{n=0}^{\infty} B_n \cos(2n\pi y/P_2) \tag{2.9}$$

$$A_n = \frac{2}{P_1} \int_{-P_1/2}^{P_1/2} f(y) \cos(2n\pi y/P_1) dy \quad n = 1, 2... \tag{2.10}$$

$$B_n = \frac{2}{P_2} \int_{-P_2/2}^{P_2/2} g(y) \cos(2n\pi y/P_2) dy \quad n = 1, 2... \tag{2.11}$$

$$A_0 = \frac{1}{P_1} \int_{-P_1/2}^{P_1/2} f(y) dy \tag{2.12}$$

$$B_0 = \frac{1}{P_2} \int_{-P_2/2}^{P_2/2} g(y) dy \tag{2.13}$$

So far, we have assumed that the two distributions are perfectly aligned. In the following, we allow the distribution $g(y)$ to be shifted by $0 < s < P_2$ relative to the distribution $f(y)$, i.e. $g(y) \rightarrow g(y+s)$. After this shift, the charge distribution at $x = a$ has the form:

$$f(x) = \Sigma_{n=0}^{\infty} B_n \cos(2n\pi y/P_2 + \theta_n) \tag{2.14}$$

$$\theta = 2\pi s/P_2, \quad \theta_n = n\theta, \quad 0 < \theta < 2\pi \tag{2.15}$$

To reduce the number of material and geometric parameters, we normalized distances by the Debye screening length l_D, the potentials by $A_1 l_D/\varepsilon_3$ and denote the ratios of dielectric constants by γ_1 and γ_2, respectively.

$$\bar{\phi}_1 = \frac{\varepsilon_3 \phi_1}{A_1 l_D} \quad \bar{\phi}_3 = \frac{\varepsilon_3 \phi_3}{A_1 l_D} \quad \bar{\phi}_2 = \frac{\varepsilon_3 \phi_2}{A_1 l_D} \tag{2.16}$$

$$\bar{y} = \frac{y}{l_D} \quad \bar{x} = \frac{x}{l_D} \quad \bar{a} = \frac{a}{l_D} \quad \gamma_1 = \frac{\epsilon_1}{\epsilon_3} \quad \gamma_2 = \frac{\epsilon_2}{\epsilon_3} \tag{2.17}$$

$$\bar{b}_n = \frac{2\pi n l_D}{P_1} \quad \bar{c}_n = \frac{2\pi n l_D}{P_2} \quad \nu_{1n} = \sqrt{\bar{b}_n^2 + 1} \quad \nu_{2n} = \sqrt{\bar{c}_n^2 + 1} \tag{2.18}$$

2.2.2 Electric Potential

The potential in each medium can be represented by an infinite series of elementary functions $\bar{\phi}_i^{(n)}$:

$$\bar{\phi}_i = \Sigma_{n=0}^{\infty} \bar{\phi}_i^{(n)}, \quad i = 1, 2, 3 \tag{2.19}$$

$$\bar{\phi}_1^{(n)} = C_{1n} \cos(\bar{b}_n \bar{y}) \exp(\bar{b}_n \bar{x}) + C_{2n} \cos(\bar{c}_n \bar{y} + \theta_n) \exp(\bar{c}_n \bar{x}) \tag{2.20}$$

$$\begin{aligned} \bar{\phi}_3^{(n)} = {} & C_{1n} \cos(\bar{b}_n \bar{y})[\cosh(\nu_{1n} \bar{x}) + C_{3n} \sinh(\nu_{1n} \bar{x})] + \\ & C_{2n} \cos(\bar{c}_n \bar{y} + \theta_n)[\cosh(\nu_{2n} \bar{x}) + C_{4n} \sinh(\nu_{2n} \bar{x})] \end{aligned} \tag{2.21}$$

$$\begin{aligned} \bar{\phi}_2^{(n)} = {} & C_{1n} \cos(\bar{b}_n \bar{y})[\cosh(\nu_{1n} \bar{a}) + C_{3n} \sinh(\nu_{1n} \bar{a})] \exp[-\bar{b}_n(\bar{x} - \bar{a})] + \\ & C_{2n} \cos(\bar{c}_n \bar{y} + \theta_n)[\cosh(\nu_{2n} \bar{x}) + C_{4n} \sinh(\nu_{2n} \bar{x})] \exp[-\bar{c}_n(\bar{x} - \bar{a})] \end{aligned} \tag{2.22}$$

2.2.3 Interaction Force and Energy

In this section we derive an expression for the interaction force between the two plates. The volume charge density can be represented as $\rho_v = \rho_v^m + \rho_v^f$, where the superscripts m and f refer to the mobile and fixed charge components. The distribution of the mobile charges is affected by thermal motion, i.e., they are subject to thermodynamic averaging, and their mean position is yet to be determined. On the other hand, fixed charges are not subject to the averaging,

and their positions are assumed to be known exactly. Sharp and Honig [35] have shown that

$$G = \int_V [\rho_v^f \phi + \frac{\rho_v^m \phi}{2} - \frac{\epsilon}{2}(\nabla\phi)^2] dv \tag{2.23}$$

represents the total free energy of the system. The term $\int_V \rho_V^f \phi dv$ can be rewritten as either a surface integral $\int_S \rho_S^f \phi ds$, or a summation $\Sigma q_j \phi_j$ depending on whether ρ_V^f is represented as a smeared surface charge or as a collection of point charges q_j. In our problem, the fixed charges are the surface charges, σ_1 and σ_2, on the interfaces $S_1 : x = 0$ and $S_2 : x = a$.

With the aid of the electrostatic identity:

$$\int_V \frac{\epsilon}{2}(\nabla\phi)^2 dv = \int_V \frac{\rho_v \phi}{2} dv = \int_V \frac{(\rho_v^m + \rho_v^f)\phi}{2} dv \tag{2.24}$$

which is an expression of Gausss law [35], the electrostatic free energy is simplified to

$$G = \int_V \frac{\rho_v^f \phi}{2} dv = \int_{S_1} \frac{\rho_{S_1}^f \phi}{2} ds + \int_{S_2} \frac{\rho_{S_2}^f \phi}{2} ds \tag{2.25}$$

As in Part I of this work, the surface comprises of repeats of a periodic unit cell with length L, that is, the periods satisfy the relation:

$$L = NP_1 = MP_2 \tag{2.26}$$

where N and M are positive integers with no common divisors other than unity. The interaction energy W can be computed by calculating the work done per unit area as follows:

$$W \equiv \frac{Work}{Area} = \frac{1}{L} \int_0^L \frac{\rho_{S_1}^f \phi_{S_1} + \rho_{S_2}^f \phi_{S_2}}{2} dy \tag{2.27}$$

where we assume that each surface has thickness h out-of-plane. The normalized interaction energy is defined by

$$\bar{W} \equiv \frac{\epsilon_3 W}{A_1^2 l_D} = \frac{1}{\bar{L}} \int_0^{\bar{L}} \frac{\rho_{S_1}^f \bar{\phi}_{S_1} + \rho_{S_2}^f \bar{\phi}_{S_2}}{2A_1} d\bar{y}, \quad \bar{L} = \frac{L}{l_D} \tag{2.28}$$

The interaction force per unit area f is defined as follows:

$$f \equiv -\frac{dW}{da} \tag{2.29}$$

A positive sign indicates that the force is repulsive, while a negative sign indicates it is attractive. In normalized form, the interaction force is

$$\bar{f} \equiv \frac{\epsilon_3 f}{A_1^2} = -\frac{d\bar{W}}{d\bar{a}} \tag{2.30}$$

2.3 Interaction between Rigid Surfaces with Striped Patterns of Charge

2.3.1 Comparison between One Dimensional and Two Dimensional Models

So far our result is valid for any form of surface charge densities that are even periodic functions. To make contact with Part I, we specialize to the case where the charge densities are step functions, as shown in Fig. 2, which gives

$$A_0 = 0, \quad A_n = \frac{4q_1}{\pi n}\sin(\frac{n\pi}{2}), \quad n = 1, 2, ... \tag{2.31}$$

$$B_0 = 0, \quad B_n = \frac{4q_2}{\pi n}\sin(\frac{n\pi}{2}), \quad n = 1, 2, ... \tag{2.32}$$

where q_i are the maximum value of σ_i ($i = 1, 2$). Note that in Part I of this work, we only consider the case where $q_1 = q_2$. In the following we use subscripts 1D and 2D to represent the results of one dimensional (Part I) and two dimensional models respectively. For arbitrary combinations of M and N, there are two cases: (i) either M or N is even, (ii) both M and N are odd. We first consider case (i).

Case (i): either M or N is even

For this case, both the interaction force $\bar{f}_{2D}$ and energy $\bar{W}_{2D}$ are independent of θ (the amount of shift between two aligned charge distributions). They are:

$$\bar{f}_{2D} = \frac{1}{4}\Sigma_{n=1,3,5...}^{\infty}[C_{1n}^2\nu_{1n}^2(1-C_{3n}^2) + C_{2n}^2\nu_{2n}^2(1-C_{4n}^2)] \tag{2.33}$$

$$\bar{W}_{2D} = \frac{1}{4}\Sigma_{n=1,3,5...}^{\infty}(A_nC_{1n}/A_1 + B_nC_{2n}/A_1) \tag{2.34}$$

It shows that the overall interaction force is always repulsive, and the interaction force and energy do not depend on θ. These findings are consistent with the results in Part I. The corresponding results obtained in Part I are:

$$\bar{F}_1 = \frac{1}{\sinh^2(\bar{a})} \tag{2.35}$$

$$\bar{W}_1 = \frac{2}{e^{2\bar{a}}-1} \tag{2.36}$$

Fig. 3(a) plots $\bar{f}_{1D}$ and $\bar{f}_{2D}$ as functions of $\bar{a}$. Fig. 3(b) plots $\bar{f}_{1D}$ and $\bar{f}_{2D}$ when $q_1 = q_2$. It shows that when $\bar{b}_1$ increases, i.e. P_1 decreases, the difference between $\bar{f}_{1D}$ and $\bar{f}_{2D}$ becomes larger. Fig. 3(c) plots $\bar{f}_{1D}$ and $\bar{f}_{2D}$ for the case $N = 1$, $M = 2$, 64, 128 and 256. Nevertheless, the 2D and 1D predictions are practically identical when $\bar{a} > 3$, that is, when the separation is greater than three times the Debye length. These results are consistent with our assumptions in part I.

Case (ii): both M and N are odd

For this case both the interaction force $\bar{f}_{2D}$ and energy $\bar{W}_{2D}$ depend on θ (the amount of shift between two aligned charge distributions, see Fig. 2). Fig. 4 plots $\bar{f}_{2D}$ as a function of θ for different combinations of M and N. It shows that $\bar{f}_{2D}$ is symmetrical with respect to $\theta = \pi$ for any M and N combination. This is as expected since $\bar{f}_{2D}(\theta) = \bar{f}_{2D}(\theta + \pi)$ and $\bar{f}_{2D}(\theta) = \bar{f}_{2D}(-\theta)$, which imply that $\bar{f}_{2D}(\pi + \theta) = \bar{f}_{2D}(\pi - \theta)$.

To find $\theta \in [0, \pi]$ where $\bar{f}_{2D}$ achieve its maximum and minimum, we obtain

$$\frac{d\bar{W}_{2D}}{d\theta} = \Sigma_{k=1,3,5,\ldots}^{\infty} \sin(kM\pi/2) \sin(kN\pi/2)[-kN\lambda \sin(kN\theta)] \tag{2.37}$$

$$\frac{d^2\bar{W}_{2D}}{d\theta^2} = \{\Sigma_{k=1,3,5,\ldots}^{\infty} \frac{1}{2} \cos[k\pi/2(M-N)] - \cos[k\pi/2(M+N)]\} \times [-(kN)^2\lambda \cos(kN\theta)] \tag{2.38}$$

Since M and N are both odd, they belong to either Ω_1 or Ω_2, where $\Omega_1 = \{4k + 1; \forall k \in Z\}$ and $\Omega_2 = \{4k + 3; \forall k \in Z\}$, where Z denotes the set of all non-negative integers. We deduce the following situations in Table 1.

The results shown in Table 1 are consistent with the position of maximum/minimum values of the curves shown in Fig. 4. Part I of this work shows that interaction energy is minimized if each unit cell begins with aligned regions of opposite charge. Figs. 5a-5d show situations where "each unit cell begins with aligned regions of opposite charge". Fig. 5a corresponds to the case that $\theta = \pi$ when $M \in \Omega_1$ and $N \in \Omega_1$, or $M \in \Omega_2$ and $N \in \Omega_2$ (Fig. 5b). Fig. 5c corresponds to the case that $\theta = 0$ when $M \in \Omega_1$ and $N \in \Omega_2$, or $M \in \Omega_2$ and $N \in \Omega_1$ (Fig. 5d). According to the results listed in Table 1, it can be seen that the conclusion obtained from one dimensional analysis is consistent with that obtained from the two dimensional analysis. It should be noted, however, that the scenario where each unit cell begins with aligned regions of opposite charge is not the only favorable configuration for adhesion (minimization of interaction energy). For example, for the case $N = 3$ and $M = 5$, Table 1 shows that the minimum interaction energy occurs at $\theta = 0$ and $\theta = 2\pi/3$.

Fig. 6a plots $\bar{f}_{1D}$ and $\bar{f}_{2D}$. Note that, when $N = 1$ and $M = 3$, Table 1 shows that the interaction energy is minimized when $\theta = 0$. Since $\bar{f}_{2D}$ is symmetrical with respect to $\theta = \pi$, the two curves for $\theta = \pi/2$ and $\theta = 3\pi/2$ overlap. Fig. 6a shows that at $\theta = 0$, $\bar{f}_{1D} = (\pi^2/16)\bar{F}_1$ and $\bar{f}_{2D}$ show good agreement, that is, the

Table 2.1: Local maximum/minimum of interaction energy

$M \in \Omega_1$ and $N \in \Omega_1$	$\theta = 0, 2\pi/N, 4\pi/N,...,(N-1)\pi/N$	$d^2\bar{W}_{2D}/d\theta^2 < 0$, maximum
Or, $M \in \Omega_2$ and $N \in \Omega_2$	$\theta = \pi/N, 3\pi/N,..., \pi$	$d^2\bar{W}_{2D}/d\theta^2 > 0$, minimum
$M \in \Omega_1$ and $N \in \Omega_2$	$\theta = 0, 2\pi/N, 4\pi/N,...,(N-1)\pi/N$	$d^2\bar{W}_{2D}/d\theta^2 < 0$, minimum
Or, $M \in \Omega_2$ and $N \in \Omega_1$	$\theta = \pi/N, 3\pi/N,..., \pi$	$d^2\bar{W}_{2D}/d\theta^2 < 0$, maximum

one dimensional result $\bar{F}_1$ is in good agreement with the two dimensional result when the separation is small in comparison with the period.

The behavior of the curves in Fig. 6a near the minimum is shown in Fig. 6b. It shows that when $\theta = \pi/2$, π and $3\pi/2$, the overall interaction is always repulsive from $\bar{a} = 0$ to 5. However, at $\theta = 0$, at large distances, the interaction is attractive and decreases significantly with distance; at short distances, there is always repulsion, and $\bar{f}_{2D} \to +\infty$ as $\bar{a} \to 0$. This applies to any combination of M and N (when they are both odd) except when $M = N = 1$. Fig. 6b also shows that there is a critical separation $\bar{a}_e$ at which the force becomes zero and the two surfaces will come to rest naturally. We obtain $\bar{a}_e = \cosh^{-1}(MN)$, and for this case $\bar{a}_e \approx 1.77$. This result is also consistent with the analysis in Part I of this work.

Finally, for the special case $M = N = 1$, Table 1 shows that the interaction energy is minimized when $\theta = \pi$. Fig. 7 plots $\bar{f}_{1D}$ and $\bar{f}_{2D}$ for the case $N = M = 1$. It shows that when $\theta = \pi$ the force is always attractive, and within this model the surfaces come to rest in contact.

2.4 Concluding Remarks

To investigate the possibility to achieve high selectivity using relatively smooth and flat extended surfaces patterned with stripes of charge, we have analyzed the interaction force and energy between two such surfaces in a two-dimensional configuration. We have shown that strong adhesion can be achieved by exact complementarity between two such pattern-charged surfaces. In the limit of small separations or large periods, the interaction force between the two surfaces in our 2D analysis is found to differ from the prediction of the 1D model in Part I of this work by a constant factor of $\pi^2/16 \approx 0.6$. Thus, the 1D and 2D analysis can be brought into perfect agreement in this limit by a simple rescaling of the interaction force. Using this rescaling, we have found that most of the 1D predictions are in good agreement with our 2D model. However, there are some differences between the two models, for example, we show that the situation where a unit cell begins with aligned region of opposite charge is not the only favorable configuration for adhesion. Our 2D solution can be applied to experiments with different choices of material and geometrical parameters. These findings can assist researchers in designing and implementing experiments on deliberate control of adhesion selectivity of pattern-charged surfaces by complementarity. In addition, the closed-form solution for electrostatic fields between surfaces with fixed periodic charge distribution is applicable to several physical phenomena and applications involving the electrophoretic and dielectrophoretic separation of charged and uncharged particles.

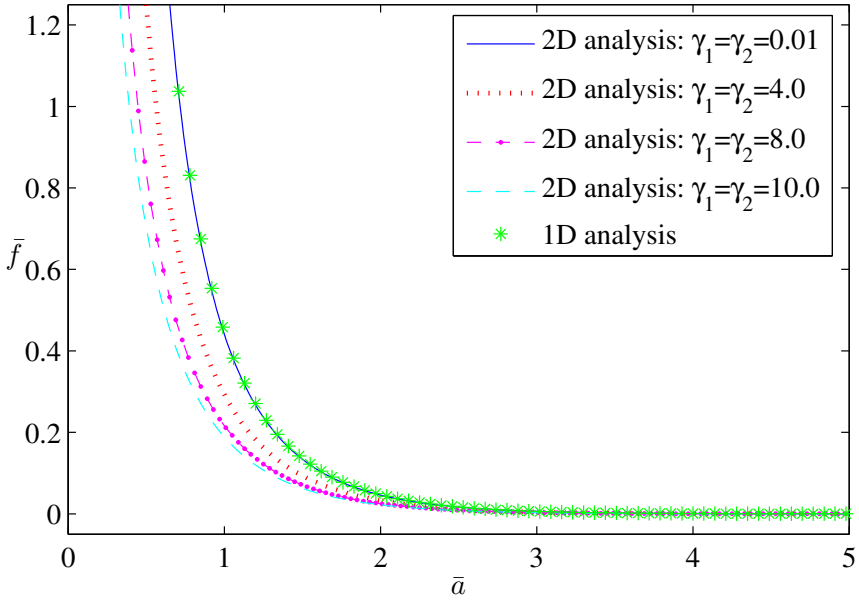
2D analysis: γ1=γ2=0.01
2D analysis: γ1=γ2=4.0
2D analysis: γ1=γ2=8.0
2D analysis: γ1=γ2=10.0
1D analysis
$\bar{f}$
$\bar{a}$
0
0.2
0.4
0.6
0.8
1
1.2
0
1
2
3
4
5

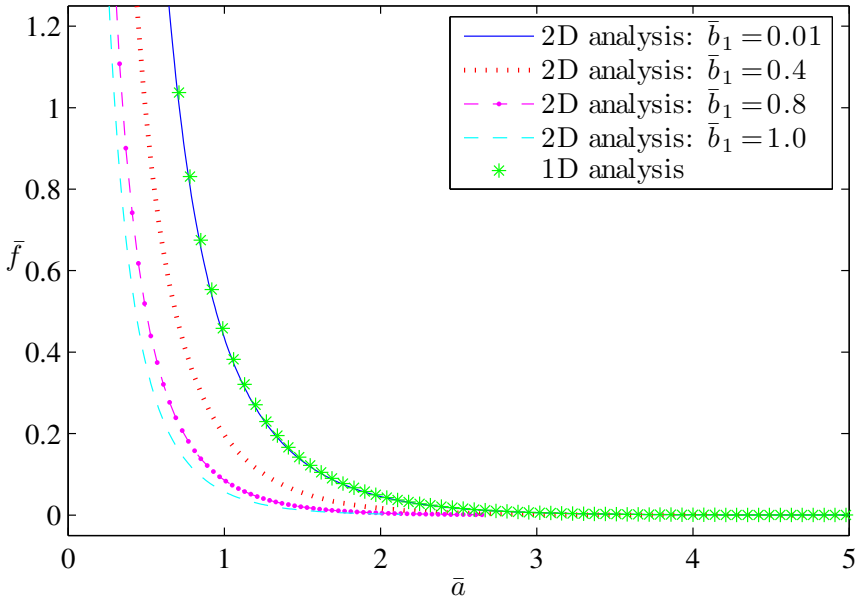
2D analysis: $\bar{b}_1 = 0.01$
2D analysis: $\bar{b}_1 = 0.4$
2D analysis: $\bar{b}_1 = 0.8$
2D analysis: $\bar{b}_1 = 1.0$
1D analysis
$\bar{f}$
$\bar{a}$
0
0.2
0.4
0.6
0.8
1
1.2
0
1
2
3
4
5

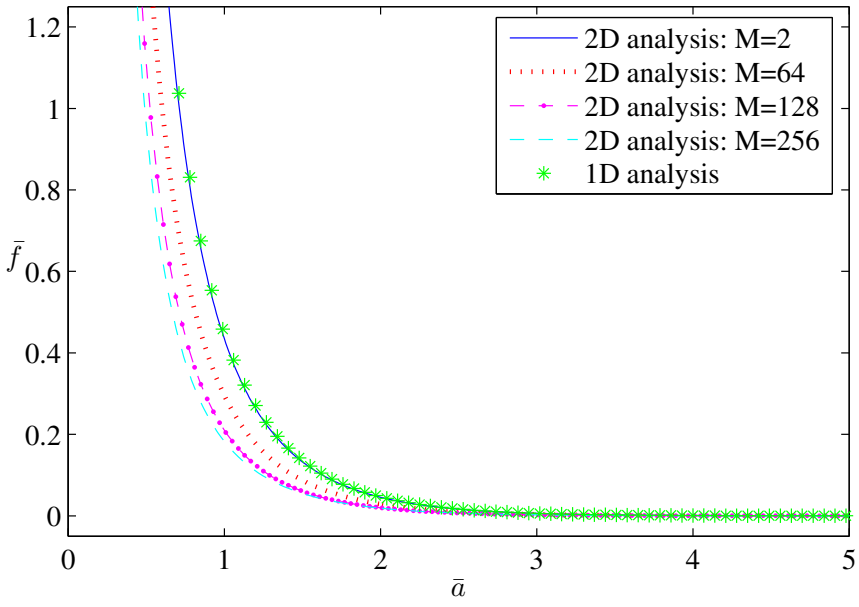

Figure 2.3: (a) $\bar{f}_{1D}$ and $\bar{f}_{2D}$ for the case $q_1 = q_2$, $\bar{b}_1 = 0.01$, $N = 1$, $M = 2$, $\gamma_1 = \gamma_2 = 0.01$, 4.0, 8.0, and 10.0; (b) $\bar{f}_{1D}$ and $\bar{f}_{2D}$ for the case $q_1 = q_2$, $\gamma_1 = \gamma_2 = 0.01$, $N = 1$, $M = 2$, $\bar{b}_1 = 0.01$, 0.4, 0.8, and 1.0; (c)$\bar{f}_{1D}$ and $\bar{f}_{2D}$ for the case $q_1 = q_2$, $\bar{b}_1 = 0.01$, $\gamma_1 = \gamma_2 = 0.01$, $N = 1$, $M = 2$, 64, 128, and 256.

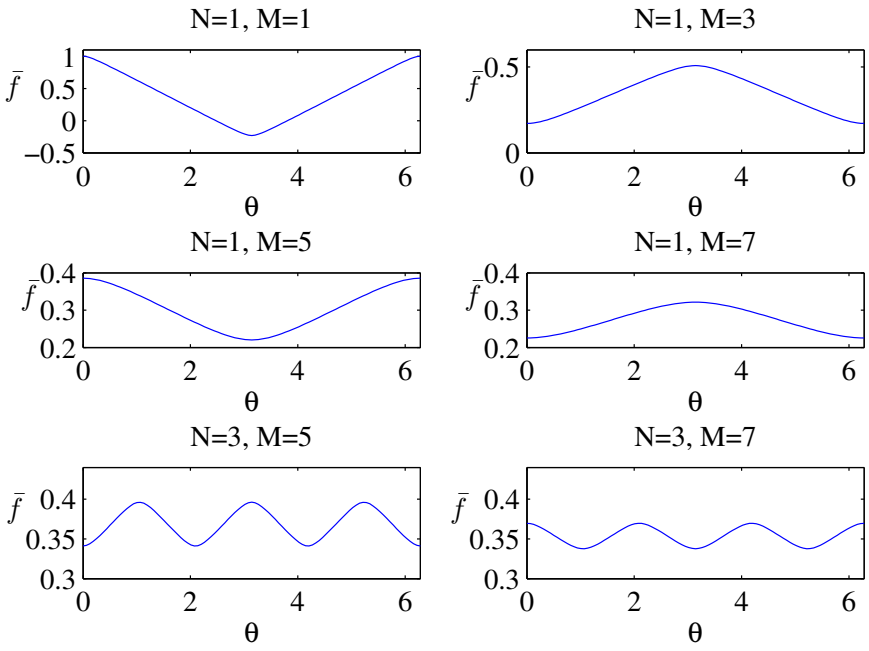

Figure 2.4: $\bar{f}_{2D}$ as a function of θ for the case $q_1 = q_2$, $\bar{a} = 1.0$, $\gamma_1 = \gamma_2 = 0.1$, $\bar{b}_1 = 0.1$ for different combinations of M and N.

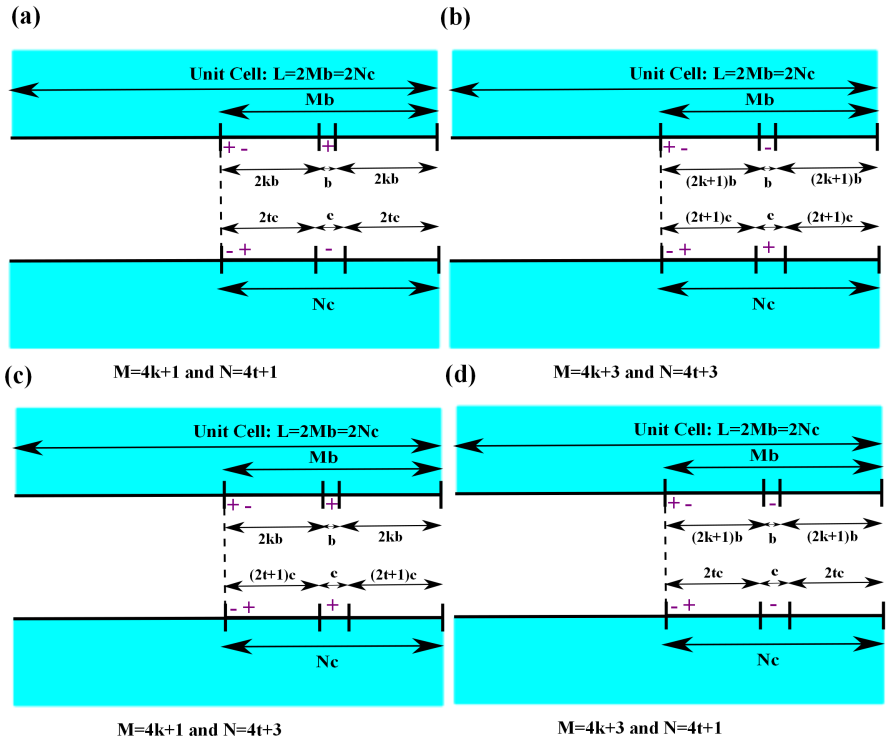

Figure 2.5: In 1D analysis, interaction energy is minimized if each unit cell begins with aligned regions of opposite charge. Fig. 5a-d show that this conclusion is consistent with the results from the two dimensional analysis as shown in Table 1.

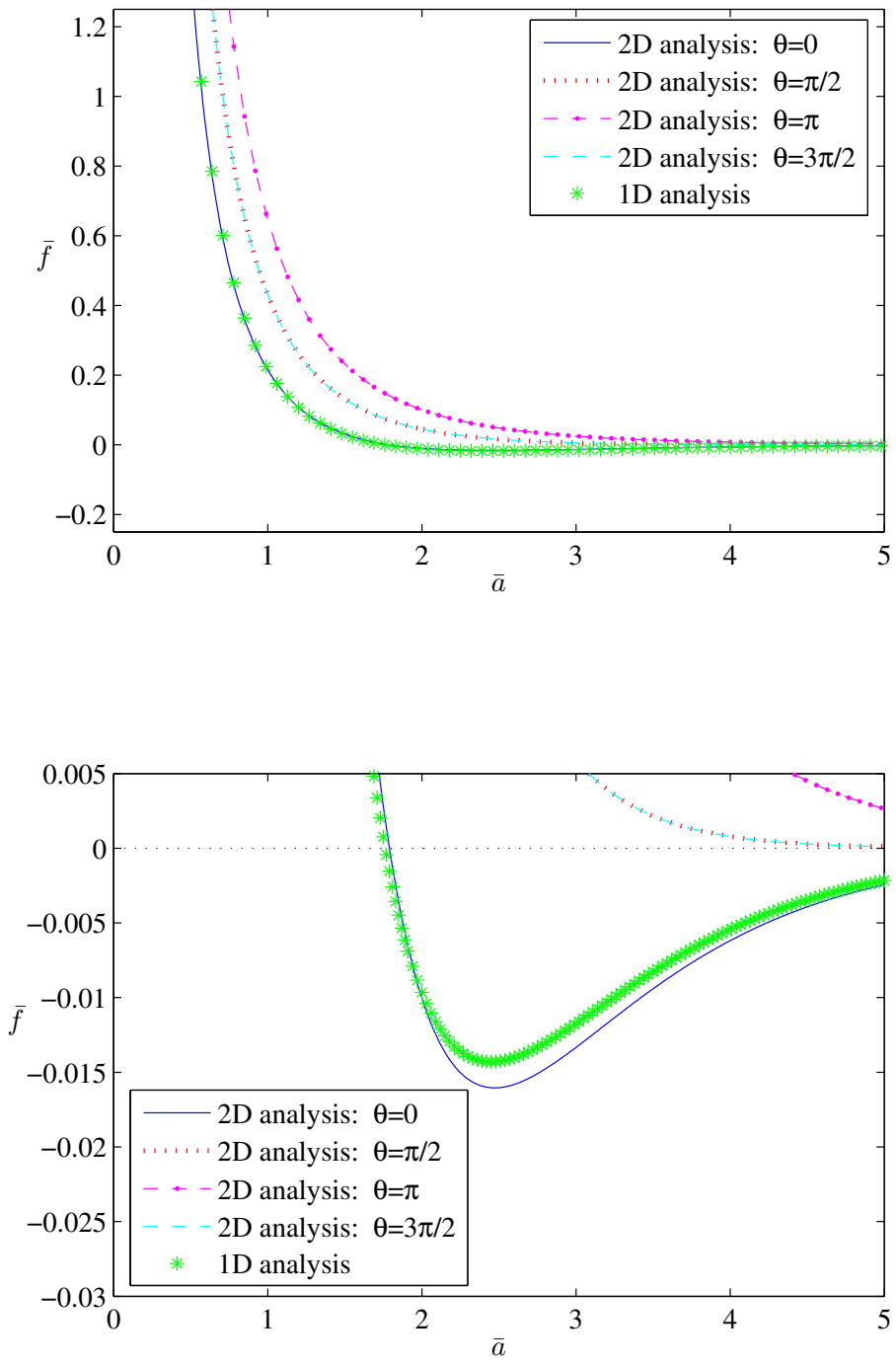

Figure 2.6: $\bar{f}_{1D}$ and $\bar{f}_{2D}$ for the case $q_1 = q_2$, $N = 1$, $M = 3$, $\gamma_1 = \gamma_2 = 0.1$, $\bar{b}_1 = 0.01$ for $\theta = 0, \pi/2, \pi$ and $3\pi/2$: (a) general view; (b) zoomed view.

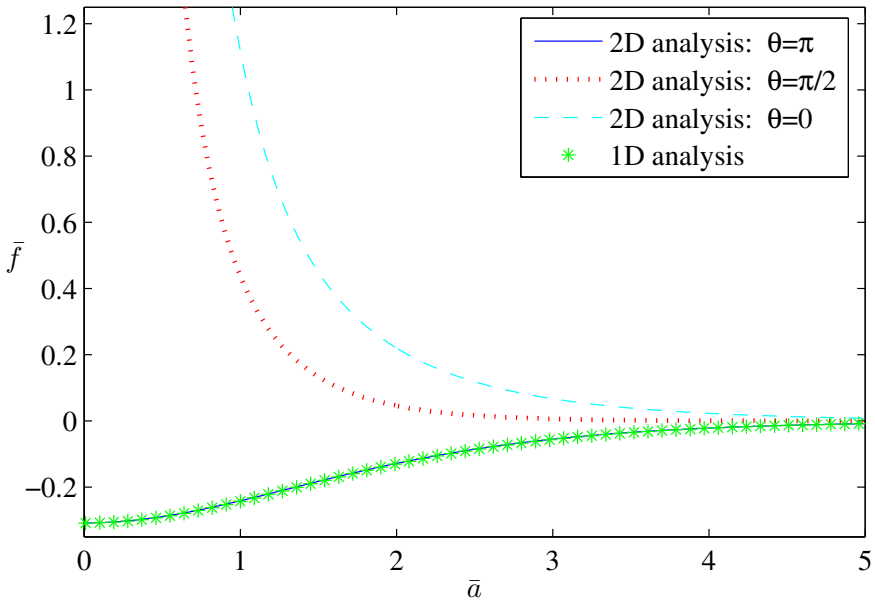

Figure 2.7: $\bar{f}_{1D}$ and $\bar{f}_{2D}$ for the case $q_1 = q_2$, $N = M = 1$, $\gamma_1 = \gamma_2 = 0.1$, $\bar{b}_1 = 0.01$ for $\theta = 0, \pi/2$ and π.

CHAPTER 3

AN EASY-TO-IMPLEMENT NUMERICAL SIMULATION METHOD FOR ADHESIVE CONTACT PROBLEMS INVOLVING ASYMMETRIC ADHESIVE CONTACT

3.1 Introduction

The canonical problem[*] of adhesive contact between two elastic spheres has been studied extensively over the last few decades, in particular, using two continuum mechanics models, namely, the Johnson–Kendall–Roberts (JKR), [37] and the Derjaguin–Muller–Toporov (DMT) models [38, 39]. The JKR model modifies the Hertz equations for the adhesionless contact of elastic spheres by accounting for surface energy. In the JKR theory the surface energies cause an infinite tensile stress to act at the contact edge, while in the DMT theory, the tensile stress is finite in a region outside the contact edge but is zero inside it. The two seemingly contradictory models were reconciled first by Tabor [40] who suggested that they described two extremes of a certain dimensionless parameter (later dubbed the Tabor parameter μ, which is defined later in this paper). Tabor showed that the JKR model is suitable for large, compliant spheres with strong adhesion (where μ is large), while the DMT model applies to small, stiff spheres with weak adhesion (where μ is small). Maugis [41] then developed a closed form solution for the transition between the JKR and DMT models by applying the Dugdale–Barenblatt model to approximate the surface interaction. The parameter used by Maugis, quantifying the transition between the JKR and

[0*]The final version of this paper has been published as: Congrui Jin, Anand Jagota and Chung-Yuen Hui 2011 An easy-to-implement numerical simulation method for adhesive contact problems involving asymmetric adhesive contact. Journal of Physics D: Applied Physics 44 405303

the DMT limit, is commonly referred to as Maugis parameter, which is effectively the same as Tabor parameter μ if one identifies ε (defined later in this paper) in the Tabor parameter with W_{ad}/σ_0 in the Maugis parameter, where W_{ad} is the work of adhesion and σ_0 is the strength of the interface.

The first numerical simulation for the adhesive contact between spheres was presented by Muller et al. in 1980 [42]. They used the Lennard-Jones potential to model surface interaction and showed a continuous transition from the JKR to the DMT theory as the Tabor parameter decreased. More numerical computations were performed by Attard and Parker [43]. They showed a puzzling non-monotonic trend of the pull-off force versus the Tabor parameter, but they did not treat the singular integrands in the governing equation correctly, resulting in their predicted trend and the quantitative validity of their pull-off forces being questioned. A complete numerical solution was obtained by Greenwood [44]. He pointed out the existence of singular integrands in the governing equation and found S-shaped load-approach curves for values of greater than one, leading to jumps into and out of contact. Feng [45,46] proposed a more efficient numerical method and a more accurate treatment of the singular integrands. He used Newton's method to solve the nonlinear equations and applied Keller's algorithm [47,48] of the arc-length continuation to track the solution branches around the turning points to determine the jumping-on and jumping-off behavior. Since spheres are axisymmetric, in all the above numerical computations, the number of nonlinear equations is of order n, where n is the number of elements for tessellation of the problem domain.

There are many important applications in which the contact area is not axisymmetric, e.g. a sphere in contact with a cylinder or two cylinders oriented

at a skew angle. Yang [49] analyzed the adhesive contact between an elliptical rigid flat-ended punch and an elastic half space using the energy method. The separation was found to initiate at the edges of the major axis, which would lead the initially elliptical contact to evolve to a more circular shape. Johnson and Greenwood [50] proposed an approximate JKR theory for the adhesive contact of smooth elastic bodies whose relative radii of curvature are unequal, in which they assumed that the energy release rate is approximately constant along an elliptical contact line. In the following, their model is referred to as elliptical JKR theory.

There are even more challenging but important problems, such as the adhesive contact between rough surfaces, where the contact area is multiply connected and quite irregular. Solving these problems with a general numerical technique, such as the finite element method, is computationally prohibitive. If, as can often be assumed, the surfaces do not deviate strongly from planarity, a significant simplification can be achieved by discretizing only the surface and accounting for interactions between them using known contact Green's functions. Even with this simplification, the absence of radial symmetry presents difficulty in the numerical solution of adhesive contact, since the number of nonlinear equations increases from n to n^2 (see Section 3). To bypass these difficulties, Wu [51] proposed an elegant numerical method to solve an asymmetric adhesive contact problem, which combines the fast Fourier transform, the biconjugate stabilized method, a preconditioning technique and a path-following method. Elliptical adhesive contact was studied experimentally by Sumer et al. [52] utilizing two polydimethylsiloxane (PDMS) cylinders placed at different skew angles with respect to each other. They found that the difference of the maximum adhesion force between experiments and elliptical JKR theory

increased as the contact line went from mildly elliptical to slim elliptical. Despite the feasibility and sophistication of the technique employed by Wu [51], it is complicated to implement and still requires significant computing time and memory resources. In this work, a numerical method, much simpler to implement and as accurate as that introduced by Wu [51], is presented. This method is used to investigate two asymmetric adhesive contact problems: (1) the adhesive contact between a sphere and a long cylinder, as shown in Fig. 1a; and (2) the adhesive contact between two identical long cylinders placed at a skew angle θ with respect to each other [52], as shown in Fig. 1b. While the problems studied in this manuscript each have a single asymmetric contact region, this technique can handle the problems that have multiple arbitrarily shaped contact regions.

3.2 Governing Equations

The equations governing frictionless adhesive interaction between two smooth, isotropic, linearly elastic non-conforming bodies are well known and can be found in Refs. [44, 51, 53]. The implicit assumption is that the contact is small compared with the size of the elastic bodies, and as a result, the initial air gap h_o, interpreted as the separation of the surfaces in the absence of applied and adhesive forces, can be written as

$$h_0 = \frac{1}{2R'}x^2 + \frac{1}{2R''}y^2 \tag{3.1}$$

where R' and R'' are called principal relative radii of curvature. For the two problems to be investigated in this paper

$$h_0 = \frac{x^2}{2R_s} + \frac{y^2}{2R_sR_c/(R_s + R_c)} \quad Problem1 \tag{3.2}$$

$$h_0 = \frac{x^2}{2R_c/(1 - \cos\theta)} + \frac{y^2}{2R_c/(1 + \cos\theta)} \quad Problem2 \tag{3.3}$$

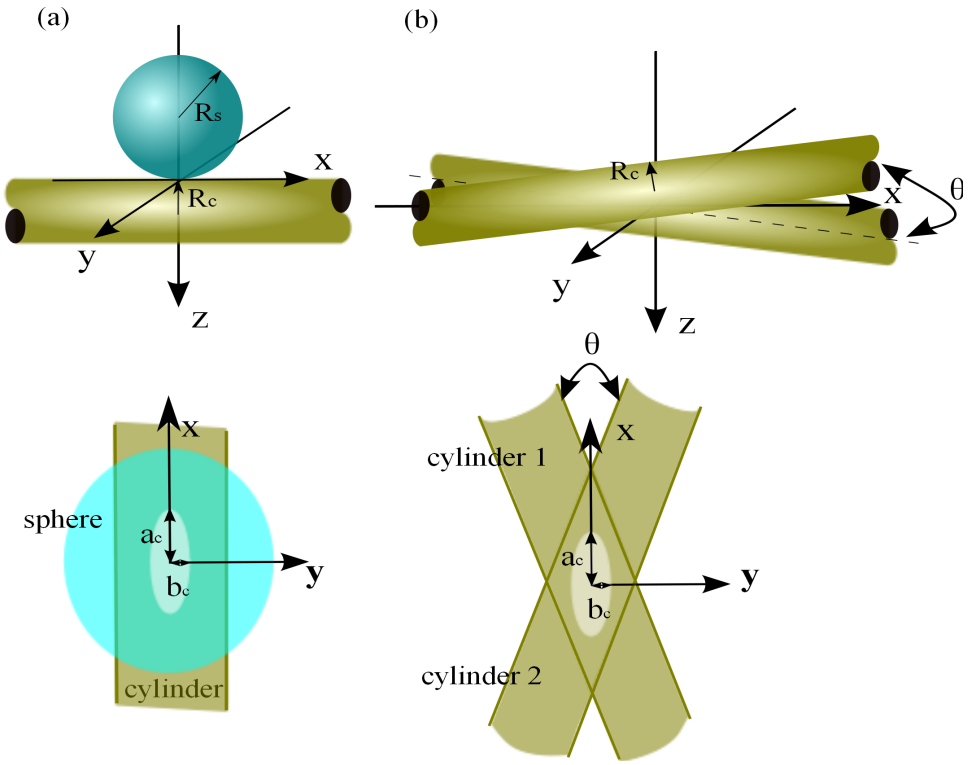

Figure 3.1: Schematic of the two elliptical adhesive contact problems. The contact area is expected to have an elliptical shape as illustrated in the top views. 1a. Adhesive contact between a sphere and a cylinder. 1b. Adhesive contact between two identical cylinders placed at a skew angle θ.

where R_s and R_c are the radius of the sphere and the cylinder respectively. Table 1 shows a summary of the dimensional and dimensionless parameters used in this paper.

In the presence of adhesive forces and external load, the surfaces deform and the separation or air gap between them depends on the surface interaction. As in Ref. [51], surface interaction is assumed to be governed by the Lennard-Jones potential (integrated between one surface and the opposing half space). In dimensionless form, the local pressure P is related to the air gap H by

$$p = \frac{8}{3}[(H+1)^{-9} - (H+1)^{-3}] \tag{3.4}$$

Table 3.1: Summary of dimensional and dimensionless parameters

Dimensional parameters
Equivalent radius: R_e (m)
Initial air gap: h_0 (m)
Air gap after deformation: h (m)
Length on the order of interatomic spacing: ε (m)
Approach of the surfaces: δ (m)
Pressure: p (Nm^{-2})
Effective modulus: E^* (Nm^{-2})
Work of adhesion: W_{ad} (Nm^{-1})
Total normal load: f (N)
Semi-major and -minor axis of the contact line: a_c and b_c (m)
Mean contact radius: $c_c = \sqrt{a_c b_c}$ (m)
Dimensionless parameters
Skew angle: θ (radian)
Ratio of the radii of the sphere and the cylinder: $\beta = R_s/R_c$
Ratio of the principal relative radii of curvature of the bodies: $\lambda = \sqrt{R''/R'}$
Normalized initial air gap between surfaces: $U = h_0/\varepsilon$
Normalized air gap after deformation: $H = h_0/\varepsilon - 1$
Normalized approach or displacement: $D = \delta/\varepsilon$
Normalized pressure: $P = p\varepsilon/W_{ad}$
Tabor parameter: $\mu = (R_e W_{ad}^2/E^{*2}\varepsilon^3)^{1/3}$
Normalized normal load: $F = f/3\pi R_e W_{ad}$ or $F_0 = f/3\pi R_s W_{ad}$
Reference contact radius: $c_r = (9\pi R_e^2 W_{ad}/4E^*)^{1/3}$ or $c_0 = (9\pi R_s^2 W_{ad}/4E^*)^{1/3}$
Normalized mean contact radius: $C = c_e/c_r$ or $C_0 = c_e/c_0$
Normalized approach or displacement: $\Delta = \epsilon R_e/c_r^2$ or $\Delta_0 = \epsilon R_s/c_0^2$
Axes ratio of the ellipse: $g = b_c/a_c$
Eccentricity of the ellipse: $e^2 = 1 - g^2$

Derjaguin's approximation [54], assuming that (4) can be applied for small areas of surfaces even when they are inclined or curved, is used. Following Ref. [51], the normalized air gap after deformation H is related to the pressure distribution P by

$$H = -D + U + \frac{8\mu^{3/2}}{3\pi} \iint_{\Omega} \frac{(H+1)^{-9} - (H+1)^{-3}}{\sqrt{(X-X')^2 + (Y-Y')^2}} dX'dY' \tag{3.5}$$

where Ω is the entire XY plane, μ is the Tabor parameter [40, 55], and U is the normalized initial gap given by

$$U = \frac{1}{2\sqrt{1+\beta}}[X^2 + (1+\beta)Y^2] \quad Problem1 \tag{3.6}$$

$$U = \frac{1}{2\sin\theta}[X^2(1-\cos\theta) + Y^2(1+\cos\theta)] \quad Problem2 \tag{3.7}$$

The dimensionless normal load F acting on the bodies is therefore

$$F = \frac{1}{3\pi} \iint_{\Omega} P(X,Y) dXdY \tag{3.8}$$

3.3 Numerical Method

Since the pressure drops very rapidly as the air gap increases, the region over which the problem is solved, Ω, can be taken to be a finite rectangle $\Omega = [-a, a] \times [-b, b]$. Partition this rectangle into $2N_1 \times 2N_2$ rectangles, each with area ab/N_1N_2. When a mesh element is small enough, the contact pressure at each element can be treated as a constant. Since both problems have symmetry that $P(X,Y) = P(-X,Y) = P(X,-Y) = P(-X,-Y)$, only the rectangle $\Omega = [0,a] \times [0,b]$ needs to be considered. Divide Ω into $N_1 \times N_2$ rectangles Ω_{ij}, assuming that $P(x,y)$ is constant, P_{ij}, in each Ω_{ij}, where

$$P_{ij} = \frac{8}{3}\{[H(X_i, Y_j) + 1]^{-9} - [H(X_i, Y_j) + 1]^{-3}\} \tag{3.9}$$

(5) can be written as

$$H_{kl} = -D + U_{kl} + \frac{\mu^{3/2}}{\pi} C_{ijkl} P_{ij} \tag{3.10}$$

which can be represented in vecter form as

$$\vec{H} = -D + \vec{U} + \frac{\mu^{3/2}}{\pi} C\vec{P} \tag{3.11}$$

Even for moderately small mesh size where $N_1 = N_2 = 100$, the number of elements of C is 10^8, and thus computation can rapidly become intractable. To solve (11) numerically, a virtual state relaxation method by interposing a virtual dash-pot in the mechanical system described by (11) is proposed. Then (11) is transformed into the following evolution equation for the dynamical system defined by

$$\frac{d\vec{H}}{dt} + \vec{H} = -D + \vec{U} + \frac{\mu^{3/2}}{\pi} C\vec{P} \tag{3.12}$$

For large separations the surface forces are weak and barely deform the surfaces, thus one can start with an initial condition of $\vec{H} = -D + \vec{U}$ to obtain the solution in the next time step. The basic idea is that D is gradually increased and the H vector obtained from the previous step is used as the initial guess for computing H in the next step. In each step, let time evolve until equilibrium is reached within a prescribed tolerance. This method yields only the stable equilibria for each D, and thus the load-displacement curves are discontinuous at unstable jumps. All the numerically generated force-displacement curves in this paper are obtained by a two-stage process: one as D increases from minimum to the maximum displacement, and the other one as it decreases back to the minimum. The two numerical stages essentially generate the two experimentally measured force-displacement branches, i.e. approach and detachment, under displacement-controlled loading.

While it has not been mathematically proved that the above numerical procedure will always converge to the correct equilibrium solution, irrespectively of initial conditions, important insight on how this numerical procedure works can be understood by considering a one dimensional version of (12). For this case, it is convenient to rewrite (12) as

$$dx/dt = c_1\phi(x) - (x + c_2) \equiv f(x) \quad x > -1 \tag{3.13}$$

where

$$\phi(x) \equiv [(x + 1)^{-9} - (x + 1)^{-3}] \tag{3.14}$$

The nonlinear ordinary differential equation (13) can be viewed as representing a nonautonomous dynamical system in which x can be interpreted as the position of a particle. The function f defined by (13) specifies the particle velocity dx/dt at each position x. It can be shown that, for $c_1 < c_1^*$ (small Tabor parameter), f is strictly decreasing resulting in exactly one stable equilibrium or fixed point (see Fig. 2a). When $c_1 > c_1^*$ (large Tabor parameter), f first decreases rapidly, then increases to a maximum, and then decreases monotonically. For this case, the number of fixed points depends on c_2 (see Figs. 2b-2d). It is easy to show that, as c_2 falls below a critical point c_2^*, whose value depends on c_1, a new fixed point materializes and splits into two, one stable and one unstable (see Fig.2c). This is called a saddle-node bifurcation at $c_2^*(c_1)$. As a result, there are three fixed points, two are stable and the middle one is unstable (see Fig. 2c). Further decreasing c_2 results in another saddle-node bifurcation where the middle unstable fixed point and the stable fixed point on the left move towards each other, collide, and mutually annihilate. Thus, for c_2 sufficiently negative, there is only one fixed point (see Fig. 2d). This behaviour is summarized in Fig. 2, the phase portrait of the dynamical system, where $\dot{x}$ is plotted against x and the direction of flow near the fixed point(s) is indicated. This portrait shows

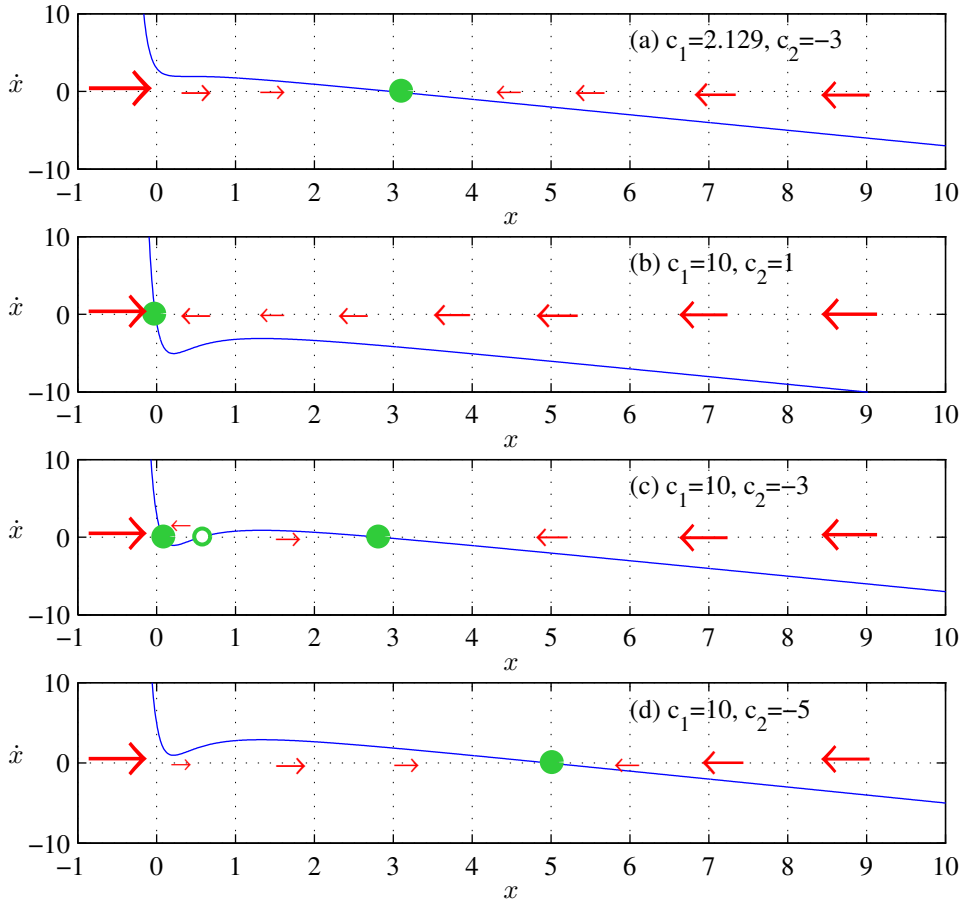

Figure 3.2: Illustration of stable (solid dots) and unstable (open dots) equilibrium points associated with (13) and (14). Arrows indicate the direction of the flow.

that, for a given initial condition, the relaxation method allows the dynamical system to evolve to these stable equilibrium solutions. Fig. 2 shows that the long time solution converges to the stable fixed points irrespective of the initial condition.

To check this method, the problem of adhesive contact between a sphere and a half-space is solved, and it shows that the results are consistent with Wu's

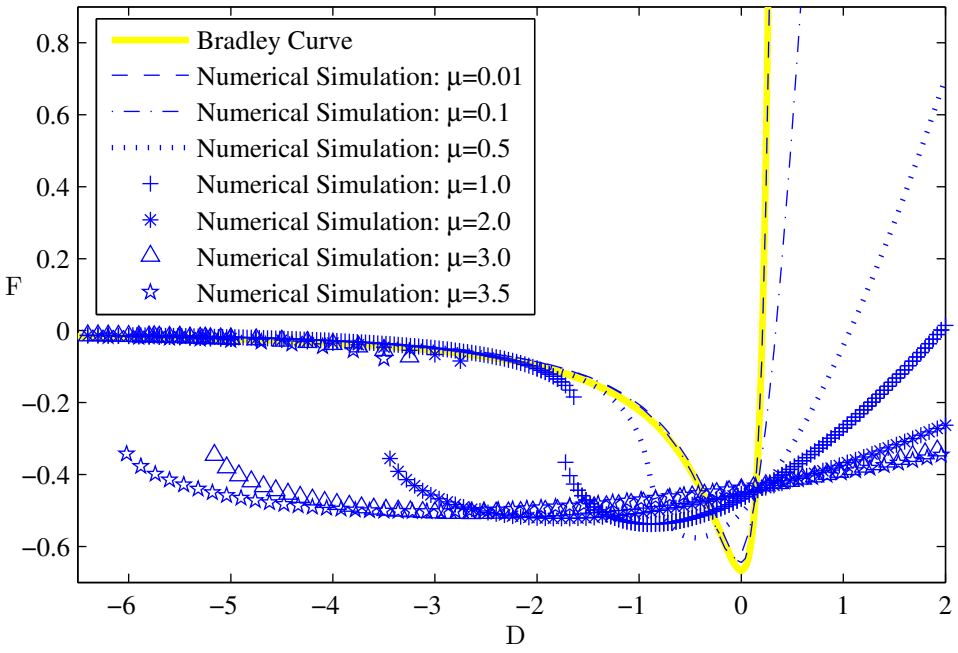

Figure 3.3: Numerical results for normalized load F versus normalized displacement D for adhesive contact between a sphere and a half-space.

results [51]. The non-dimensional load-displacement curves are shown in Fig. 3. It can be seen that the load-displacement curves for very small values of Tabor parameter ($\mu < 0.1$) converge to the prediction of rigid-sphere model:

$$F = \frac{2 - 8(1 - D)^6}{9(1 - D)^8} \tag{3.15}$$

which is referred to as the Bradley curve [45]. For large values of Tabor parameter the load-displacement curves become S-shaped, leading to jumps into and out of contact. The load-displacement curves generated by the present method comprise only the stable solutions that can be observed in experiments. The accuracy and capability of extension to higher values of Tabor's parameter was further confirmed in Ref. [57], where the adhesive contact problem between a spherical indenter and rippled surface was solved and compared with an exact

solution provided by Guduru [58,59].

3.4 Results and Discussion

Since the numerical results will be compared with the approximate elliptical JKR theory, a few of its basic results [50] are summarized here. In the elliptical JKR theory, the contact line where the energy release rate is equal to the work of adhesion is assumed to be an ellipse with semi-major and -minor axis a_c and b_c respectively. The normal load f, separation δ and mean contact radius $c_c \equiv \sqrt{a_c b_c}$ in normalized form (F, Δ, C) are:

$$F = \frac{8}{3\pi}\left[\frac{g(1-g^{1/2})^2}{(\Pi_2 g^2 - \Pi_1)^2}\right] \times \left[\frac{\Pi_1 - \Pi_2 g^{5/2}}{1-g^{1/2}} - \frac{1}{3}(\Pi_2 g^2 + \Pi_1)\right] \quad (3.16)$$

$$\Delta = \left(\frac{2^{7/2}}{9\pi^2}\right)^{2/3}\left[\frac{g(1-g^{1/2})^2}{(\Pi_2 g^2 - \Pi_1)^2}\right]^{2/3} \times \left[2K(e)\frac{\Pi_1 - \Pi_2 g^{5/2}}{1-g^{1/2}} - \Pi_1 B(e) - g^2 \Pi_2 D(e)\right] \quad (3.17)$$

$$C = \left(\frac{4\sqrt{2}}{3\pi}\frac{g^{5/4(1-g^{1/2})}}{\Pi_2 g^2 - \Pi_1}\right)^{2/3} \quad (3.18)$$

where c_r is a reference contact radius defined by $c_r = [9\pi R_e^2 W_{ad}/(4E^*)]^{1/3}$ and g is the axes ratio defined by $g = a_c/b_c$. The axes ratio is related to the eccentricity e of the ellipse by $e^2 = 1 - g^2$. The dimensionless quantities Π_1 and Π_2 are weighting parameters accounting for the effect of adhesion energy:

$$\Pi_1 = \frac{\lambda + \lambda^{-1} - B(e)\Pi_2}{D(e)} \quad (3.19)$$

$$\Pi_2 = \frac{\lambda^2 C(e) + D(e) + C(e)}{\lambda[(D(e) + C(e))(B(e) + g^2 C(e)) - g^2 C(e)^2]} \quad (3.20)$$

where $K(e)$, $C(e)$, $B(e)$, and $D(e)$ are complete elliptic integrals [60] that depend only on the eccentricity e, and λ is the ratio of the principal relative radii of

curvature of the bodies:

$$\lambda = \sqrt{R''/R'} \quad (R'' < R', \lambda < 1) \tag{3.21}$$

The normalized force-displacement curves for different values of R''/R' are plotted in Fig. 4. In a load-controlled experiment, the two surfaces will spontaneously separate once the pull-off force is reached. Following the standard convention in contact mechanics, the absolute value of minimum on the $F(\Delta)$ curve is called as the pull-off or adhesion force, F_c. Fig. 4 shows that the normalized pull-off force F_c monotonically decreases with increasing values of R'/R''.

When $R'/R'' = 1$, the results reduce to the classical JKR theory for circular contact [37,53], which can be written as

$$F = C^3 - \sqrt{2C^3} \quad \Delta = C^2 - \frac{2}{3}\sqrt{2C} \tag{3.22}$$

In the Hertz contact theory, only compressive stresses can exist in the contact area, which gives the following equations [53]:

$$F = C^3 \quad \Delta = C^2 \tag{3.23}$$

For the DMT model, the force is the Hertz force inside the contact area plus the adhesion force outside the contact area, which gives [38,53]

$$F = C^3 - \frac{2}{3} \quad \Delta = C^2 \tag{3.24}$$

For the two problems to be investigated in this paper,

$$R'/R'' = 1 + \beta \;\; Problem1 \quad R'/R'' = \frac{1+\cos\theta}{1-\cos\theta} \;\; Problem2 \tag{3.25}$$

The variation in the ratio of principal relative radii of curvature R'/R'' versus β or θ is plotted for the two problems in Fig. 5, which shows that the ratio is

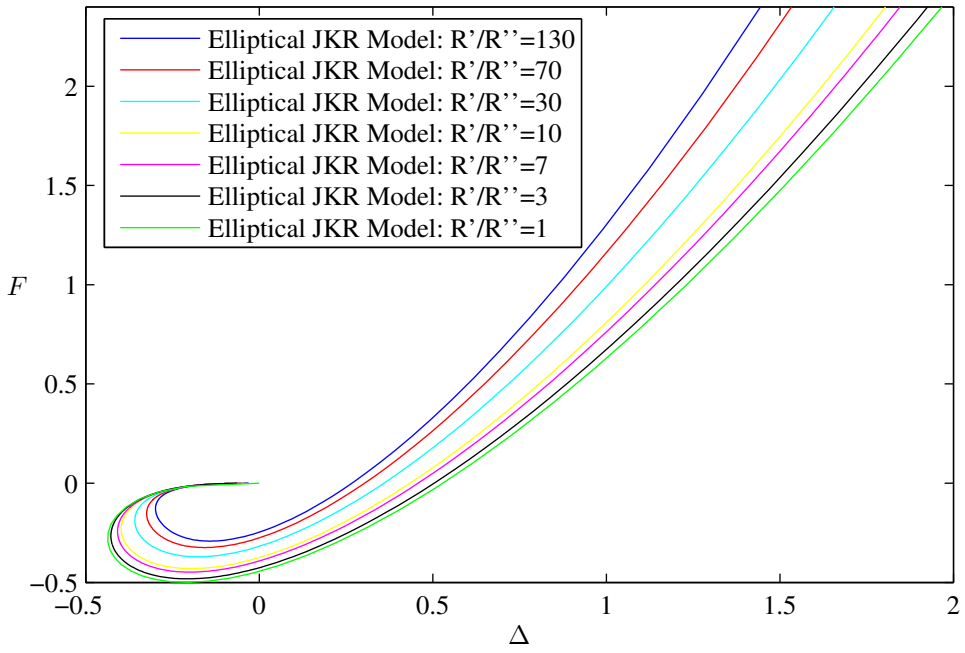

Figure 3.4: Normalized load F versus normalized displacement Δ for different values of R'/R'' based on elliptical JKR theory.

not large in Problem 1 even for very large values of β (large sphere and small cylinder), whereas R'/R'' can be very large in Problem 2 for small skew angles.

Problem 1 is simulated for $\beta = 0.0$, 0.7 and 7.0, and the corresponding values of R'/R'' are 1.0, 1.7 and 8.0, respectively. As shown in Fig. 4, to investigate the region for small values of R'/R'' ($1 < R'/R'' < 10$), a different scaling is needed to distinguish the difference, if any, between the elliptical JKR solution and the numerical results. Thus R_e is replaced by R_s in the dimensionless variables, and F_o and Δ_o are defined. The $F_o - \Delta_o$ curve is plotted for $\mu = 2.2$ in Fig. 6, which indicates that the numerical results agree very well with the elliptical JKR theory. Numerical simulation was also performed for $\mu = 3.0$, but the curve is not shown in this figure, since it is quite similar to that for $\mu = 2.2$.

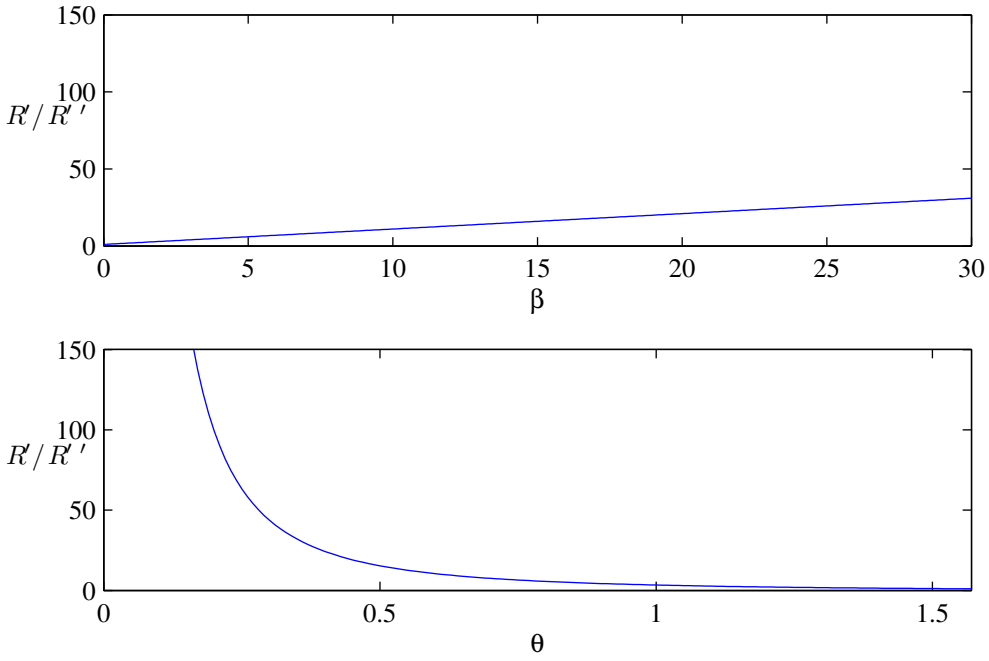

Figure 3.5: The variation in the ratio of principal relative radii of curvature R'/R'' versus $\beta = R_s/R_c$ (Problem 1) or θ (Problem 2).

Problem 2 is simulated for $\theta = \pi/2$, $\pi/3$, $\pi/6$, $\pi/9$ and $\pi/18$, and the corresponding values of R'/R'' are 1.0, 3.0, 13.9, 32.2 and 130.6, respectively. Note that the case of $R'/R'' = 1$ corresponds to classical JKR model for circular contact. Fig. 7 plots the normalized force F versus normalized displacement Δ, which shows that for large values of R'/R'' (small skew angles), the numerical results deviate significantly from the elliptical JKR theory. For example, when $R'/R'' = 32.2$ and 130.6, the numerical results predict much larger values of tensile force for a given indentation depth. In particular, the pull-off forces F_c are nearly independent of the values of R'/R'' (showing an indiscernible decrease with increasing value of R'/R''), which is quite different from the elliptical JKR theory which shows that the pull-off force F_c decreases with decreasing skew angle. One may argue that this discrepancy is due to the fact that elliptical JKR

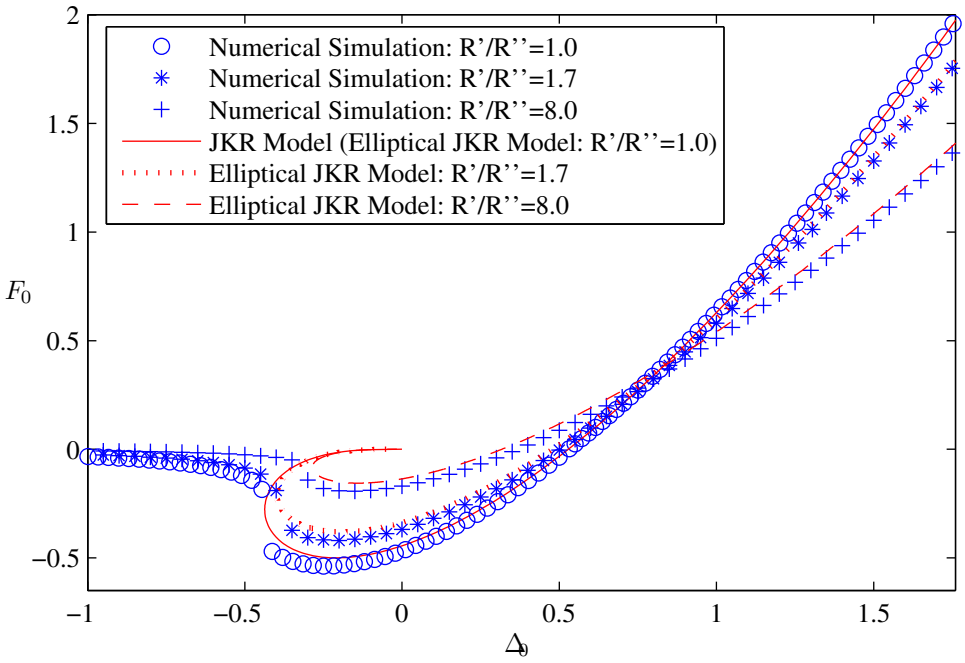

Figure 3.6: Adhesive contact between a sphere and a cylinder: Normalized load F_o versus normalized displacement Δ_o.

theory assumes that $\mu \to \infty$, and therefore it does not explicitly account for surface interaction. However, numerical simulation for the case of $\mu = 3.0$ shows quite similar result to that for $\mu = 2.2$. The percentage of relative deviation is less than 2.23%, much smaller than the deviation from the elliptical JKR solution. This discrepancy can be explained as follows. In the elliptical JKR theory, the crack front (where the energy release rate equals to the work of adhesion) is assumed to be an ellipse. However, the pull-off instability is very sensitive to the shape of the crack front, since a slight change in the shape of crack front can cause the crack to go unstable (see also comment on Fig. 11 and Fig. 12(a)).

Based on the experimental parameters provided by Ref. [52], Fig. 8 plots the pull-off force f_c as a function of the skew angle θ in a dimensional scale

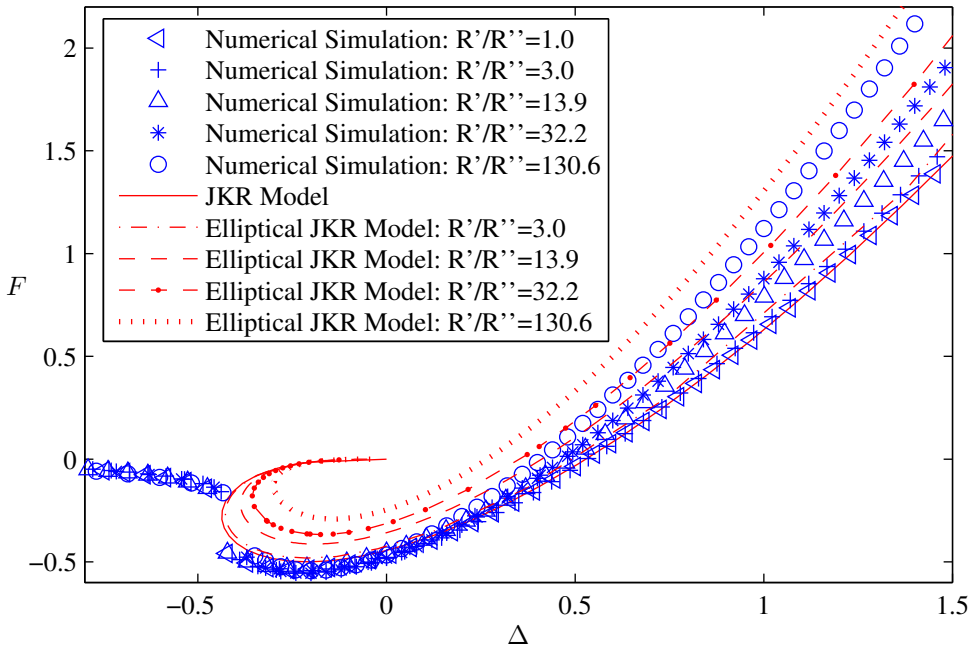

Figure 3.7: Adhesive contact between two identical cylinders placed at a skew angle θ: Normalized load F versus normalized displacement Δ.

superimposed with the prediction of the elliptical JKR model and experimental data. The numerical simulation shows that the elliptical JKR model is fairly accurate for small values of R'/R''. The numerical results start to deviate from the elliptical JKR solution as the skew angle decreases, i.e. the value of R'/R'' increases. Neither of them shows exact fit to the experimental data although our numerical results provide a better fit to the data for $0.2 < \theta < 1$. To compare the shape of the contact area with the elliptical JKR theory, contact needs to be defined. Using Greenwoods definition [44], the location of the peak tensile stress is considered as the contact edge. Denote the location of the peak tensile stresses along x- and y-axis as a_c and b_c, respectively. The mean contact radius c_c obtained using the numerical results will be compared with the elliptical JKR

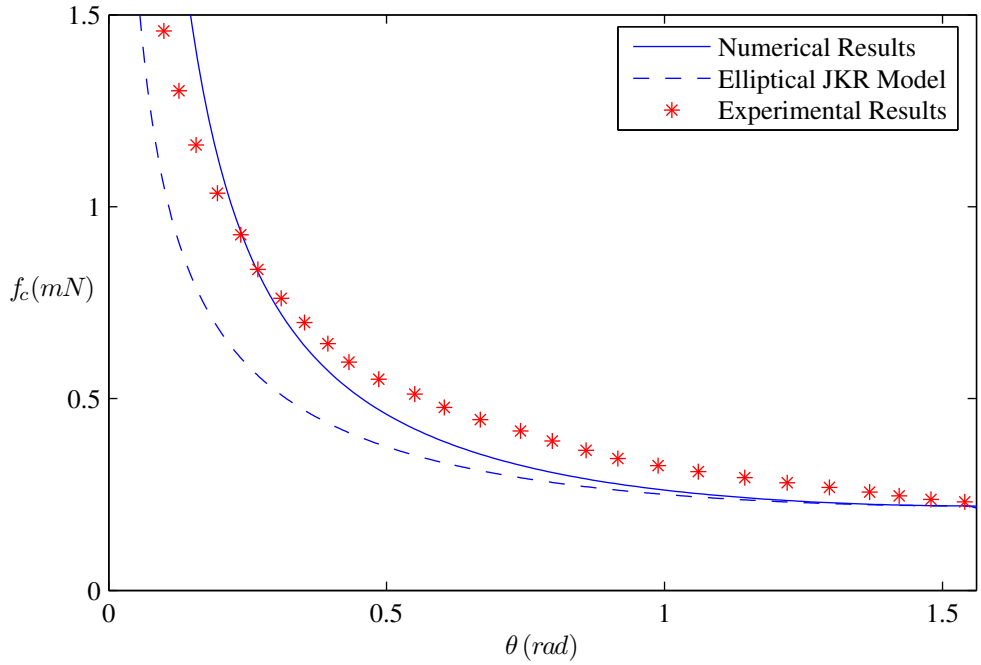

Figure 3.8: Adhesive contact between two identical cylinders placed at a skew angle θ: Numerical results for the pull-off force f_c as a function of θ in a dimensional scale superimposed with the prediction of the elliptical JKR model and experimental results from Ref. [52].

theory. For Problem 1, Fig. 9 plots the normalized force versus normalized mean contact radius for different values of R'/R''. For Problem 2, Fig. 10 plots the normalized force versus normalized mean contact radius. It can be seen that, near the final pull-off, the discrepancy between numerical curves and the elliptical JKR model becomes larger with increasing value of R'/R''.

For Problem 1, Fig. 11 plots a series of normalized pressure distributions P for $\beta = 7.0$ (the corresponding value of R'/R'' is 8.0) and $\mu = 1.0$ at $D = -1.8$, -1.0, 0.0 and 1.0. For Problem 2, Fig. 12(a) plots the normalized pressure distributions for $\theta = \pi/18$ (the corresponding value of R'/R'' is 130.6) and $\mu = 1.0$ at $D = -1.8$, -1.0 and 0.0. When the two bodies are approaching each other

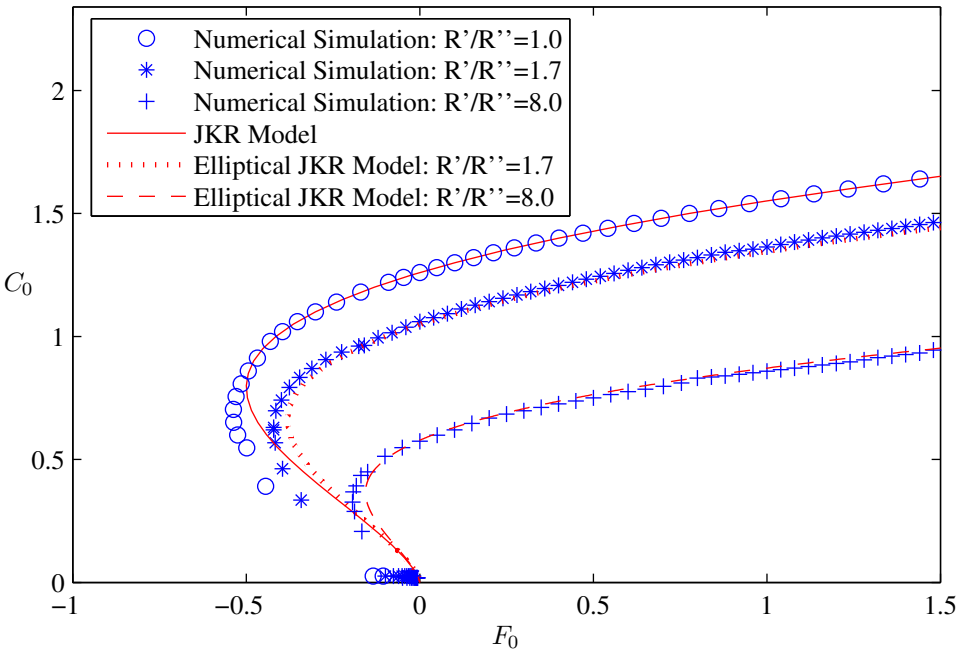

Figure 3.9: Adhesive contact between a sphere and a cylinder: Normalized mean contact radius C_o versus normalized load F_o.

from a noncontact state, the surfaces barely deform with pressure being nearly zero everywhere. As the two bodies approach each other one step further, the surfaces jump to a new equilibrium state suddenly with a nonzero contact area, and the pressure becomes compressive in the central region and tensile at the contact edge.

To check how elliptical the contact lines are, the ellipses based on the location of the peak tensile stresses along x- and y-axis are plotted in magenta lines, as shown in Figs.11 and 12(a). It is found that the contact lines are approximately elliptical. However, a closer examination (by zooming in on the y-axis) reveals that at the tip of the major axis, the real contact shape is always a little blunter as compared to an ellipse, as shown in Fig. 12(b), in which a comparison between

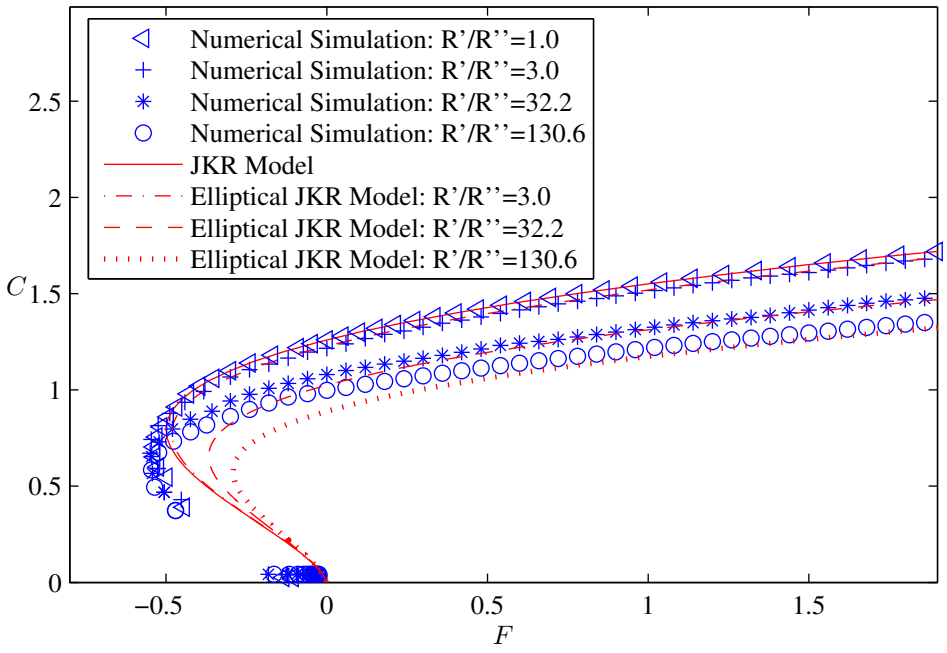

Figure 3.10: Adhesive contact between two identical cylinders placed at a skew angle θ: Normalized mean contact radius C versus normalized load F.

the magenta lines and the real contact lines at $D = -1.2$ is presented for two different skew angles: $\theta = \pi/6$ and $\theta = \pi/18$. This deviation from an ellipse is found to increase as the skew angle is reduced, which is expected since the initial assumption of Hertzian elliptical boundary in the solution of elliptical JKR theory does not satisfy the requirement of that the stress intensity factor to be equal around the periphery, especially for large values of R'/R'' [50]. This deviation is consistent with previous experimental observation, shown in Ref. [52], which shows that the nucleation sites for the detachment starts at the tip of the major axis, resulting in a nonelliptical shape of the contact area.

So far, the simulation has been mostly carried out in the JKR adhesion regime, i.e. for large values of Tabor parameter ($\mu > 1.0$), in which the key

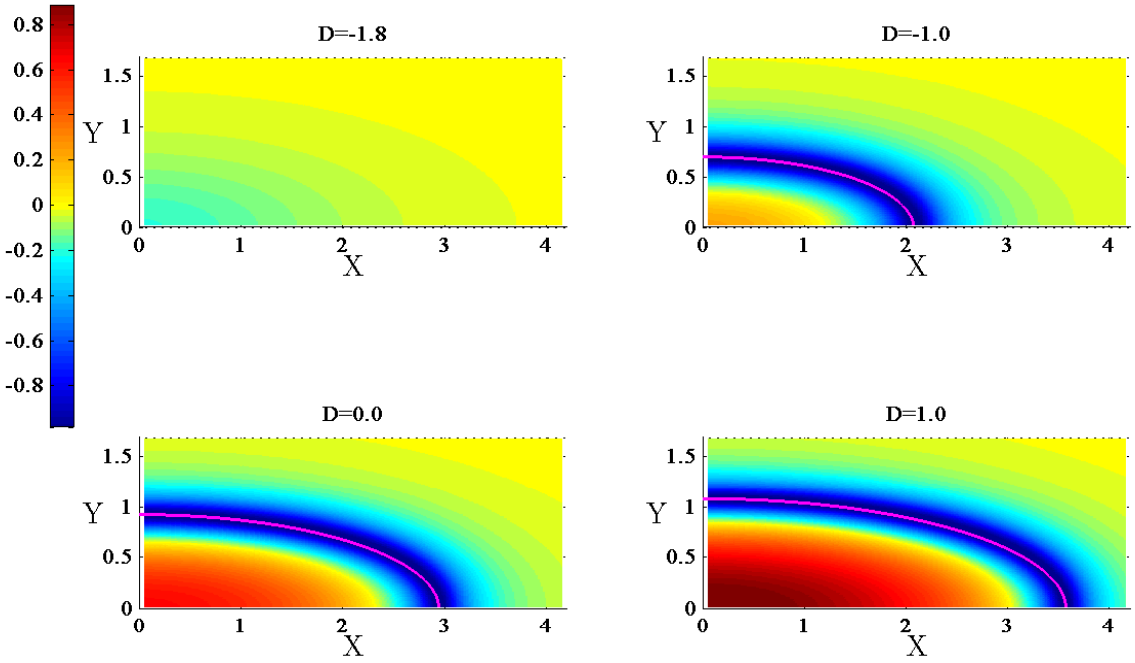

Figure 3.11: Adhesive contact between a sphere and a cylinder: Pressure distribution P for $D = -1.8, -1, 0, 1, \beta = 7.0$ (the corresponding value of R'/R'' is 8.0) and $\mu = 1.0$. Magenta lines show the ellipses based on the location of the peak tensile stresses along x- and y-axis.

assumption is the absence of surface interaction outside the contact area. Attractive forces outside the contact edge become important for stiff materials, small spheres or weak adhesion. In these cases, the contact mechanics is better captured by the DMT model [38, 53], which assumes that molecular forces act only in a ring-shaped zone of noncontact adhesion. To explore the DMT and JKR–DMT transition regimes, Problem 2 is simulated for $\theta = \pi/6$ for different values of Tabor parameter. Fig. 13 plots the normalized force versus normalized displacement. Fig. 14 plots the normalized force versus normalized mean contact radius. The classical JKR model, Hertz contact theory, and DMT model for

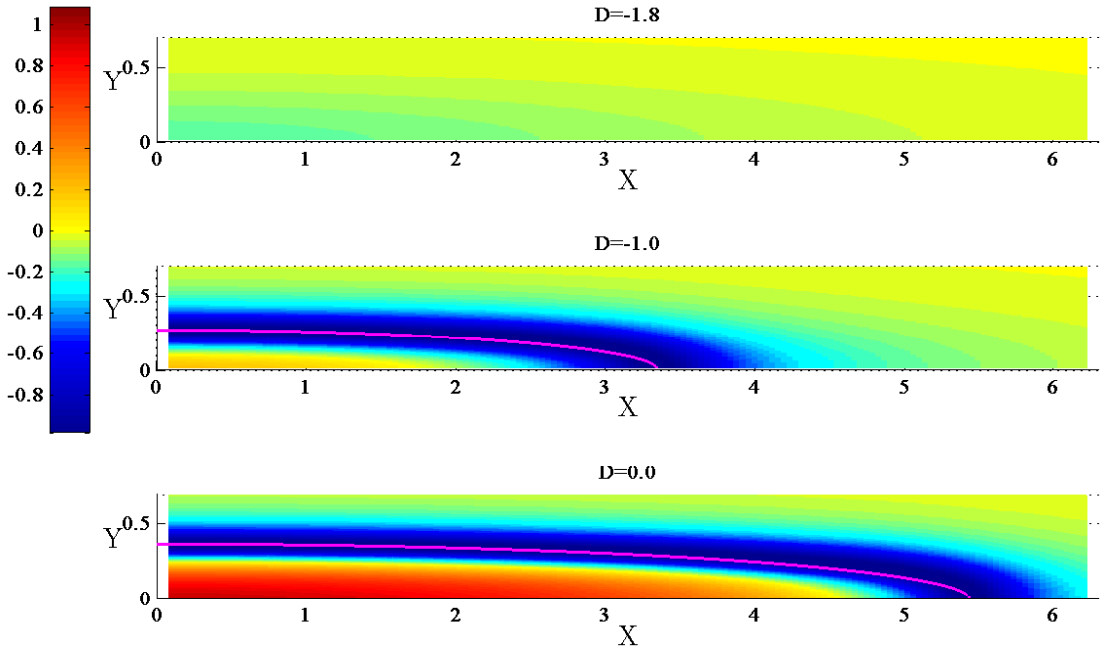
D=-1.8
D=-1.0
D=0.0
Y
X
1
0.8
0.6
0.4
0.2
0
-0.2
-0.4
-0.6
-0.8
0.5
0
1
2
3
4
5
6

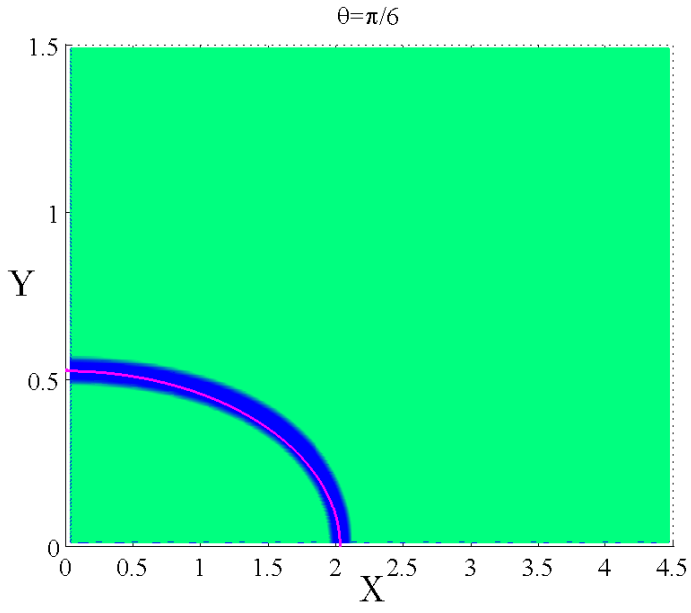
θ=π/6
Y
X
1.5
1
0.5
0
0.5
1
1.5
2
2.5
3
3.5
4
4.5

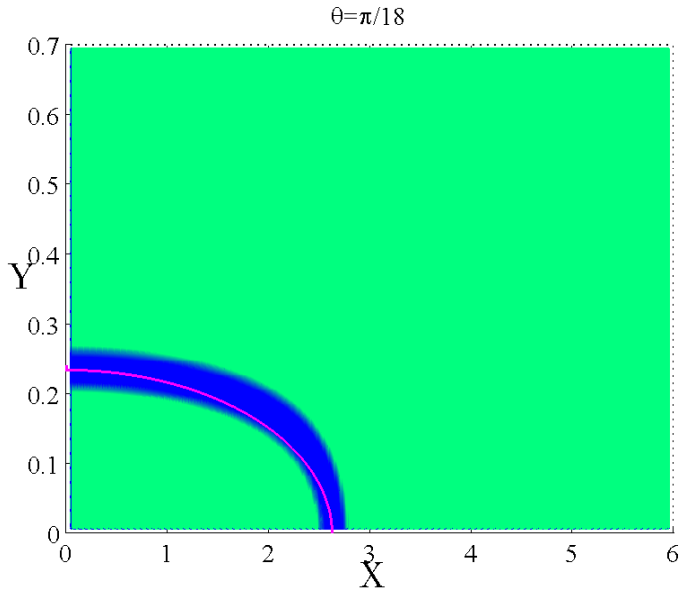

Figure 3.12: (a) Adhesive contact between two identical cylinders placed at a skew angle θ: Pressure distribution P for $D = -1.8, -1, 0$, $\theta = \pi/18$ (the corresponding value of R'/R'' is 130.6) and $\mu = 1.0$. Magenta lines show the ellipses based on the location of the peak tensile stresses along x- and y-axis. (b) Adhesive contact between two identical cylinders placed at a skew angle θ: Pressure distribution P for $D = -1.2$ and $\mu = 1.0$ for two different skew angles $\theta = \pi/6$ and $\theta = \pi/18$. Magenta lines show the ellipses based on the location of the peak tensile stresses along x- and y-axis. The region coloured by deep blue represents the real contact line.

circular contact are superimposed for comparison. It can be seen that with decreasing value of Tabor parameter, the force-displacement curve becomes closer to the prediction by the DMT model.

3.5 Summary

A new numerical technique for analysis of asymmetric adhesive contact problems in rectangular coordinates has been developed. Adhesive interactions are

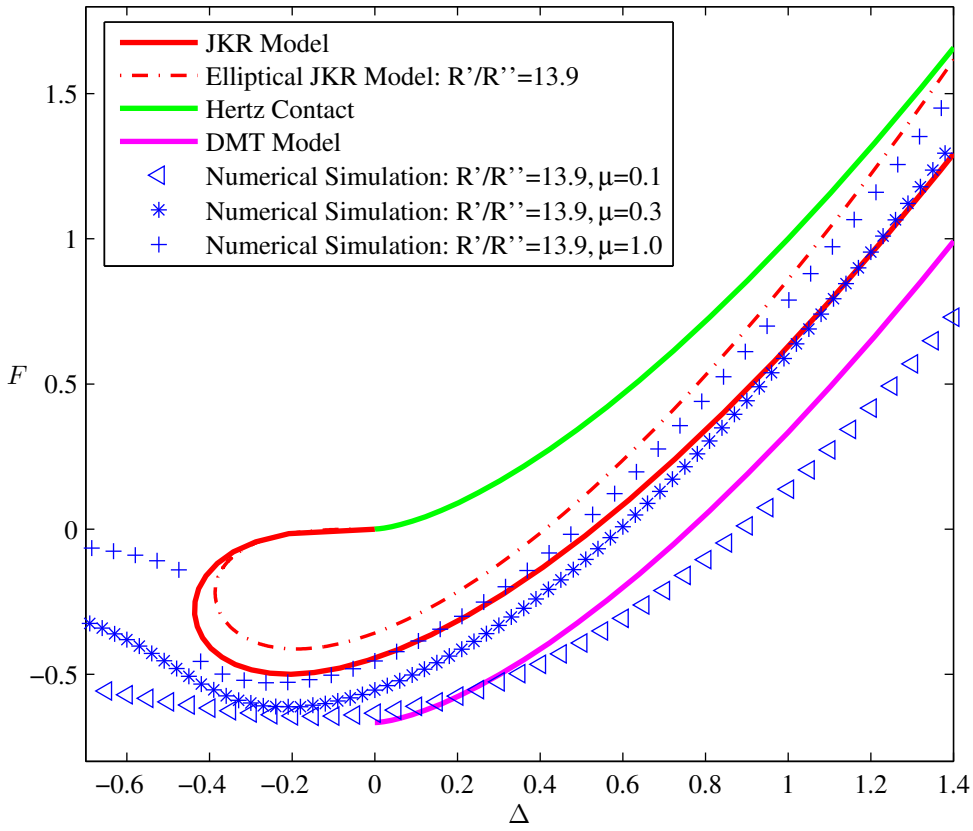

Figure 3.13: Adhesive contact between two identical cylinders placed at a skew angle θ: Normalized load F versus normalized displacement Δ.

represented by an interaction potential and surface deformations are coupled using half-space Green's functions discretized on the surface. The resulting set of nonlinear equations is solved by a relaxation technique. Because it can handle surface topography and spatial variation in adhesive properties, this technique allows more efficient modelling of a number of problems in adhesive contact mechanics that have been difficult to analyse so far.

In this paper, the new numerical method has been applied to two adhesive

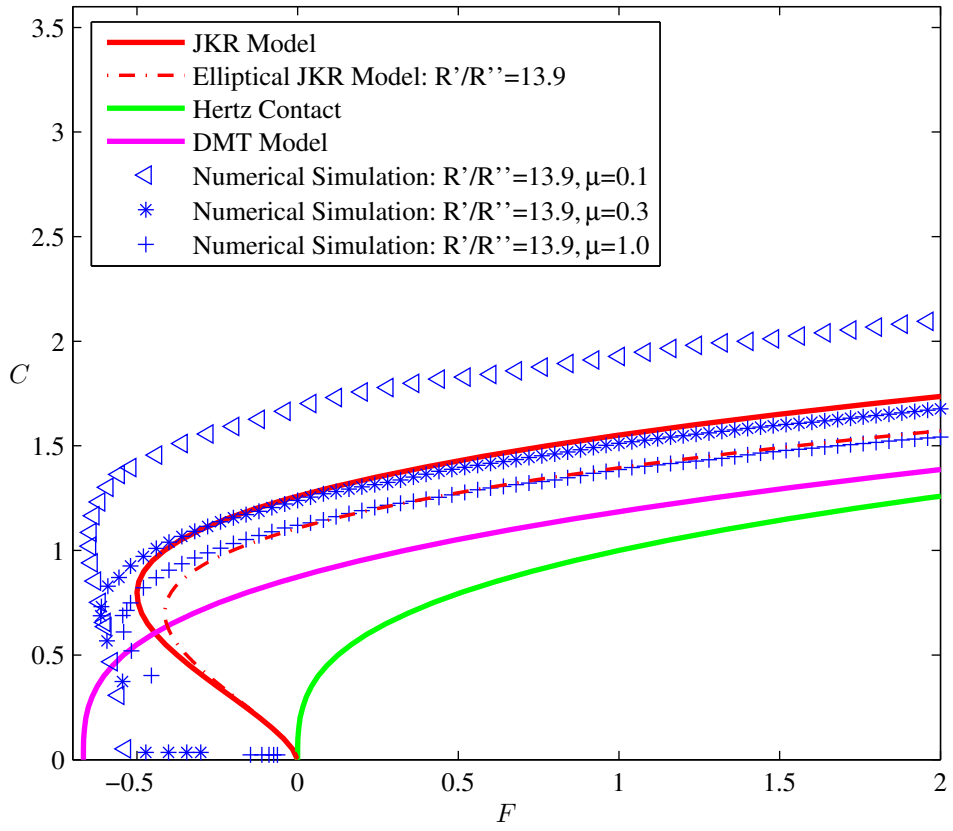

Figure 3.14: Adhesive contact between two identical cylinders placed at a skew angle θ: Normalized mean contact radius C versus normalized load F.

contact problems: the adhesive contact between a sphere and a cylinder; and the adhesive contact between two identical cylinders placed at a skew angle with respect to each other. The results are compared with Johnson and Greenwood's approximate elliptical JKR model [50]. For small values of R'/R'', i.e. the ratio of the principal relative radii of curvature of the bodies, the elliptical JKR model works well, but for large values of R'/R'', the discrepancy between numerical results and the elliptical JKR model becomes large. The pull-off forces show an indiscernible decrease with increasing value of R'/R'' (nearly independent of the

value of R'/R''), which is quite different from the elliptical JKR theory. This deviation is expected since the initial assumption of Hertzian elliptical boundary in the solution of elliptical JKR theory does not satisfy the requirement of the stress intensity factor to be equal around the periphery. The numerical results reveal that at the tip of the major axis, the real contact shape is always a little blunter as compared to an ellipse. This is consistent with previous experimental observation [52], which shows that the nucleation sites for the detachment starts at the tip of the major axis. This numerical technique is much simpler to implement and as accurate as the method introduced by Wu [51]. This technique has also been proven to be very efficient in solving adhesive contact problems between a spherical indenter and rippled surfaces that involve partial contact and large value of Tabor's parameter.

CHAPTER 4

FUTURE WORK

The investigations provided here will lay the goundwork for extending the research on adhesion selectivity to interfaces with numerous other patterns and other parameters, as shown in Fig. 1. What makes this study fascinating is its appeal to the imagination.

4.1 Interfaces in Crystalline Solids

Over the past few decades unprecedented and far-reaching discoveries have been taking place in the material sciences, e.g. in solid state physics, crystallography, metallurgy and nanotechnology, which have led to deeper understanding of how nature works, e.g., of how atoms combine to build the world. In seeking inroads into microstructure design to obtain desired adhesion properties, concepts are borrowed back and forth between theoretical mechanics and material science. I here first briefly review some basic concepts and results on the subject of interfaces in heterophase and homophase crystalline solids [61].

4.1.1 Three Types of Interfaces: Coherent, Semi-Coherent, and Incoherent

Basically the theory which we use to describe interfacial dislocation structures is that of Frank and van der Merwe [62–69] who formulated it in 1949, well before experimental observations of interfacial dislocations. At that time, dislocation

theory was still in its early stage. Even though the Frank–van der Merwe theory was developed as a description of thin film epitaxy, it has also been successfully applied to similar boundaries generated during phase transformations. Christian [70] has detailed the formal theory of interfacial boundaries. He has distinguished three types of interface which he described as incoherent, semicoherent and coherent. These three types are schematically represented in Fig. 2.

A "coherent" interface arises when two crystals match perfectly at the interface plane so that the two lattices are continuous across the interface, as shown in Fig. 2a. This can be achieved if, disregarding chemical species, the interfacial plane has the same atomic configuration in both phases, and this requires the two crystals to be oriented relative to each other in a special way. Coherent interfacial energy ranges from 0 to 200 mJ/m^2.

When the interface plane has a very different atomic configuration in the two adjacent phases, there is no possibility of good matching across the interface. The pattern of atoms may either be very different in the two phases or, if it is similar, the interatomic distances may differ by more than 25%. In both cases the interface is defined as "incoherent", as shown in Fig. 2b. Incoherent interfacial energy ranges from 500 to 1000 mJ/m^2, where the structural contribution is really large. Very little is known about the detailed atomic structure of incoherent interfaces.

Moire Lines

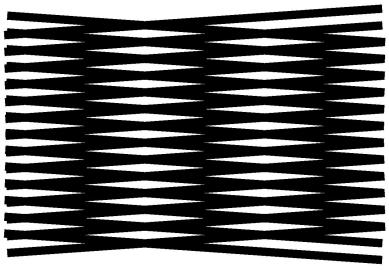

(a) Two identical sets of lines overlaid slightly askew generate a single array of parallel screw dislocations.

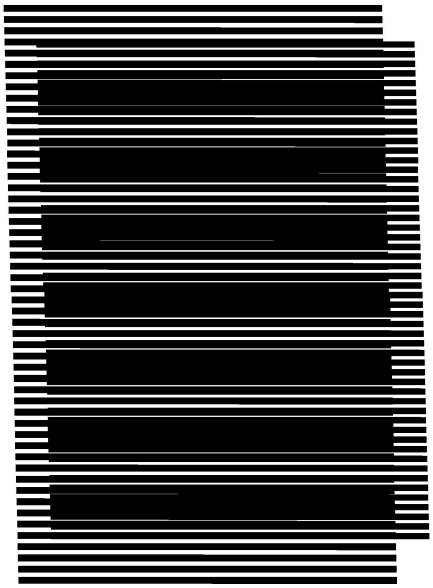

(b) Two sets of lines with different spacings generate a single array of parallel edge dislocations.

Moire Grids

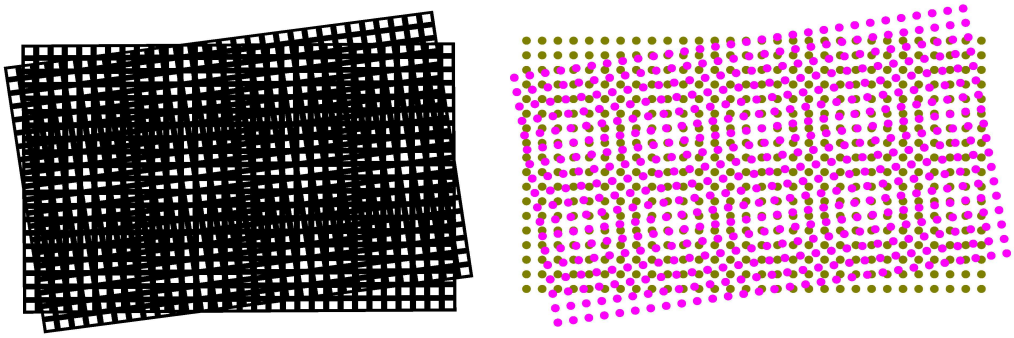

(c) Two identical grids overlaid slightly askew generate a network of two sets of screw dislocations.

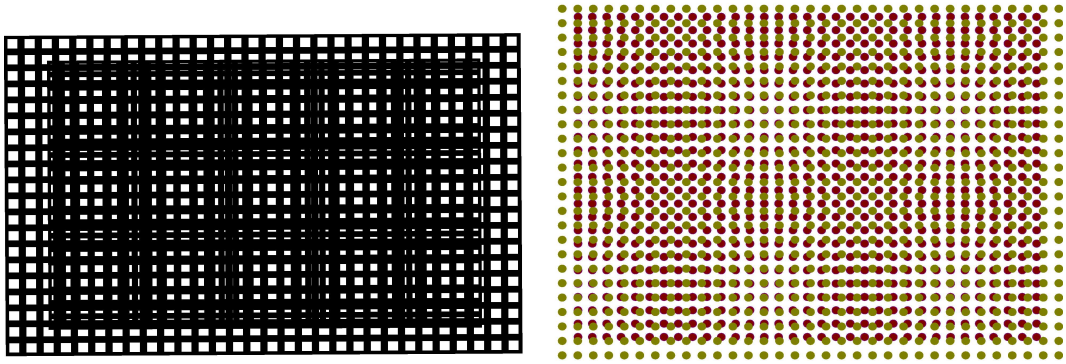

(d) Two grids of different sizes generate a network of two sets of edge dislocations.

Moire Pattern with Honeycomb Lattices

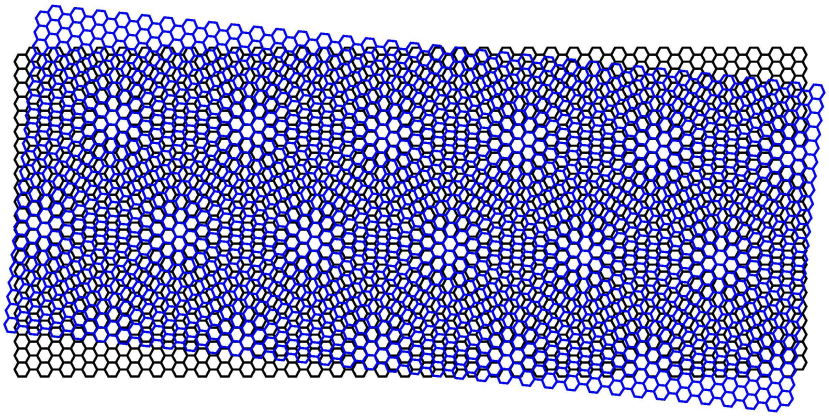

(e) Two identical patterns with honeycomb lattices overlaid slightly askew generate a network of three sets of dislocations.

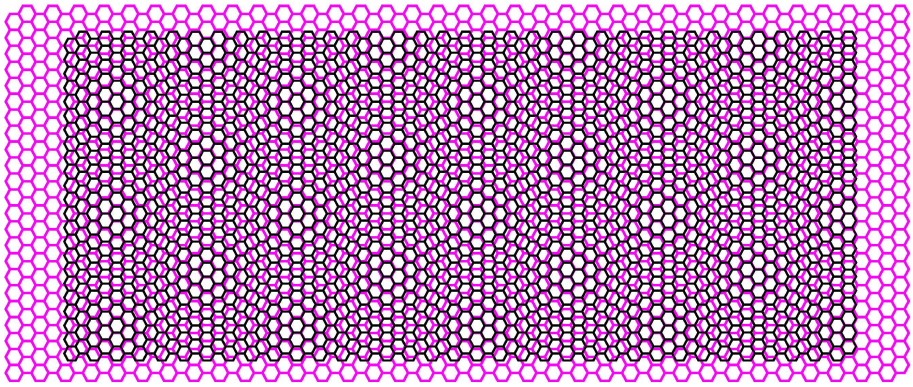

(f) Two patterns with honeycomb lattices of different sizes generate a network of three sets of dislocations.

(g) Moire Pattern with Triangular Lattices

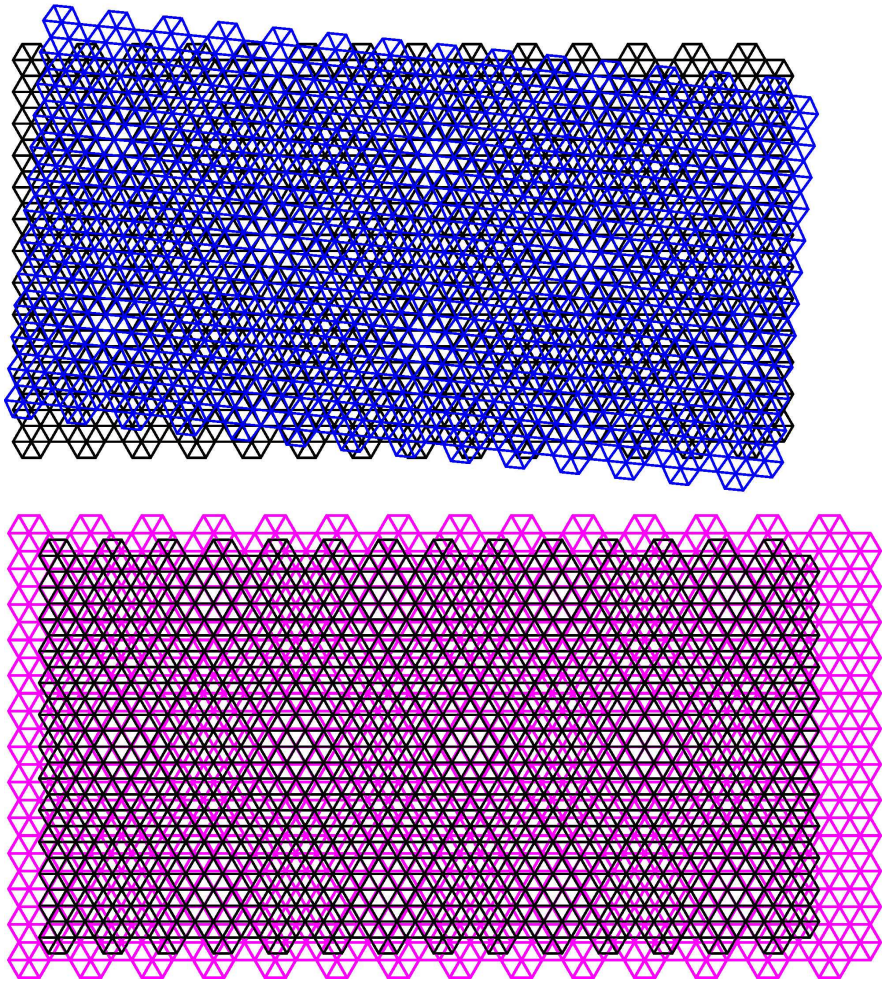

(h) Moire Circles and Spirals

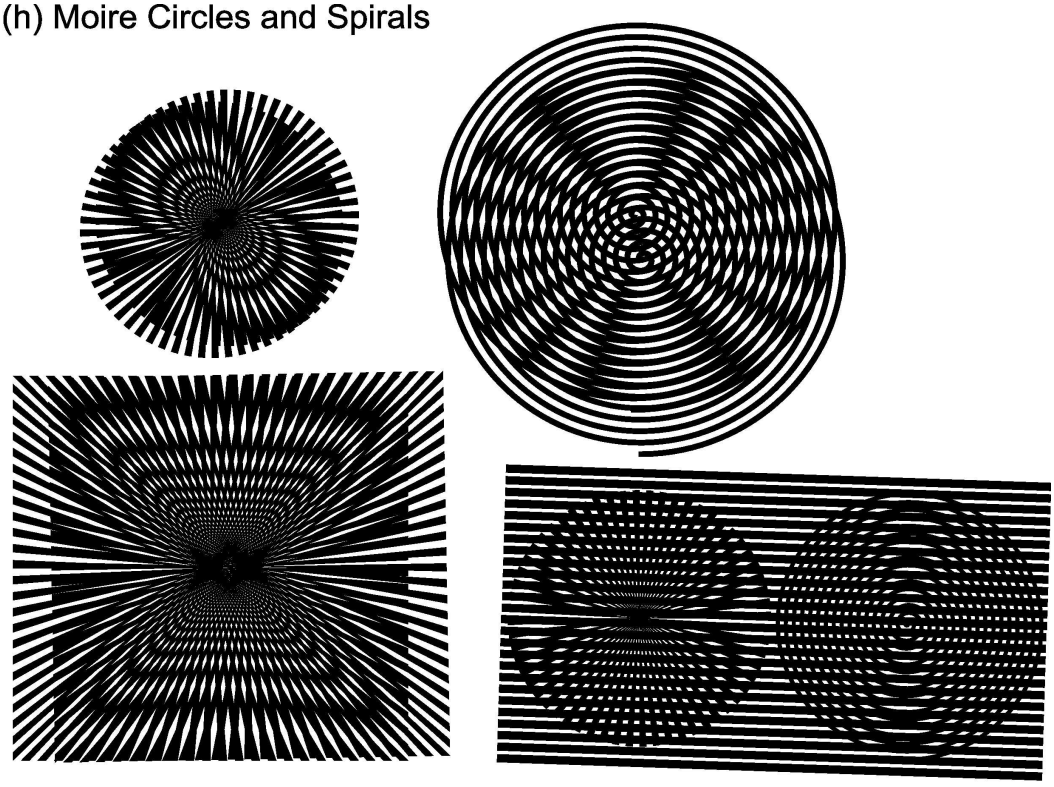

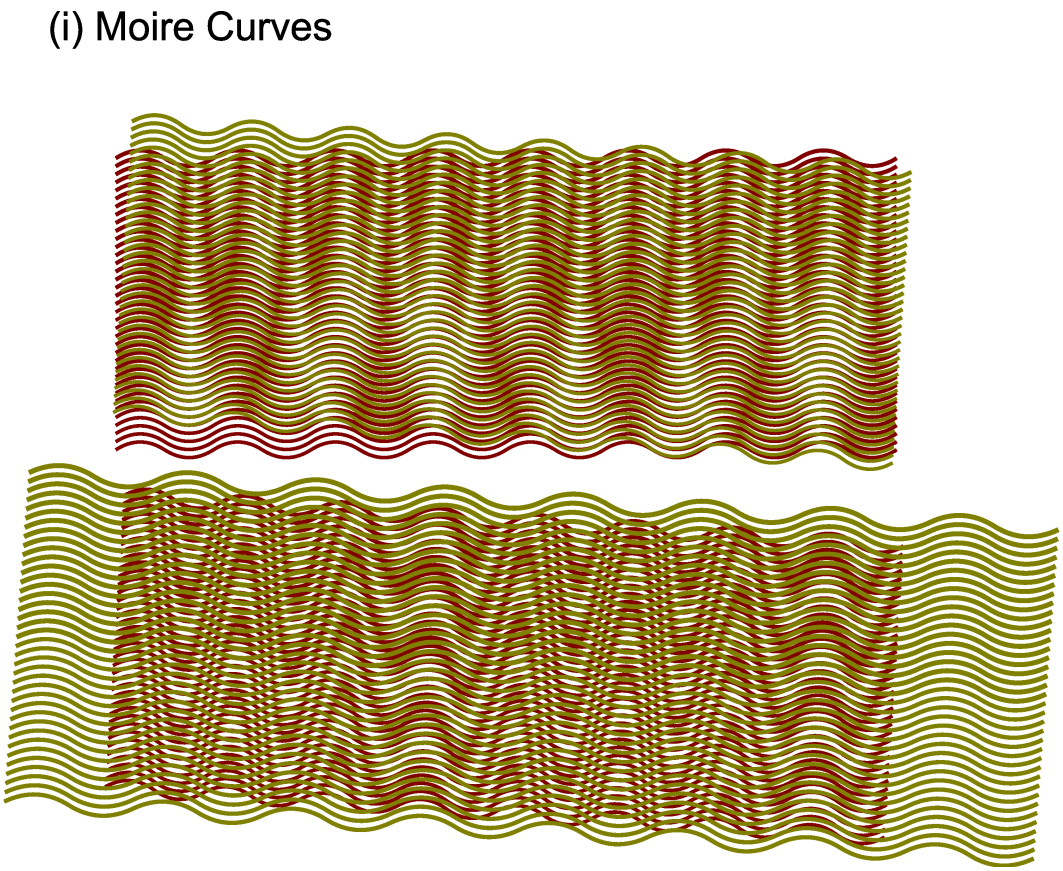

Figure 4.1: Examples of Moire patterns: (a) Moire lines (rotational misalignment), (b) Moire lines (size mismatch), (c) Moire grids (rotational misalignment), (d) Moire grids (size mismatch), (e) Moire pattern with honeycomb lattice structure (rotational misalignment), (f) Moire pattern with honeycomb lattice structure (size mismatch), (g) Moire pattern with triangular lattice structure, (h) Moire circles and spirals, and (i) Moire curves. In the whitish (bright) areas, there is a high degree of coincidence of lattice points, whereas in the black areas the misfit is largest.

When the strains associated with a coherent interface raise the total energy of the system, and for sufficiently large atomic misfit, or interfacial area, it becomes energetically more favorable to replace the coherent interface with an interface in which the disregistry is periodically taken up by misfit dislocations. If the dislocations are sufficiently far apart so that patches of coherency exist between them, the interface called "semicoherent", as shown in Fig. 2c, while if their density is so high that no coherent patches remain, the interface is simply "incoherent". Semicoherent interfacial energy ranges from 200 to 500 mJ/m^2.

Heterophase interfaces are typically coherent only if one of the neighboring crystals is strained to match the crystallography of the other. Since coherent interfaces usually have lower energies than incoherent ones, it is sometimes energetically favorable for such straining to take place when the strained layer is sufficiently thin. As the thickness of the strained layer increases, however, its elastic energy exceeds the difference in energy between a coherent and an incoherent interface, giving rise to a thermodynamic driving force for a coherent-to-incoherent interface structure transition [71–75].

Semicoherent interfaces may be observed using transmission electron microscopy (TEM) in interfaces between crystals whose misfit is small [75–77] and may also be seen in grain boundaries with sufficiently low deviations from coherency [78, 79]. The simple case of a misfit in one dimension, as shown in Fig. 2c, is less likely to be encountered in real materials than cases of a two-dimensional misfit, where more than one set of dislocations is required to take up the mismatch. Square networks of edge dislocations have been seen at the faces of plates of UC_2 precipitated within a matrix of UC [80]. The structure of UC is the same as that of $NaCl$; the square pattern of U atoms in the {100} planes

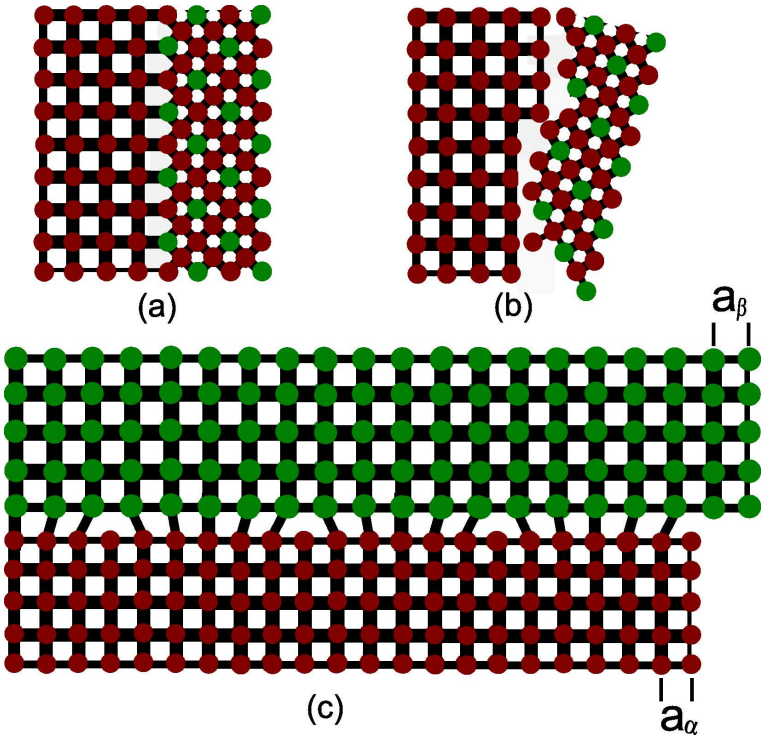

Figure 4.2: Three types of interfaces: (a) coherent, (b) incoherent, and (c) semi-coherent. a_α and a_β are the unstressed interplanar spacings of the matching planes in the $\alpha-$ and $\beta-$ phase, respectively. The number of extra planes to be accommodated in the lower crystal of (c), in unit distance, is $m = |a_\alpha^{-1} - a_\beta^{-1}|$. The dislocation spacing $d = m^{-1} = a_\alpha a_\beta / |a_\alpha - a_\beta|$.

almost matches that of the U atoms in the (001) of UC_2, which has a b.c.t. structure. A square net of edge dislocations takes up the small mismatch at the faces of the (001) plates of UC_2 which precipitate on the cube planes of UC. A comprehensive review of experimental results on interfacial dislocation structures has been provided by Shiflet [81].

For a general interface, say between α and β phase, when β particle precipitates from α phase, a new interface forms. For a spherical particle of radius r, the total surface energy is the sum of the two sources: surface energy contributed by chemical bonding at interface, $\gamma_{ch} = 4\pi r^2 \gamma_{\alpha\beta}$, and the strain energy,

$\gamma_{st} = \frac{4}{3}\pi r^3 c\epsilon^2$, where c is elastic constant, and ϵ is defined as "misfit", i.e., the relative strain due to misfit of lattice. Denote a_α and a_β as the unstressed interplanar spacings of the matching planes in the $\alpha-$ and $\beta-$ phase, respectively. We have $\epsilon \approx |a_\alpha - a_\beta|/a_\alpha \approx |a_\alpha - a_\beta|/a_\beta$.

For example, for the case shown in Fig. 2c, if $a_\alpha = 1.0$Å and $a_\beta = 1.2$Å, then $\epsilon = 20\%$ (i.e. every 5 continuous planes in the β phase will take a dislocation to accommodate the misfit of the two lattice). However, if $a_\alpha = 1.0$Å and $a_\beta = 1.01$Å, i.e., no significant difference between the two phase lattice, then $\epsilon = 1\%$ (i.e. the dislocation density decreases to every 100 planes in the β phase, approaching to the case of coherent interface); on the other hand, if the two phases differ dramatically in lattice, say $a_\alpha = 1.0$Å and $a_\beta = 1.5$Å, then $\epsilon = 50\%$, (i.e., now every 2 continuous planes in the β phase will take a dislocation, very worse for the two phases to match or fit, thus falling to the category of incoherent interface.) The interface with intermediate $\epsilon < 25\%$ is usually called semicoherent interface.

The interfacial energy of a semicoherent interface can be approximately considered as the sum of the chemical contribution and strain (misfit) contribution: $\gamma_{semicoherent} = \gamma_{st} + \gamma_{ch}$. As ϵ increases, the dislocation spacing diminishes. For small values of ϵ, the structural contribution to the interfacial energy is roughly proportional to the density of the dislocations in the interface: $\gamma_{st} \propto \epsilon$. The energy of the boundary can be calculated, and its dependence on the misfit is very similar to the dependence of the energy of a low angle grain boundary on its angle of tilt or twist [67,82,83]. However, γ_{st} increases less rapidly as ϵ becomes larger and it levels out when $\epsilon \to 0.25$. The reason for such behavior is that as the misfit dislocation spacing decreases, the associated strain field increasingly overlap and annul each other. When $\epsilon > 0.25$, i.e., one dislocation for every four

interplanar spacings, the regions of poor fit around the dislocation cores overlap and the interface cannot be considered as coherent, now turns to be incoherent.

4.1.2 Frank–Bilby Equation

The number and character of misfit dislocations in an equilibrium interface is related to the strain needed to impose coherency, and thus it is possible to predict the exact misfit dislocation configuration at semicoherent interfaces. For this purpose, Frank–Bilby equation [61, 70, 84, 85] is widely used for crystal structures that can be related to each other through uniform deformations, but requires generalization for ones that are not (e.g. transformations between b.c.c. and h.c.p. structures involve both a deformation and a sublattice shuffle).

For the derivation of Frank–Bilby equation, assume that two lattices α and β intersect at an interface with a unit normal vector $\vec{n}$ and these two lattices are generated from the same reference lattice by the transformation matrices S_α and S_β, respectively. Using the standard finish-start/right-handed (FS/RH) convention in an orthogonal coordinate system, the Frank-Bilby equation can be written as $\vec{b}_c = (S_\alpha^{-1} - S_\beta^{-1})\vec{x}$, where $\vec{b}_c$ is the Burgers vector to annihilate the misfit strain across an arbitrary vector $\vec{x}$ in the interface $\vec{n}$. If the lattice α is selected as the reference lattice, the Frank-Bilby equation becomes: $\vec{b}_c = (I - S^{-1})\vec{x} = T\vec{x}$, where I is a unit matrix, and S and T are given as $S = S_\beta S_\alpha^{-1}$ and $T = I - S^{-1}$, respectively.

The Frank-Bilby equation is generally accepted for characterizing misfit in interfaces, but it contains vectors that are continuous variables so that it has to be quantized to account for discrete misfit dislocation arrays in interfaces. It

says nothing concerning network reconstructions or dissociation of dislocations into partials, both of which are observed in TEM [79]. To derive a misfit dislocation configuration from it, additional assumptions must be made. Knowles's approach requires a specific set of misfit dislocation Burgers vectors to be assumed [86]. Bollmann's O-lattice theory is also often used to calculate periodic dislocation structure of interfaces, and it claims that the misfit dislocation Burgers vectors cannot be uniquely specified [87, 88]. Further difficulties arise in the proper selection of coherent reference state, which may result in unphysical predictions [61]. The underlying reason for these ambiguities is that the Frank-Bilby equation provides a purely geometrical constraint on misfit dislocation networks that may be met in numerous ways. The true solution must also minimize the interface energy.

4.2 Unresolved Problems and Future Work

Those concepts and results from material science are closely connected to our research, especially the results provided in the first chapter.

> Small is similar to great,
> Though they different appear.
> —-Goethe (1749–1832)

For two crystals growing together, they prefer order to disorder, and the perfect match region will extend by relaxation and the dislocation region will shrink. In an isomorphic manner, when the pressing force is applied to two misaligned PDMS strips, the featureless region will extend, and correspondingly

the dislocation region will shrink until it reaches a state of equilibrium. The linear elastic model to calculate the strain energy stored in the dislocation configuration would be identical for the two problems except that for crystalline solids we need to use the full, anisotropic elastic constant tensors, whereas PDMS is isotropic.

Our experiments show that when misalignment angle is very small, only a few dislocation regions are found, and they show no regular pattern. As we gradually increase the misalignment angle, it becomes energetically more favorable to replace the "coherent" interface with an interface in which the misfit is periodically taken up by screw dislocations, i.e., the initially almost random dislocation distribution resolves into a periodic pattern. In these "semicoherent" interfaces, the relationship between period of dislocation pattern and misalignment angle matches closely with Moire analysis. When the misalignment angle is further increased, the featureless region can be observed at first, but the defect structure is not stable, and thus the featureless regions in between start to shrink upon release of the pressing force, and as a result, the interface becomes simply "incoherent". We may apply techniques borrowed from the analysis of crystalline solids, such as the Frank–Bilby equation, to study our experimental results at tens-of-micron scale.

Our study so far has been focusing on the single array of screw dislocations. Edge dislocation array needs further examination with PDMS samples patterned with parallel microchannel structures of slightly different spacings, as shown in Fig. 2c. Additional suggestions for future work is to investigate misfit dislocation networks with two or three arrays of edge/screw dislocations, which may involve more intricate pattern designs and fabrication techniques,

as shown in Fig.1. A more careful examination on the effect of channel depth is also of great interest. Gradually decreasing the value of channel depth may result in the movement of dislocations, or a complete removal of dislocations. It can also be possible to apply photoelastic technique to visualize the stress field around dislocations and crack fronts, since the PDMS samples are transparent.

APPENDIX A

APPENDIX OF CHAPTER ONE

A.1 Relationship between Local Geometric Properties of Dislocation Structure and Interfacial Adhesion Strength

A.1.1 Strain Energy Stored in Standard Core

Both simplicity and singularity of the continuum theory of dislocations result from an unphysical yet mathematically convenient description of the dislocation core where the distribution of Burgers vector is described by a delta function. Since the 1960s, several schemes have been developed to remove the singularities [27]. A well-known approach is proposed by Lothe [28], who removes (or weakens) the singularity by spreading the dislocation core uniformly over a fixed finite width on the glide plane, which is commonly referred to as the standard reference core. It is worthwhile to notice that this simple and straightforward mathematical model actually gives a realistic description of the core structures observed in our experiments, as shown in Fig. A1.

A strip of width dx within the interval $[-b/2, b/2]$ contributes with dc, $dc = cdx/b$, to the Burgers vector, and thus the relative displacement over the discontinuity surface is as follows:

$$\Delta u_z = 0, x < -\frac{1}{2}b \tag{A.1}$$

$$\Delta u_z = c(\frac{1}{2} + \frac{x}{b}), -\frac{1}{2} < b < \frac{1}{2} \tag{A.2}$$

$$\Delta u_z = c, x > \frac{1}{2}b \tag{A.3}$$

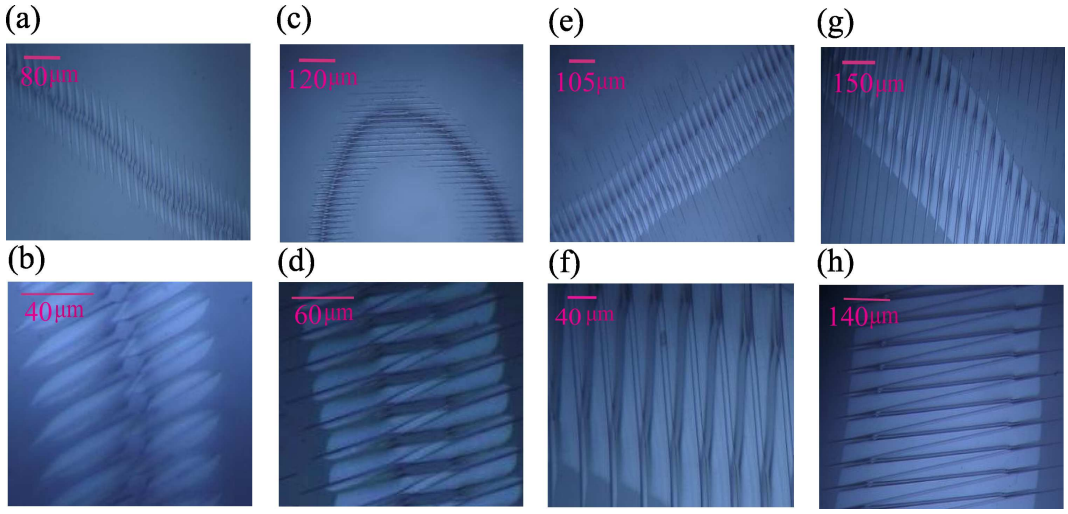

Figure A.1: Optical micrographs of dislocation regions in complementary surfaces. All the samples shown above have the same channel depth and width, $d = w = 10\ \mu$m, and the misalignment angle $\theta < 2^o$. The interchannel spacing c is varied: (a), (b) and (c): 20 μm (d): 30 μm (e): 35 μm (f): 40 μm (g): 65 μm (h): 70 μm. Clear, featureless regions are those where pillars have been inserted fully into channels. These striations are dislocation regions where pillars fail to fully insert into channels.

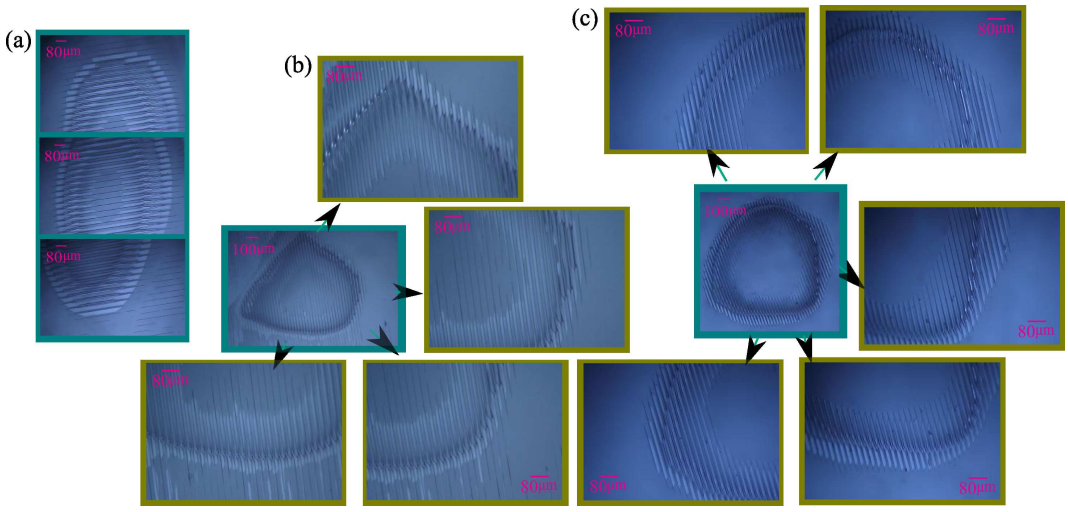

Figure A.2: Some intricate dislocation patterns, such as closed loops, are observed in the samples with small interchannel spacing ($c <$ 60 μm). The samples have $d = w = 10\ \mu$m, $c = 40\ \mu$m in (a), and $c = 20\ \mu$m in (b) and (c).

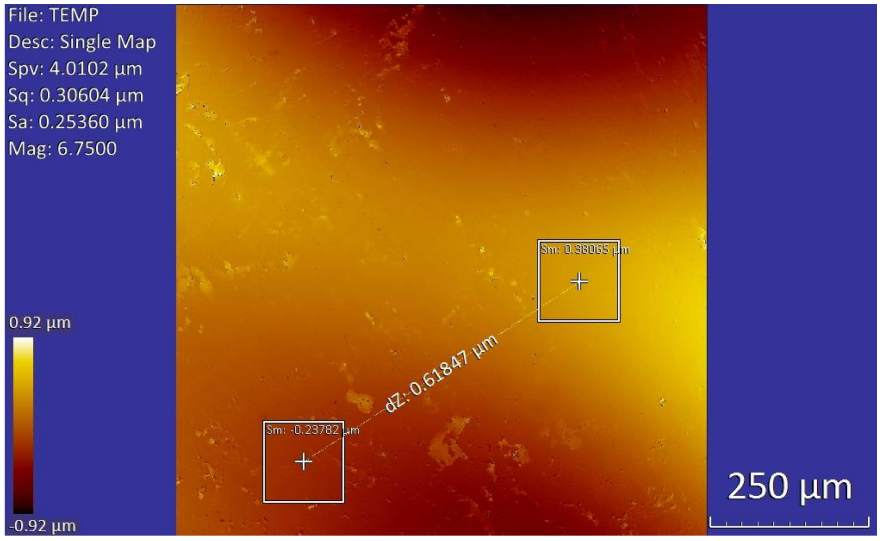

Surface metrology with nanometer-level precision.

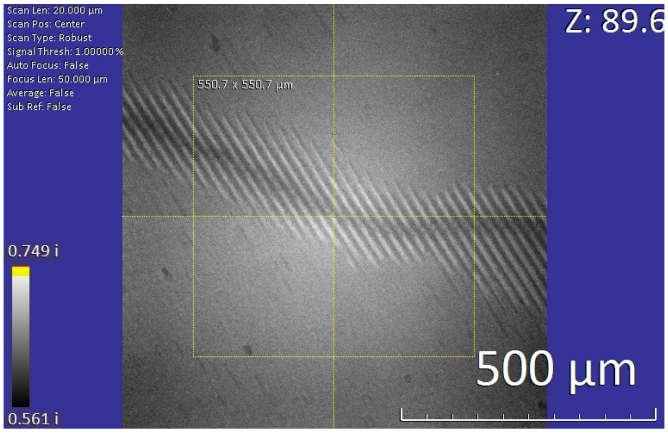

Optical micrograph of the dislocation structure at the interface.

Figure A.3: A typical surface morphology for a pair of complementary surfaces, showing that the region on the surface right above the dislocation region at the interface is about 0.618 μm higher than that above the featureless region. Each piece of sample is 610 μm thick. The dimensions of the microstructure: $d = w = 10$ μm, and $c = 20$ μm, and the misalignment angle: $\theta < 2^o$.

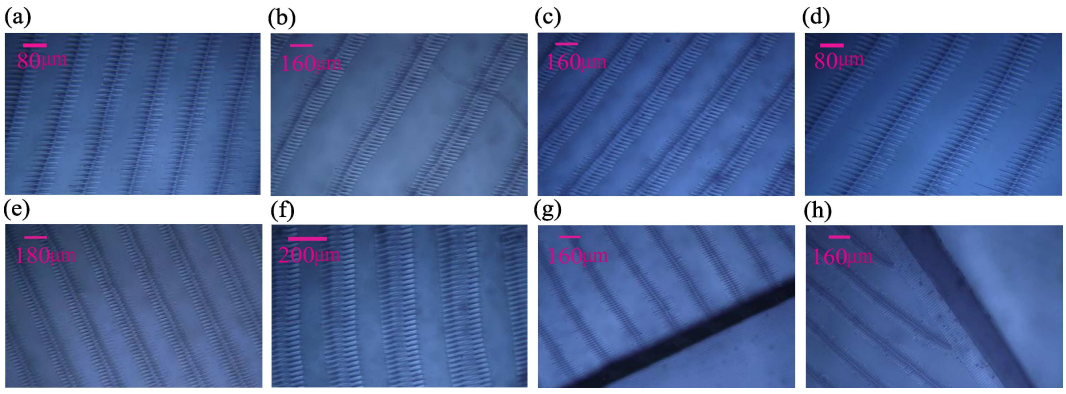

Figure A.4: Optical micrographs of the periodic patterns of dislocation regions in misaligned complementary surfaces. All the samples shown above have the same channel depth and width, $d = w = 10\ \mu$m. The interchannel spacing c is varied: (a), (d), (g) and (h) 20 μm; (b), (c) and (e) 30 μm; (f) 40 μm. The misalignment angle θ is varied: (a) 8.37^o; (b) 3.59^o; (c) 4.59^o; (d) 5.37^o; (e) 5.09^o; (f) 4.97^o; (g) and (h) 4.09^o.

For an infinite straight screw dislocation stretching out along z-axis, the singular expression for σ_{yz} in the x-direction is simply $\frac{\mu c}{2\pi x}$. When the Burgers vector is spread uniformly over the interval $x \in [-b/2, b/2]]$, the stress field in the x-direction becomes

$$\sigma_{yz} = \frac{\mu c}{2\pi b} \int_{-b/2}^{b/2} \frac{1}{x - x'} dx' \tag{A.4}$$

which gives

$$\sigma_{yz} = \frac{\mu c}{2\pi b} \log(\frac{x + b/2}{x - b/2}) \quad x > b/2 \tag{A.5}$$

$$\sigma_{yz} = \frac{\mu c}{2\pi b} \log(\frac{x + b/2}{b/2 - x}) \quad -b/2 < x < b/2 \tag{A.6}$$

This stress field is logarithmically divergent, but integrable, so that the elastic energy in the core will be bounded. By making use of Eqns. (A1)–(A6), the work per unit length done on the discontinuity surface $y = 0$, $-\frac{1}{2}b < x < R_o$, $(R_o >> b)$ can be derived as follows:

$$\frac{1}{2} \int_{-b/2}^{R_o} \sigma_{yz} \Delta u_z dx = \frac{\mu c^2}{4\pi} \log \frac{R_o e^{3/2}}{b} \tag{A.7}$$

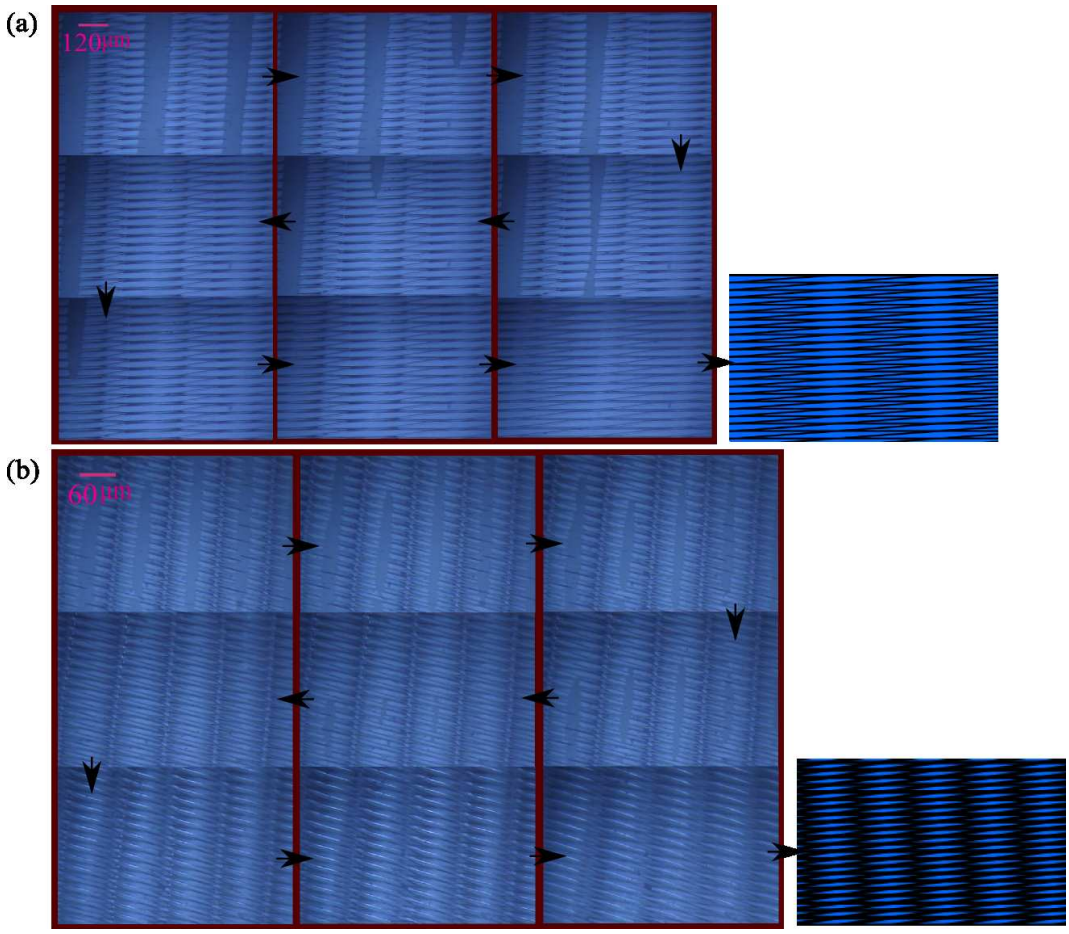

Figure A.5: Images from a video representing two typical sequences leading to the detachment of two PDMS strips. The first frame was grabbed 20 seconds after release of the pressing force. It shows the shrinkage of the featureless region between the close-packed periodic dislocation regions. The last frame taken 10 minutes after release of the pressing force depicts the almost detached state of the two sheets, which shows that the disappearance of the featureless region on both sides of the dislocation region allows the core region to relax. Both samples shown above have the same channel depth and width, $d = w = 10\ \mu$m. The interchannel spacing c: (a) 40 μm (b) 20 μm. The misalignment angle θ: (a) 6.30^o (b) 9.94^o. A completely decoupled state of the two sheets may be visualized using the Moire pattern (drawn to scale) on the right.

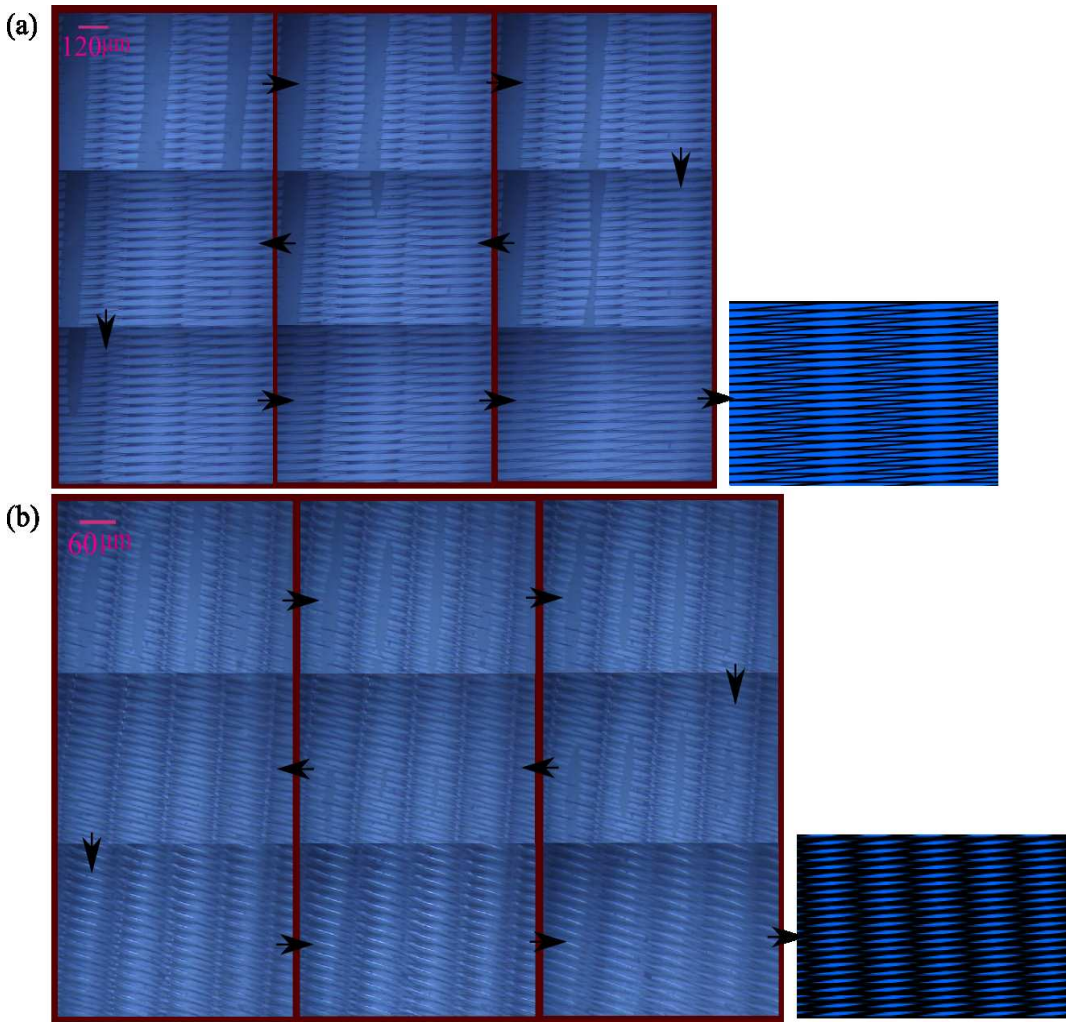

Figure A.6: The influence of pre-existing dislocations on the shape of the debonded region can be substantial. The video images in (a)-(d) and the last frames in (e)-(g) show the final equilibrium shapes of the debonded regions. The samples shown above have $d = w = 10$ μm and $\theta < 2^o$. The interchannel spacing $c = 30$ μm in (a), (b), (f) and (g), and $c = 40$ μm in (c), (d) and (e).

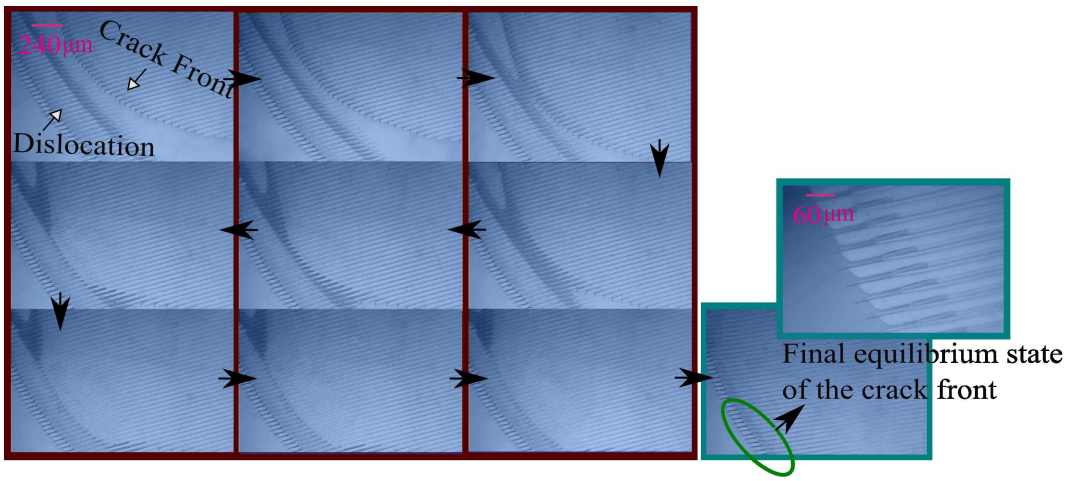

Figure A.7: Images from a video representing a typical crack-dislocation interaction sequence. The sample has $d = w = 10\ \mu$m, $c = 40\ \mu$m, and $\theta < 2^o$.

Thus, for the standard-core screw dislocation, the total strain energy per unit length within a cylinder of radius R_o is given by:

$$E_s = \frac{\mu c^2}{4\pi} \log \frac{R_o e^{3/2}}{b} \tag{A.8}$$

Substituting Eqn. (A8) into Eqn. (4) gives the same result as Eqn. (5), showing that the strain energy stored in the core can be neglected in this analysis.

A.1.2 Energy Release Rate due to Dilation

To evaluate the energy release rate due to dilation of the core region, a rough estimate is made by treating the dislocation as an elastic crack wedged open by a concentrated central force P in an infinite two-dimensional isotropic elastic solid, as shown in Fig. A8.

Tada [28] showed that crack opening profile, $v(x, 0)$, stress intensity factor,

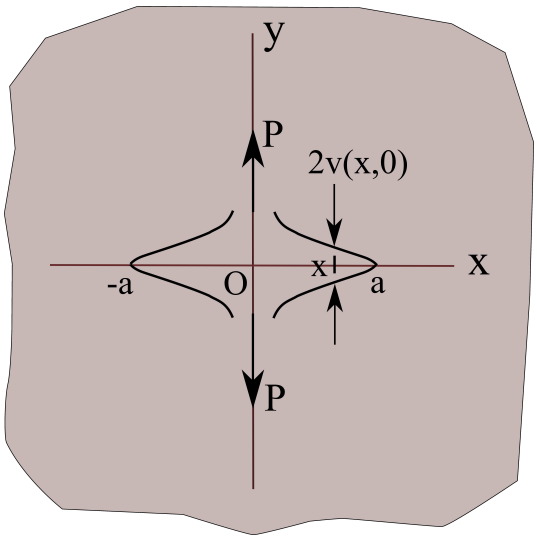

Figure A.8: An infinite two-dimensional elastic solid containing a finite crack on $y = 0$ and $|x| < a$.

K_I, and energy release rate, G, are given by:

$$2v(x,0) = \frac{4P}{\pi E'} \cosh^{-1} \frac{a}{x}, \quad |x| < a \tag{A.9}$$

$$K_I = P/\sqrt{\pi a} \tag{A.10}$$

$$G = K_I^2/E' \tag{A.11}$$

respectively, where $E' = E$ for plane stress conditions, and $E' = E/(1 - \nu^2)$ for plane strain conditions. From Eqns. (A9)-(A11), it is clear that energy release rate due to dilation is decreasing with increasing values of a. For the case that interchannel spacing $c = 20\,\mu$m, $a \approx 110\,\mu$m, and using typical values of $E' = 4$ MPa and $v = 10\,\mu$m, we obtain $G \approx 0.67$ N/m. Considering the typical work of separation for flat PDMS samples, about 0.25 N/m, and the fact that adhesion between structured samples can be enhanced by up to 30 times compared to a flat control, the energy release rate due to dilation is negligibly small.

BIBLIOGRAPHY

[1] C. Chothia, J. Janin, Nature 1975, 256, 705.

[2] N. Bowden, S. Brittain, A. G. Evans, J. W. Hutchinson, G. M. Whitesides, Nature 1998, 393, 146.

[3] R. J. Jackman, S. T. Brittain, A. Adams, M. G. Prentiss, G. M. Whitesides, Science 1998, 280, 2089.

[4] W. Yang, R. L. Somerville, Methods 1999, 19, 322.

[5] P. W. K. Rothemund, Proc. Natl. Acad. Sci. U.S.A. 2000, 97, 984.

[6] E. Kangas, B. Tidor, J. Phys. Chem. B 2001, 105, 880.

[7] J. K. N. Mbindyo, B. D. Reiss, B. R. Martin, C. D. Keating, M. J. Natan, T. E. Mallouk, Adv. Mater. 2001, 4, 249.

[8] G. M. Whitesides, B. Grzybowski, Science 2002, 295, 2418.

[9] G. M. Whitesides, M. Boncheva, Proc. Natl. Acad. Sci. U.S.A. 2002, 99, 4769.

[10] V. N. Manoharan, M. T. Elsesser, D. J. Pine, Science 2003, 301, 483.

[11] M. Lamblet, E. Verneuil, T. Vilmin, A. Buguin, P. Silberzan, L. Leger, Langmuir 2007, 23, 6966.

[12] H. Shahsavan, B. Zhao, Langmuir 2011, 27, 7732.

[13] A. K. Singh, Y. Bai, N. Nadermann, A. Jagota, C.-Y. Hui, Langmuir 2012, 28, 4213.

[14] A. Jagota, C.-Y. Hui, Materials Science and Engineering R 2011, 72, 253.

[15] Y. Bai, C. Jin, A. Jagota, C.-Y. Hui, J. Appl. Phys. 2011, 110, 054902.

[16] C. Jin, Y. Bai, A. Jagota, C.-Y. Hui, J. Appl. Phys. 2011, 110, 054903.

[17] S. Vajpayee, K. Khare, S. Yang, C.-Y. Hui, A. Jagota, Adv. Funct. Mater. 2011, 21, 547.

[18] O. Kafri, Opt. Lett. 1980, 5, 555.

[19] I. Amidror, The Theory of the Moir Phenomenon, Dordrecht, Netherlands, 1999.

[20] G. Oster, Y. Nishijima, Sci. Amer. 1963, 208, 54.

[21] J. M. Sanchez, S. El-Mansy, B. Sun, T. Scherban, N. Fang, D. Pantuso, et al. Acta Mater. 1999, 47, 4405.

[22] C. Jin, Int. J. Solid. Struct. 2008, 45, 6485.

[23] J. W. Hutchinson, Z. Suo, Advances in Applied Mechanics 1992, 29, 63.

[24] J. P. Hirth, J. Lothe, Theory of Dislocations, McGraw-Hill, New York, 1983.

[25] W. L. Noderer, L. Shen, S. Vajpayee, N. J. Glassmaker, A. Jagota, C.-Y. Hui, Proceedings of the Royal Society A, 2007, 463, 2631.

[26] W. Cai, A. Arsenlis, C. R. Weinberger, V. V. Bulatov, J. Mech. Phys. Solids 2006, 54, 561.

[27] J. Lothe, In: V. L. Indenbohm, J. Lothe, (Eds.) Elastic Strain Fields and Dislocation Mobility, North-Holland, Amsterdam, 1992.

[28] H. Tada, P. C. Paris, G. R. Irwin, The Stress Analysis of Cracks Handbook, 2nd. ed., Paris Productions, 1985.

[29] Zielenbewicz P and Rabczenko A 1988 Methods of molecular modelling of protein-protein interactions Biophysical Chemistry 29 219

[30] Potter M D 2004 Electrostatic filter and a method thereof US Patent 6773488 USPTO

[31] Brown R G, Derick B N, Stanley J O, Watkins Jr. J M 1970 Electrostatic filter unit with high stable charge and its manufacture US Patent 3487610 USPTO

[32] Jones T B 2003 Basic theory of dielectrophoresis and electrorotation IEEE Engineering in Medicine and Biology Magazine 22 33

[33] Debye P and Huckel E 1923 The theory of electrolytes. I. Lowering of freezing point and related phenomena Physikalische Zeitschrift 24 185

[34] Russel W B, Saville D A and Schowalter W R 1989 Colloidal Dispersions Cambridge University Press.

[35] Sharp K and Honig B 1990 Calculating total electrostatic energies with the non-linear Poisson–Boltzmann equation J. Phys. Chem. 94 7684

[36] Khripin C, Jagota A and Hui C-Y 2005 Electric fields in an electrolyte solution near a strip of fixed potential J. Chem. Phys. 123 134705

[37] Johnson K L, Kendall K and Robert A D 1971 Surface energy and the contact of elastic solids Proc. R. Soc. Lond. A 324 301

[38] Derjaguin B V, Muller V M and Toporov Y P 1975 Effect of contact deformations on the adhesion of particles J. Colloid Interface Sci. 53 314

[39] Muller V M, Derjaguin B V and Toporov Y P 1983 On two methods of calculation of the force of sticking of an elastic sphere to a rigid plane Colloids Surf. 7 251

[40] Tabor D 1977 Surface forces and surface interactions J. Colloid Interface Sci. 58 2

[41] Maugis D 1992 Adhesion of spheres: the JKR-DMT transition using a Dugdale model J. Colloid Interface Sci. 150 243

[42] Muller V M, Yushchenko V S and Derjaguin B V 1980 On the influence of molecular forces on the deformation of an elastic sphere and its sticking to a rigid plane J. Colloid Interface Sci. 77 91

[43] Attard P and Parker J L 1992 Deformation and adhesion of elastic bodies in contact Phys. Rev. A 46 7959

[44] Greenwood J A 1997 Adhesion of elastic spheres Proc. R. Soc. Lond. A 453 1277

[45] Feng J Q 2000 Contact behavior of spherical elastic particles: a computational study of particle adhesion and deformations Colloids Surf. A 172 175

[46] Feng J Q 2001 Adhesive contact of elastically deformable spheres: a computational study of pull-off force and contact radius J. Colloids Interface Sci. 238 318

[47] Keller H B 1977 Numerical solution of bifurcation and non-linear eigenvalue problems Applications of Bifurcation Theory ed P Rabinowitz (New York: Academic) pp 359

[48] Keller H B 1983 The bordering algorithm and path following near singular points of high nullity SIAM J. Sci. Stat. Comput. 4 573

[49] Yang F 2005 Adhesive contact between an elliptical rigid flat-ended punch and an elastic half space J. Phys. D: Appl. Phys. 38 1211

[50] Johnson K L and Greenwood J A 2005 An approximate JKR theory for elliptical contacts J. Phys. D: Appl. Phys. 38 1042

[51] Wu J J 2006 The numerical analyses on elliptical adhesive contact J. Phys. D: Appl. Phys. 39 1899

[52] Sumer B, Onal C D, Aksak B and Sitti M 2010 An experimental analysis of elliptical adhesive contact J. Appl. Phys. 107 113512

[53] Johnson K L 1985 Contact Mechanics (Cambridge: Cambridge University Press)

[54] Derjaguin B V 1934 Untersuchungen uber die reibung und adhasion: IV. Theorie des anhaftens kleiner teilchen Kolloid Z. 69 155

[55] Johnson K L and Greenwood J A 1997 An adhesion map for the contact of elastic spheres J. Colloid Interface Sci. 192 326

[56] Love A E H 1929 The stress produced in a semi-infinite solid by pressure on part of the boundary Phil. Trans. R. Soc. Lond. A 228 377

[57] Jin C, Khare K, Vajpayee S, Yang S, Jagota A and Hui C-Y 2011 Adhesive contact between a rippled elastic surface and a rigid spherical indenter: from partial to full contact Soft Matter 7 10728

[58] Guduru P R and Bull C 2007 Detachment of a rigid solid from an elastic wavy surface: experiments J. Mech. Phys. Solids 55 473

[59] Jahnke E and Emde F 1945 Tables of functions (New York: Dover)

[60] Zilberman S and Persson B N J 2002 Adhesion between elastic bodies with rough surfaces Solid State Commun. 123 173

[61] Sutton, A.P. and R.W. Balluffi, Interfaces in Crystalline Materials. Monographs on the physics and chemistry of materials; 511995, Oxford: Oxford University Press. xxxii.

[62] F. C. Frank and J. H. van der Merwe , Proc. R. Soc. London, Ser. A, 198 (1949) 205.

[63] F. C. Frank and J. H. van der Merwe, Proc. R. Soc. London, Ser. A, 198 (1949) 216.

[64] F. C. Frank and J. H. van der Merwe, Proc. R. Soc. London, Ser. A, 200 (1949) 125.

[65] J. H. van der Merwe, Proc. Phys. Soc., London, A, 63 (1950) 616.

[66] J. H. van der Merwe, J. Appl. Phys., 34 (1963) 117.

[67] J. H. van der Merwe, J. Appl. Phys., 34 (1963) 123.

[68] J. H. van der Merwe, J. Appl. Phys., 41 (1970) 4725.

[69] J. H. van der Merwe, Treatise Mater. Sei. Technol., 2 (1973) 1.

[70] Christian J.W. The theory of transformations in metals and alloys. 3rd ed. Oxford: Pergamon Press; 2002.

[71] Matthews, J.W. and A.E. Blakeslee, Deffects in epitaxial multilayers .1. misfit dislcotions. Journal of Crystal Growth, 1974. 27(DEC): p. 118.

[72] Matthews, J.W. and A.E. Blakeslee, Defects in epitaxial multilayers. II. Dislocation pile-ups, threading dislocations, slip lines, and cracks. Journal of Crystal Growth, 1975. 29(3): p. 273.

[73] Matthews, J.W. and A.E. Blakeslee, Defects in epitaxial multilayers. III. Preparation of almost perfect multilayers. Journal of Crystal Growth, 1976. 32(2): p. 265.

[74] Kamat, S.V. and J.P. Hirth, Dislocation injection in strained multilayer structures. Journal of Applied Physics, 1990. 67(11): p. 6844.

[75] Hirth, J.P. and X.X. Feng, Critical layer thickness for misfit dislocation stability in multilayer structures. Journal of Applied Physics, 1990. 67(7): p. 3343.

[76] Laird, C. and H.I. Aaronson, The dislocation structures of the broad faces of widmanstatten γ plates in an Al-15% Ag alloy. Acta Metallurgica, 1967. 15(1): p. 73.

[77] J. W. Matthews, The observation of dislocations to accommodate the misfit between crystals with different lattice parameters. Phil. Mag. 6 (1961) 1347.

[78] Chen, C., K.N. Tu, C.H. Tung, T.T. Sheng, A. Ploessl, R. Scholz, and U. Gosele, Twist-type silicon bicrystals and compliant substrates prepared from silicon-on-insulator wafers. Philosophical Magazine A: Physics of Condensed Matter, Structure, Defects and Mechanical Properties, 2000. 80(Compendex): p. 881.

[79] Amelinckx, S., The direct observation of dislocations. Solid state physics. Supplement 61964, New York: Academic Press.

[80] Whitton, J. L., J. Nuclear Materials, 1964, 12, 115.

[81] Shiflet, G. J., 1986, Mater. Sci. Eng. 81, 61.

[82] Read, W.T. and W. Shockley, Dislocation models of crystal grain boundaries. Phys. Rev. 1950. 78(3): p.275.

[83] Brooks, H., Theory of internal boundaries, in Metal Interfaces, Am. Soc. Metals, Cleveland Press (1952).

[84] Frank F.C. Conference on plastic deformation of crystalline solids. Carnegie Institute of Technology and Office of Naval Research; 1950. p. 150.

[85] Bilby B.A. Prog Solid Mech 1960;1:329.

[86] Knowles, K.M., The dislocation geometry of interphase boundaries. Philosophical Magazine A-Physics of Condensed Matter Structure Defects and Mechanical Properties, 1982. 46(6): p.951.

[87] Bollmann, W., Crystal defects and crystalline interfaces. 1970, Berlin: Springer-Verlag. xi.

[88] Bollmann, W., O-lattice calculation of an fcc-bcc interface. Physica Status Solidi A-Applied Research, 1974. 21(2): p.543.